UNIVERSIDADE DE SÃO PAULO
ESCOLA POLITÉCNICA DA USP
DEPARTAMENTO DE ENGENHARIA NAVAL E OCEÂNICA

Daniel Francisconi Oliveira

Aerodynamic modelling and simulation of offshore wind turbines using actuator models

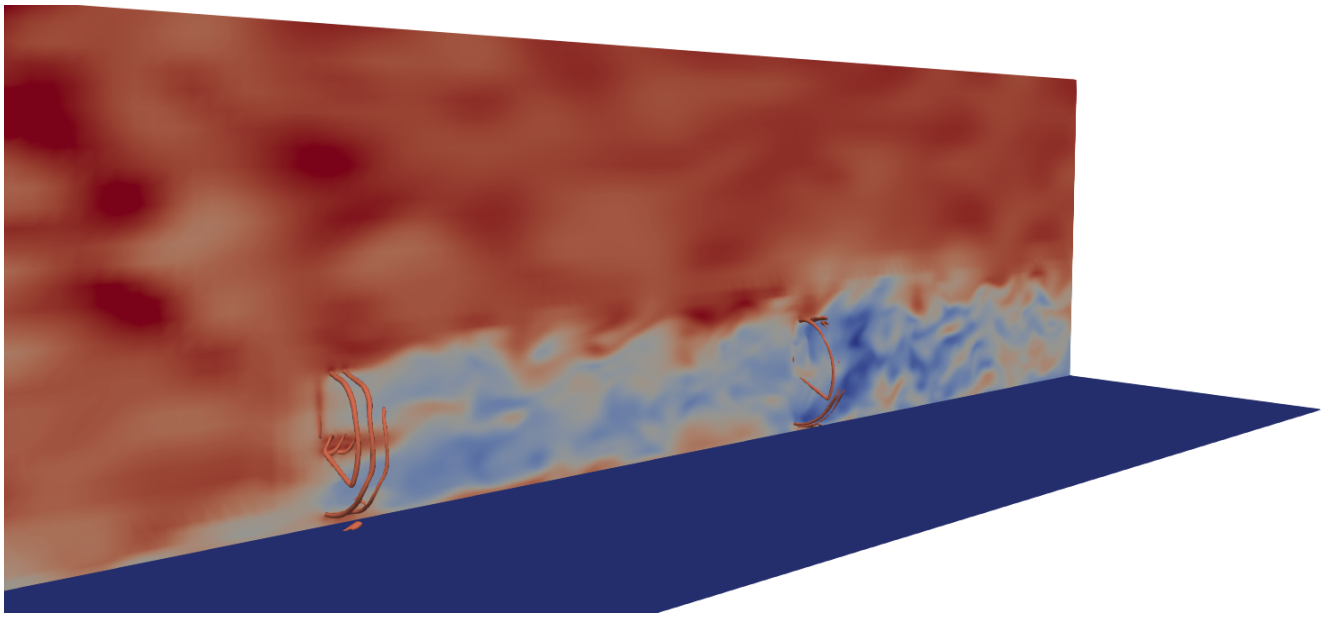

SÃO PAULO
2023

DANIEL FRANCISCONI OLIVEIRA

Aerodynamic modelling and simulation of offshore wind turbines using actuator models

Versão Corrigida

Dissertação apresentada à Escola Politécnica da Universidade de São Paulo para obtenção do título de Mestre em Ciências.

Área de concentração: Engenharia Naval e Oceânica

Orientador: Prof. Dr. Bruno Souza Carmo

SÃO PAULO
2023

Catalogação-na-publicação

Oliveira, Daniel Francisconi
Aerodynamic modelling and simulation of offshore wind turbines using actuator models / D. F. Oliveira -- São Paulo, 2022.
98 p.

Dissertação (Mestrado) - Escola Politécnica da Universidade de São Paulo. Departamento de Engenharia Naval e Oceânica.

1.Dinâmica dos fluidos computacional 2.Turbina eólica 3.Linha atuadora 4.Disco atuador 5.Configuração em tandem I.Universidade de São Paulo. Escola Politécnica. Departamento de Engenharia Naval e Oceânica II.t.

ACKNOWLEDGEMENTS

Every person that came before me and crossed my path during my life made this work possible somehow. I would like to specially thank my parents, my brother and my girlfriend, who is a fantastic woman and researcher, for all the support, without them none of this would be possible.

I would like to express the deepest gratitude to my supervisor Professor Bruno Souza Carmo for his guidance and dedication of hours and hours of virtual meetings during this pandemic time. Also, to Professor Alexandre Simos who introduced us at the end of my under-graduation, and to the colleagues of NDF: Rodolfo Puraca, Lucas Franceschini and Marielle de Oliveira for the several enriching discussions.

Finally, I would like to thank the University of São Paulo and its partners around the world for providing me the technical means to develop this work, and to Petrobras, who financially supported me during the project.

"Not one man, nor a group of men, but in all men: in you. You the people have the power, the power to create machines, the power to create happiness. You the people have the power to make this life free and beautiful, to make this life a wonderful adventure."

Charlie Chaplin - The Great Dictator (1940)

ABSTRACT

There is a growing demand for renewable energy sources in the context of climate change mitigation goals. Wind energy is playing a fundamental role in the energy transition, with a steep increase of new onshore and offshore installations during the past years. The ability to design larger wind turbines and optimized wind farms depends on the capacity to model and simulate the wind energy extraction process. Actuator models have been extensively used to simulate wind turbine rotors. The present work investigates the capabilities of the actuator disc model (ADM) and actuator line model (ALM) using computational fluid dynamics (CFD) simulations. The objective is to understand the influence of numerical parameters, validate the models, and analyze their results for offshore wind turbines. The work found that ADM can provide accurate power and thrust predictions and overall flow dynamics, but its axisymmetric behaviour cannot deal with the real flow close to the rotor. Instead, ALM can capture the turbulent structures in the near-wake region with higher fidelity, but the time-step needed is considerably smaller due to the $\mathrm{CFL_{tip}}$ restriction, which limits the tip blade to travel less than one grid cell within a time step, increasing the computational cost, but still less than blade-resolved models. With large eddy simulations (LES), we found a very good agreement between ALM and the well consolidated Blade Element Momentum (BEM) theory for a smoothing parameter ϵ fixed at 2.5 times the grid spacing. Coarser grid mesh overestimates the forces notably near the blade tip, thus, a tip correction would improve power and thrust predictions in this case. It was shown that mesh refinement far from the rotor has no impact on the power and thrust prediction of a single turbine. Regarding turbines in tandem configuration, the importance of the inflow turbulence and turbine spacing was evaluated for ADM with Reynolds-averaged Navier–Stokes (RANS) simulations and for ALM using a synthetic turbulence generator for LES. Higher turbulence intensities lead to faster wake recovery and increased power prediction of the downstream turbine, without considering structural consequences. Larger turbine spacing also improves energy at downstream turbines, however, it is limited by the size of the site. The levels of turbulence showed an important impact on the wake recovery of the first wind turbine, but not very significant for the second one, which shows that inlet turbulent quantities would have little impact on a third row of turbines in a 5D configuration. For a 15 MW wind turbine, increasing the turbine spacing from 5D to 10D lead to an improvement of 40% of power prediction at the downstream turbine. Finally, several wake analyses were made to characterize its dynamics, and ALM was able to predict asymmetric velocities due to the atmospheric boundary layer (ABL) and rotational direction.

Keywords: Computational fluid dynamics. Wind turbines. Actuator line. Actuator disc. Tandem configuration.

RESUMO

Há uma demanda crescente por fontes de energia renováveis no contexto do combate às mudanças climáticas, e a energia eólica desempenha papel fundamental na transição energética. Projetar grandes turbinas e otimizar parques eólicos depende da capacidade de modelar e simular a extração de energia do vento. Modelos atuadores têm sido amplamente usados para simular aerogeradores. Este trabalho investiga as capacidades do modelo de disco atuador (ADM) e do modelo de linha atuadora (ALM), usando simulações de dinâmica de fluidos computacional (CFD). O objetivo é entender a influência de parâmetros numéricos, validar os modelos e analisar seus resultados para turbinas offshore. O ADM pode fornecer previsões precisas de potência e empuxo, além da dinâmica geral do escoamento, porém seu comportamento axissimétrico não é capaz de reproduzir o escoamento próximo ao rotor. Por outro lado, o ALM pode capturar as estruturas turbulentas na região da esteira próxima com maior fidelidade, apesar de o passo de tempo ser consideravelmente menor devido à restrição $\mathrm{CFL}_{\mathrm{tip}}$, que limita a ponta da pá a percorrer até uma célula da malha em um passo de tempo, amentando o custo computacional, ainda abaixo de modelos *blade-resolved*. Com simulações LES (*large eddy simulations*), foi encontrada uma concordância muito boa entre o ALM e a teoria já bem estabelecida de Blade Element Momentum (BEM) para um fator de espalhamento ϵ fixado em 2.5 vezes o espaçamento da malha. Uma malha mais grosseira superestima as forças especialmente perto da ponta da pá, portanto, uma correção de ponta da pá melhoraria as previsões de potência e empuxo neste caso. Foi mostrado que o refino da malha ao longe do rotor não tem impacto na previsão de potência e empuxo de uma única turbina. Em relação às turbinas em configuração tandem, a importância da turbulência na condição de entrada e espaçamento entre turbinas foi avaliada para ADM com simulações RANS (*Reynolds-averaged Navier–Stokes*) e para ALM com gerador de turbulência sintético para LES. Intensidades de turbulência mais altas levaram a recuperação de esteira mais rápida e aumentaram a previsão de potência da turbina a jusante, sem considerar consequências estruturais. O espaçamento maior entre as turbinas também melhora a energia da turbina a jusante, no entanto, fica limitado à área do site. Os níveis de turbulência mostraram impacto importante na recuperação da esteira do primeiro aerogerador, mas pouco significativo para o segundo, mostrando que variáveis turbulentas na entrada teriam pouco impacto em uma terceira fileira de aerogeradores em configuração 5D. Para uma turbina eólica de 15 MW, aumentar o espaçamento entre turbinas de 5D para 10D elevou a potência da turbina a jusante em 40%. Por fim, análises da esteira foram feitas, e o ALM foi capaz de prever velocidades assimétricas devido à presença de camada limite atmosférica (ABL) e o sentido de rotação das pás.

Palavras-chave: Dinâmica dos fluidos computacional. Turbina eólica. Linha atuadora. Disco atuador. Configuração em tandem.

LIST OF FIGURES

LIST OF TABLES

LIST OF ABBREVIATIONS AND ACRONYMS

ACE	Actuator Curve Embedding
ADM	Actuator Disc Model
ALM	Actuator Line Model
AoA	Angle of Attack
ABL	Atmospheric Boundary Layer
BEM	Blade Element Momentum
CAPEX	Capital Expenditure
CCS	Carbon Dioxide Capture and Storage
CPU	Central Processing Unit
CAGR	Compound Annual Growth Rate
CFD	Computational Fluid Dynamics
CBL	Convective Boundary Layer
CFL	Courant–Friedrichs–Lewy condition
COP26	26^{th} United Nations Climate Change Conference
DNS	Direct numerical simulation
FOWT	Floating Offshore Wind Turbine
GCM	Global Climate Model
GWEC	Global Wind Energy Council
GHG	Greenhouse Gas
HAWT	Horizontal Axis Wind Turbine
IBL	Internal Boundary Layer
IEA	International Energy Agency
IPCC	Intergovernmental Panel on Climate Change
LES	Large eddy simulation
MCBL	Moderately Convective Boundary Layer
NREL	National Renewable Energy Laboratory
NDC	Nationally Determined Contributions
NBL	Neutral Boundary Layer
NWP	Numerical Weather Prediction
OpenFOAM	Open-source Field Operation And Manipulation

PV	Photovoltaics
RANS	Reynolds-averaged Navier–Stokes
SST	Shear Stress Transport
SBL	Stable Boundary Layer
TSR	Tip Speed Ratio
TKE	Turbulent Kinetic Energy
VIM	Vortex Induced Motion
WMO	World Meteorological Organization

LIST OF SYMBOLS

$^{\circ}$C	Degrees Celsius
$^{\circ}$	Degrees
ϵ	Smooth Force Projection Factor
Δ_g	Grid Size
C_P	Power Coefficient
C_T	Thrust Coefficient
C_D	Drag Coefficient
C_L	Lift Coefficient
C_x	Axial Force Coefficient
C_y	Tangential Force Coefficient
D	Rotor Diameter or Drag
L	Lift
R	Rotor Radius
r	Local Radius
T	Thrust
P	Power
B	Number of Blades
Q	Torque
F	Tip Correction Factor
g	Tip Correction Constant
c	Airfoil Chord
k	Turbulent Kinetic Energy
ε	Dissipation of TKE
ω	Specific Rate of Dissipation of TKE
U_∞	Far Inflow Velocity
U_D	Wind Speed at the Rotor
U_W	Wake Velocity
W	Relative Flow Velocity
p	Fluid Pressure
p_∞	Far Pressure

a	Axial Induction Factor
a'	Tangential Induction Factor
ρ	Density
A_D	Disc Area
Ω	Angular Velocity
λ	Tip Speed Ratio
α	Angle of Attack
β	Twist Angle
ϕ	Relative Flow Angle
σ_r	Chord Solidity
ν	Kinematic Viscosity
$\vec{f}$	Source Term
$\vec{u}$	Fluid Velocity
η_ϵ	Gaussian Smooth Function
f_ϵ	Smoothed Force Projection

CONTENTS

1 INTRODUCTION

1.1 WIND ENERGY CONTEXT

In the beginning of the 2020s several events to discuss a sustainable future took place, notably the Leaders Summit on Climate in 2021 and the 27$^{\text{th}}$ United Nations Climate Change Conference, also known as COP27, in 2022. Both summits aim to accelerate action towards the goals of the Paris Agreement, signed in 2016 by 191 countries, to limit global warming to well below 2 °C, and preferably 1.5 °C, compared to pre-industrial levels.

The problems caused by a slight increase in global temperature can be devastating. Depending on the region, some consequences may be: more droughts and heat waves, changes in precipitation patterns, lengthen of the frost-free season, stronger and more intense hurricanes, melting of glaciers, rise of sea level and ocean acidity etc. All these effects imply a significant impact on biodiversity and ecosystems, with consequences on human systems and well-being, specially on the poor and vulnerable.

According to the Intergovernmental Panel on Climate Change (IPCC), the climate-related risks to health, livelihoods, food security, water supply, human security, and economic growth are projected to increase with global warming of 1.5 °C and increase further with 2 °C. Limiting warming to 1.5 °C implies reaching net zero CO_2 emissions globally around 2050 and concurrent deep reductions in emissions of non-CO_2 greenhouse effect gases, particularly methane (IPCC, 2018).

In 2020, human-induced warming reached approximately 1.2 °C, increasing at 0.2 °C per decade. Figure 1 presents the historical mean global temperatures difference compared to 1850–1900 baseline. According to WMO (2021), there is a 40% chance that, until 2025, one year will be at least 1.5 °C warmer, and the chance is increasing with time.

The most recent Global Wind Report elaborated by the Global Wind Energy Council (GWEC, 2021) underlines that the current policies are propelling us towards the 2.9 °C global warming. Figure 2 shows the different ranges of global warming temperatures according to greenhouse gas (GHG) emissions. Without any policy aiming at a reduction of emissions, humanity would cause an increase of global temperature above 4 °C. On the other hand, if all pledges and nationally determined contributions (NDCs) of December 2020 are implemented, the world might reach 2.1 °C and miss the net zero by 2050 target.

Society is more aware of the dangers of climate change and the urgency of reducing human impact on the Earth. For example, the European Union is embedding in law a target of reducing net greenhouse gas emissions by at least 55% by 2030 and a net zero target by 2050. At the Leaders' Climate Summit, the US announced a reduction of 50-52% by 2030 compared to 2005 in the country. In the same occasion, Brazil committed to achieving net zero by 2050, end illegal deforestation by 2030, and double funding for forest preservation. In this context, basically all the great economies in the world are committing to similar goals for reducing emissions.

Figure 1 – Global annual mean temperature difference from pre-industrial conditions (1850-1900) for five global temperature data sets.

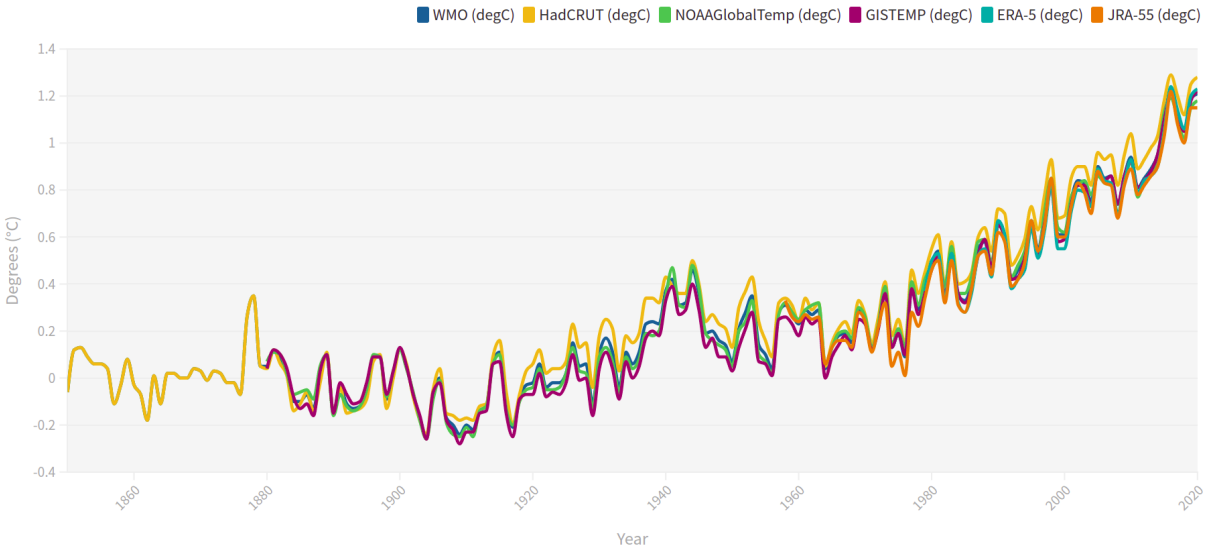

Source: (WMO, 2021)

Figure 2 – Emissions and expected warming projections based on pledges and current policies.

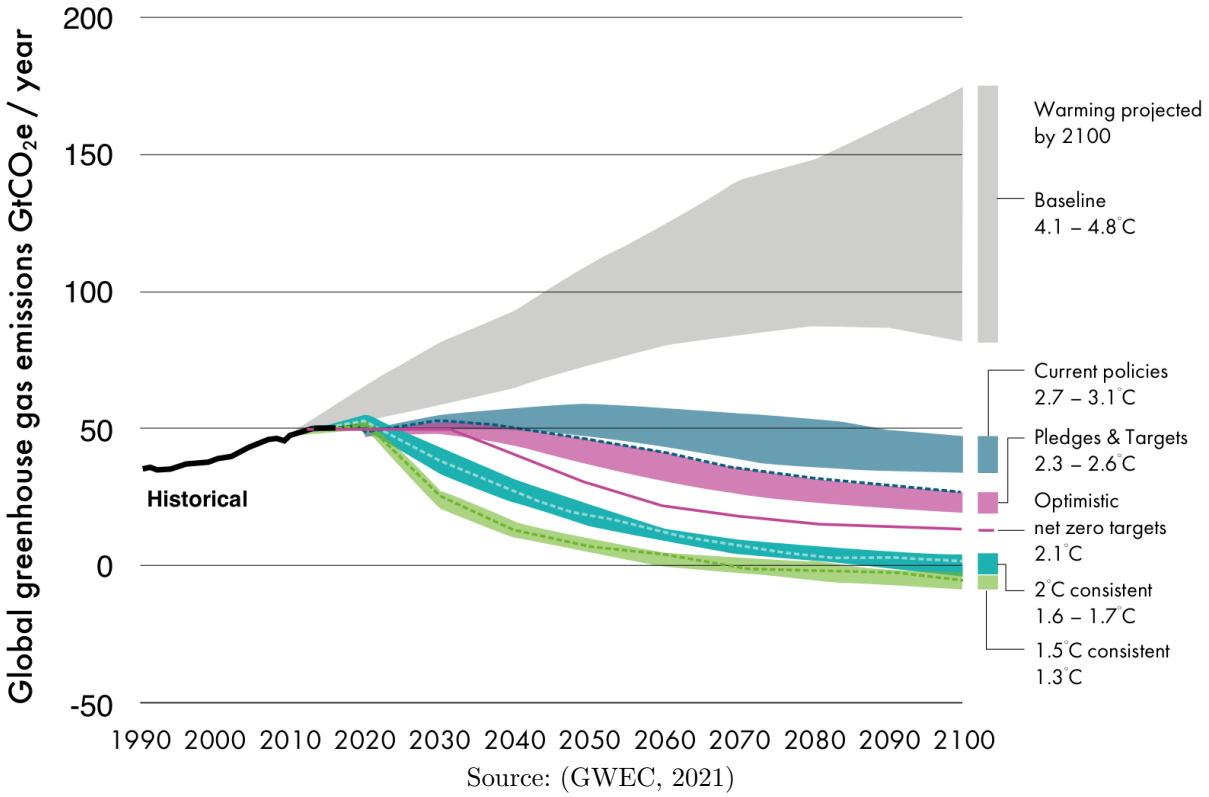

Source: (GWEC, 2021)

Figure 3 – Historical CO_2 emissions and projected emissions from operating energy infrastructure as it was used historically, 1900-2100.

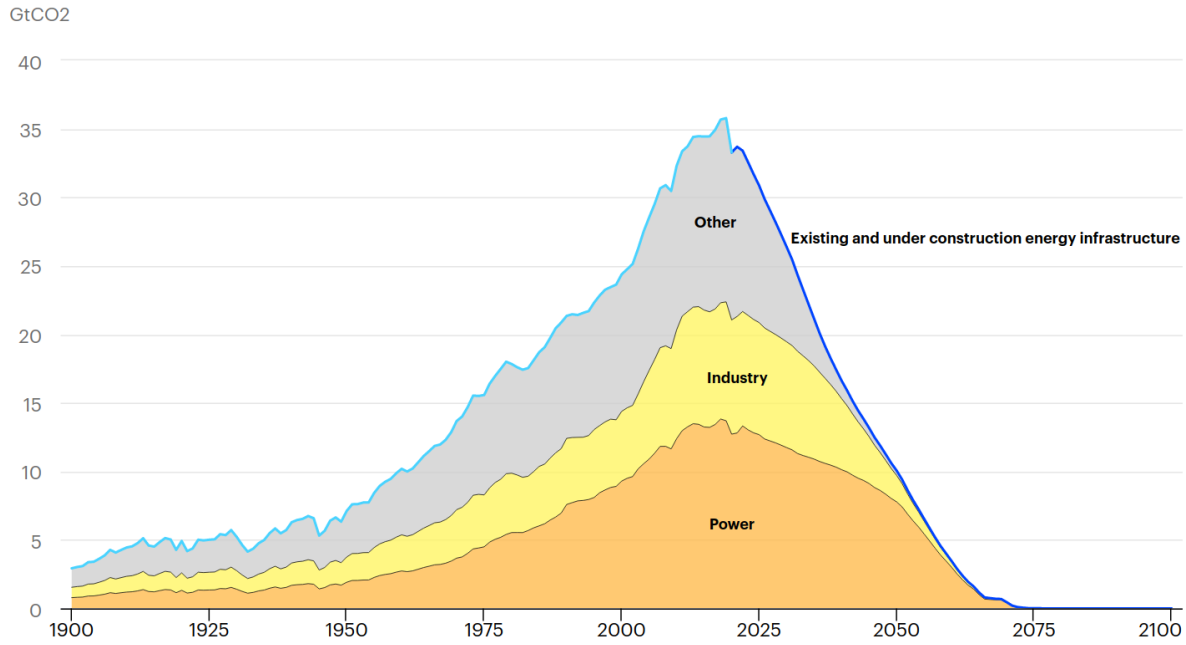

Source: (IEA, 2020)

It is important to notice that avoiding new emissions is not enough. If nothing is done about emissions from the existing infrastructure, climate goals will not be accomplished. Considering today's and under construction industrial and power plants, buildings, and vehicles that rely on fossil fuels, operating for their usual lifetimes, in 2050 there would still be around 10 Gt of CO_2 emission. This scenario is shown in Fig. 3, where the historical CO_2 emissions from 1900 and projections to 2100 are separated by categories of power, industry, and other. The graphic illustrates very well the turning point that we should be at the present moment: the maximum carbon emission of all times, with a break of the exponential growth of the last century and a sharp decrease in emissions.

Since the energy sector is responsible for around three-quarters of global GHG emissions (IPCC, 2019), the only chance of meeting the Paris Agreement target is an increasingly steep expansion of renewables and related infrastructure in replacement of fossil fuel-based capacities. Figure 4 shows the global energy consumption in 2019. On the left side, 67% of the total final energy consumption was based on oil, coal, and natural gas. And on the right side of the figure, it is shown that 63% of the electric power generation also used fossil fuels sources. It is clear, therefore, that non-renewable sources are still the main basis of global energy production.

However, the changes in the global electricity supply during the last two years were very positive for sustainable energies. Figure 5 shows that the world increased renewable sources and decreased the fossil ones. It is interesting to notice that wind energy was responsible for the largest absolute growth in electricity generation in 2020. According to

Figure 4 – Global final energy consumption in 2019.

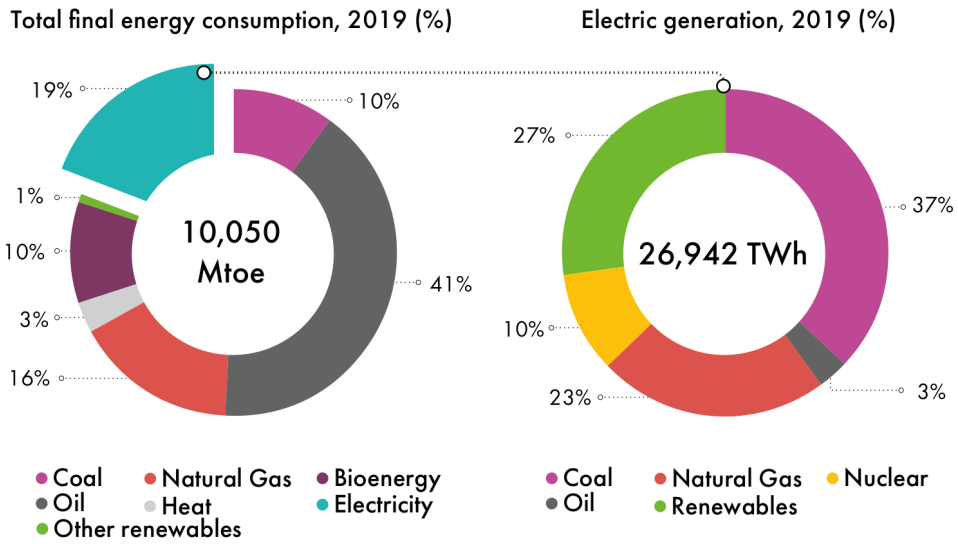

Source: (GWEC, 2021)

Figure 5 – Global electricity supply change in 2020.

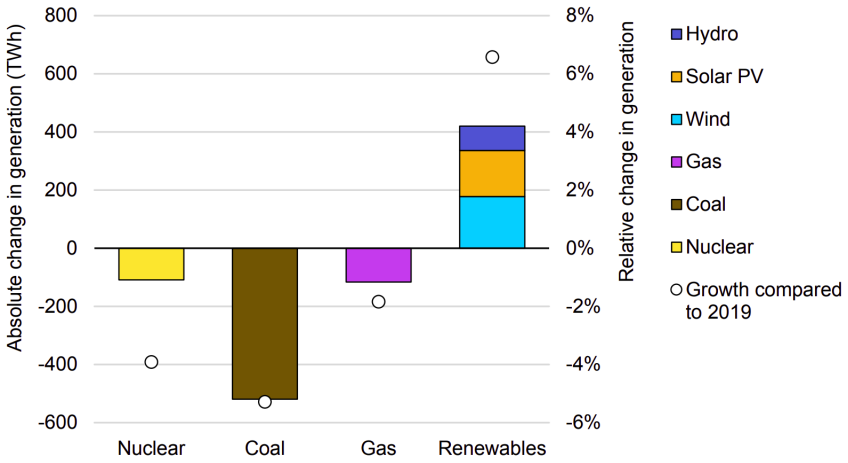

Source: (IEA, 2020)

IEA (2020), in the same year, Central and South America were the continent region with the largest share of renewable sources, followed by Europe. On the contrary, the Middle East had the smallest share of renewables, followed by Eurasia.

The political, economic, social, and technical feasibility of solar energy, wind energy, and electricity storage technologies has improved dramatically over the past few years, while that of nuclear energy and carbon dioxide capture and storage (CCS) in the electricity sector have not shown similar improvements. According to IPCC (2018), to limit global warming to 1.5 °C, renewable sources of energy (bioenergy, hydro, wind, and solar) should supply a share of 52–67% of primary energy in 2050, while the share from coal should decrease to 1–7%, with a large fraction of this coal use combined with CCS. Credit agencies are now expecting global oil demand to continue declining steadily over the next decade,

Figure 6 – Historical development of new wind turbine installations (GW) in the world 2001-2020.

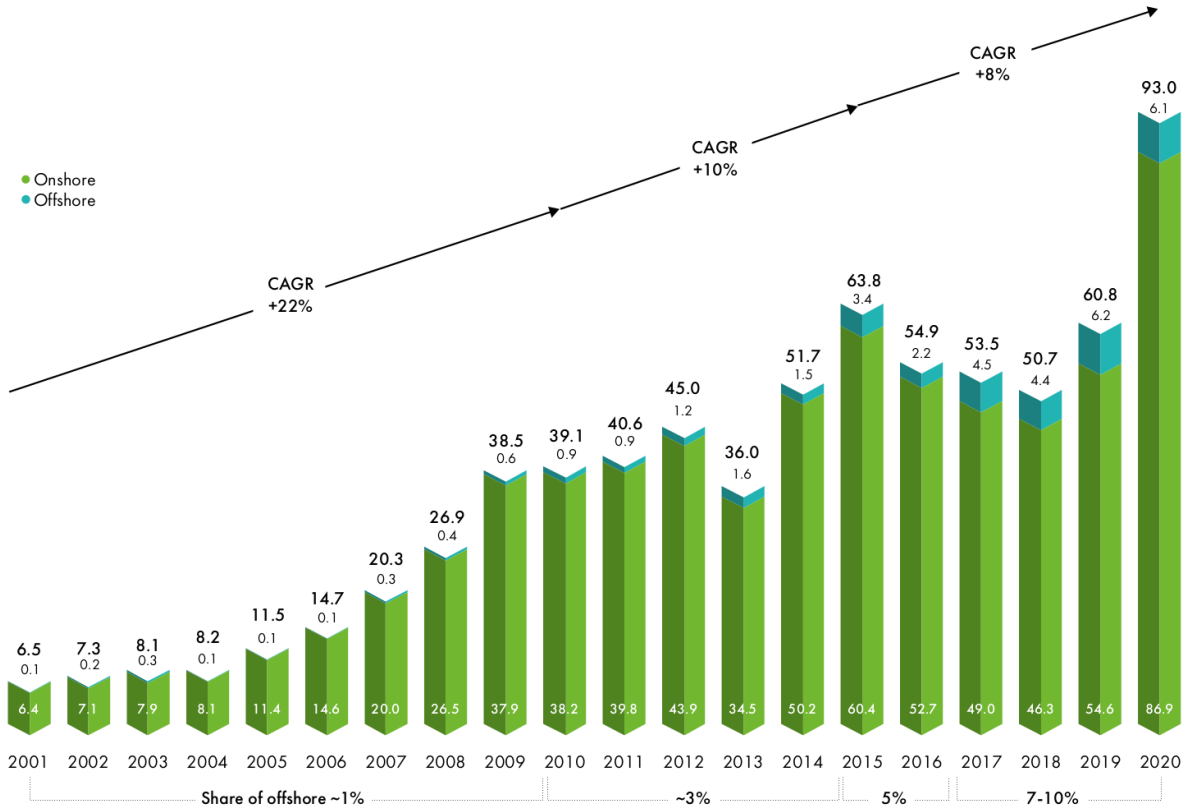

Source: (GWEC, 2021)

in its most conservative outlook, BP (2020) forecasts peak oil demand as soon as 2025.

In this context, wind energy plays a fundamental role in building a sustainable future, and with the advancement of technology and government subsidies, the world is accelerating the use of this clean energy. Figure 6 shows the global historical development of new wind turbine installations since 2001. Although the compound annual growth rate (CAGR) decreased compared to the beginning of the century, it maintained a significant positive rate, tracing a robust acceleration of the wind energy industry. The world entered the 21$^{\text{th}}$ century with 24 GW of wind energy installations and ended 2020 with a total of 743 GW, from which 35 GW concern offshore installations. According to IRENA's transforming energy scenario (IRENA, 2020), the annual deployment for wind energy must surge to around 180 GW, and the IEA's Net Zero by 2050 scenario (IEA, 2021) points to 160 GW by 2025 and 280 GW by 2030 to reach the sustainable goals.

Also in Fig. 6, it is clear that the new onshore installations (in green) are much more significant than the offshore ones (in blue). However, the share of offshore increased substantially during the last 20 years, starting with less than 1% and ending 2019 with a share of 10% of new installations. Regarding only the new offshore installations in the last 5 years, Fig. 7 highlights China as the main responsible for the development of offshore wind

Figure 7 – New offshore wind turbine installations (MW) by region for the past five years.

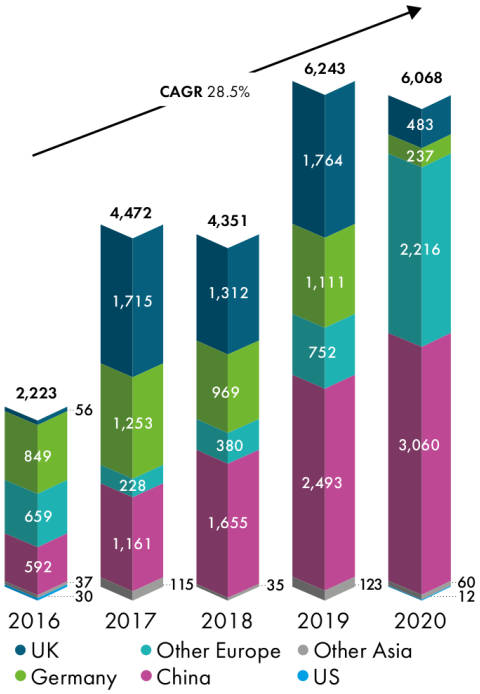

Source: (GWEC, 2021)

turbines, followed by the UK, Germany, and, specially in 2020, other European countries. According to GWEC (2021), this year, the capital expenditure (CAPEX) committed to offshore wind overtook investment in offshore oil and gas for the first time.

Offshore wind farms are a very promising concept because of the better wind resources. With no obstacles nor complex topography, the ocean location has usually higher wind velocities compared to land, which implies more wind energy available for power extraction. Also, politically and socially, the offshore wind farms may have a negligible visual and noise impact. Furthermore, since coastal regions have commonly dense populations, it may also alleviate the electrical transmission from the country. However, there is the additional complexity of hydrodynamic loads from waves and currents, as well as challenges for designing the foundation for shallow waters, and the floating system for deep sea waters. Moreover, the impact on marine ecosystems must still be analyzed in greater detail.

Another interesting trend observed is the growth in size of wind turbines during the past decades and its projections for the future. The costs of installation and maintenance can be optimized for a wind farm with a reduced number of wind turbines that generate the same amount of energy. Figure 8 presents some typical wind turbine sizes since 1980 and the prospects for the next decades. For comparison, the world's largest passenger airliner is also presented in scale, the Airbus A380, with a wingspan of 80 m and capacity for holding more than 500 people. Since the rotor efficiency increases with its diameter, and wind resource quality increases with height, the maximum size of wind turbines is

Figure 8 – Growth in size of wind turbines since 1980 and prospects. Airbus A380 for size comparison.

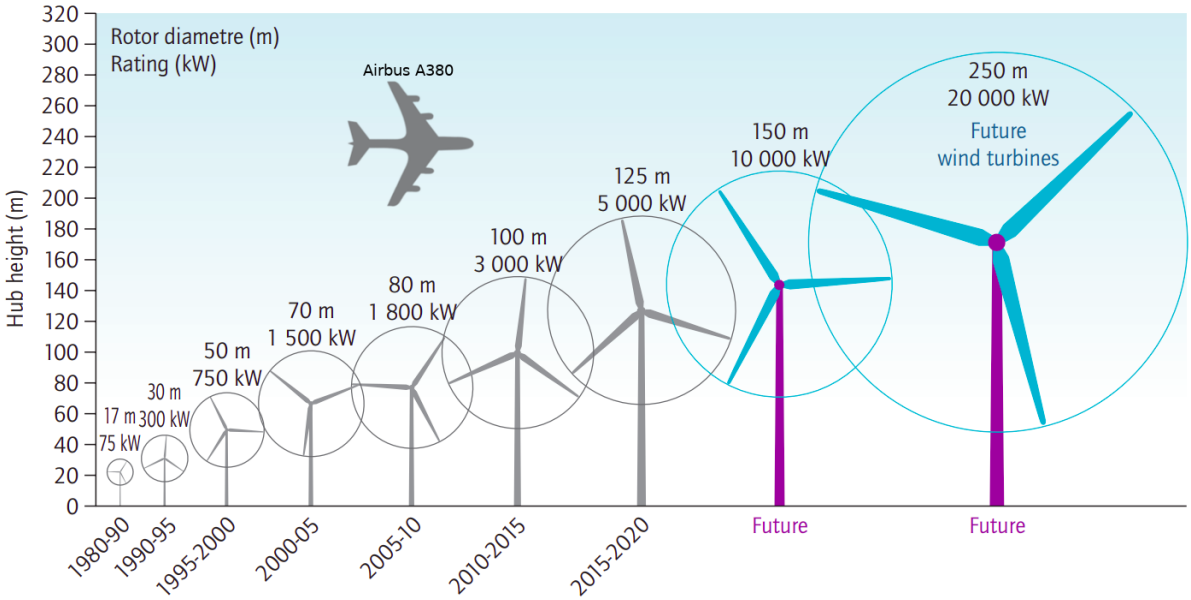

Source: adapted from (IEA, 2013)

related to technological limitations. Currently, the most powerful offshore wind turbines feature from 14 MW to 16 MW capacity, with rotors diameters from 220 m to 242 m.

The complexity of designing these gigantic rotating structures is huge, and gets even more challenging considering offshore applications, where ocean conditions such as waves, currents, and corrosion must also be taken into account. The difficulty increases when dealing with wind farms, where multiple turbines may interact with each other aerodynamically. While on onshore applications the terrain may define the positioning of wind turbines, on the ocean, the freedom of choosing its locations leads to the question: how far one turbine should be from the other one? Turbine distance becomes one of the main issue in designing an offshore wind farm, and understanding the wind turbine interaction is a necessary step for optimized projects.

1.2 WIND TURBINE FLOW

When the air passes through a wind turbine rotor it is strongly modified, notably by the blades. The near-wake is the affected region immediately downstream the rotor, but it is difficult to visualize the phenomenon in real applications because of the optical nature of air: transparency. However, in a rare arrangement of sunlight, rain, and clouds, the near-wake could be recorded in video, and a snap-shot is presented in Fig. 9a. What can be partially seen are the helicoidal vortex lines generated by each blade tip. As a low pressure zone, it concentrates the droplets that are illuminated by the sunlight in contrast with the dark clouds in the background. Figure 9b draws the schematic tip vortices coloured by the

Figure 9 – Wake of a V150-4.2MW turbine during rain and sunlight in Campo Formoso, Bahia, Brazil. Snap-shot from video provided by Lucas Tavares Ferreira (a), and schematic lines of tip-vortices coloured by the respective blade (b).

(a) (b)

respective blade. This phenomenon is more commonly seen in ship propeller experiments underwater due to cavitation, or sometimes in helicopter rotors under similar conditions.

Regarding the methodologies available for aerodynamic studies of wind turbines, besides wind tunnel experiments and field measurements, numerical simulations using computational fluid dynamics play a major role in research advancements. The scope of this work is to investigate numerical models available and understand their limits and capacities for modelling and simulating offshore wind turbines.

One of the great challenges of numerical simulations of wind farms is the multiple scales that concern the wind flow (Fig. 10). From global weather effects of thousands of kilometers to blade airfoil scales of meters, there is a large spectrum of models and tools designed to deal with a specific physical scale. However, coupling all the scales together, as it is in reality, is still unfeasible with the existing computational resources. Fortunately, it is possible to select scales of interested regarding the observed phenomena, thus not all the scales must be simultaneously treated. The present work is mainly concentrated between the scale of a single turbine and a wind farm, where wake interactions arise. Therefore, the airfoil scale is considered by 2-D modelling, but the meso and macroscale are completed neglected in this study.

Figure 10 – Schematic illustrating the wide range of flow scales relevant to wind energy: from the turbine blade scale to the meteorological mesoscale and macroscale.

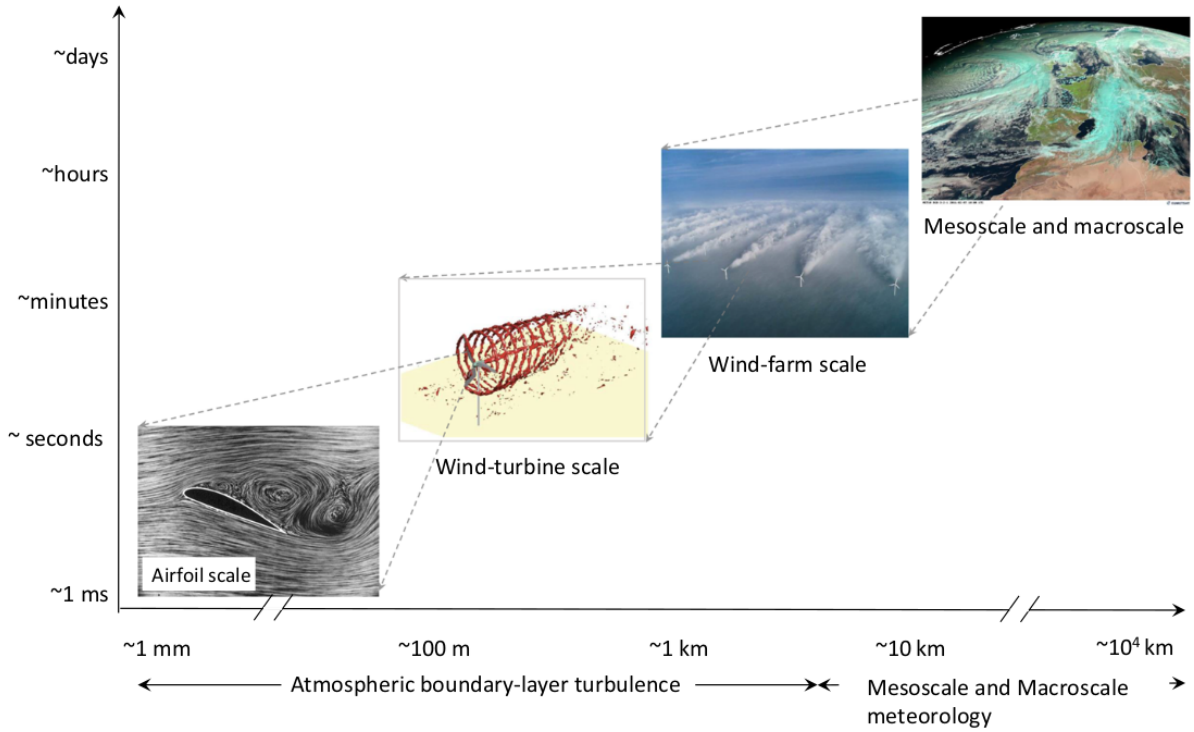

Source: (Porté-Agel; Bastankhah; Shamsoddin, 2020)

1.3 RESEARCH GOALS

To meet future demand of wind energy, additional research and explorations are needed. The ability to design larger wind turbines and optimized wind farms depends directly on the capacity of understanding the physics involved in the whole process of wind energy extraction. Multiple research areas surround a wind energy project: aerodynamics, aeroelasticity, structures, control, materials, manufacturing, installation, and for the offshore case, hydrodynamics.

The present work is particularly interested in the aerodynamics of wind turbines, which may include in turn several topics such as: aerofoils, dynamic stall, vortex ring state, vortex to vortex interactions, turbulence, complex inflow, upscaling, blade-vortex interactions, near-wake, wake interactions, load and power performance etc. (Vermeer; Sørensen; Crespo, 2003). We focus on wake interactions, analyzing near-wake structures, power performance and load analysis for models comparison.

For this purpose, the work investigates CFD rotor modelling with actuator disc and actuator lines, analyzing the impact of numerical parameters that are not completely clear in the research community today. After validating their usage by comparing with well consolidated models, their results for offshore wind turbines will be analyzed for one single turbine and two turbines in tandem configuration. Two types of offshore wind turbines

were used, one with a power capacity of current operational wind turbines (5 MW), and a larger one, to represent the future capacity (15 MW).

The objective is to clarify the understanding of such models, obtain new results for large offshore wind turbines, and push the limits of the knowledge frontier towards reliable simulation results for the wind energy community. Beyond any doubt, the findings by the research community are absolutely valuable for future energy projects, and will certainly impact society.

1.4 STRUCTURE OF THIS THESIS

The remainder of this master thesis is organized into four other chapters. Chapter 2 presents the *Fundamentals* of wind turbine modelling, introducing rotor models and numerical tools for simulation. Chapter 3 summarizes the *Literature Review* of the subject, in which concepts are discussed in depth and the recent literature results are examined. Chapter 4 presents and discusses the main *Simulation Results* obtained in this work. Finally, chapter 5 is the *Conclusion*, which summarizes the findings and suggests possible works for the future.

2 FUNDAMENTALS

To predict the loads and performance of wind turbines, it is essential to be capable of modelling them. The oldest mathematical representation of a screw propeller or wind turbine in fluid dynamic calculations is the classical actuator disc in axial flow proposed by Froude (1889) as a continuation of the work of Rankine (1865) on the momentum theory for propellers. This model has been used to represent wind energy turbines, but also for ship propellers and helicopter rotors.

An important extension of the actuator disc momentum theory was given by Glauert (1935), it is the so called blade element momentum theory, written shortly as BEM or BEMT. This improved model assumes that each annulus of the disc is independent, and the loads of each blade section are computed using two-dimensional aerofoil data. In addition, it can use a tip correction factor, firstly developed by Prandtl (1919), to account for the effect of a finite number of blades with finite length and three-dimensional effects at the tip.

This model can be coupled with the Navier-Stokes equation using computational fluid dynamics (CFD) for analyzing not only the turbine performance but also how the flow is affected by the turbine. An improvement of the actuator disc model (ADM) in CFD is the actuator line model (ALM), proposed by Sørensen and Shen (2002). The significant difference is that the ADM provides an axisymmetric result, while the ALM, by representing each blade by a line of actuator points, leads to a much more detailed wake near the rotor, with turbulence and coherent structures such as tip vortices. The following sections will describe these models.

2.1 ACTUATOR DISC CONCEPT

The most simplified concept to model a wind turbine rotor or a propeller is the actuator disc model (ADM). It consists basically of representing the rotor using a permeable and thin disc as schematized in Fig. 11 as a grey disc.

Since the wind turbine extracts kinetic energy from the wind to convert it into electrical energy, the wind slows down when passing through the rotor region. It is interesting to visualize what happens to the flow considering a stream tube passing exactly through the disc (Fig. 11). By mass conservation, if the air is not compressed, the upstream stream tube diameter must be smaller, and the downstream stream tube diameter must be larger than that of the disc.

Figure 12 depicts what happens with the wind velocity, in the axial direction, and pressure inside the stream tube. The wind speed far from the disc is U_∞, and this speed decreases continuously until it reaches the value U_W in the wake region. Regarding the pressure, it assumes the value of the atmospheric pressure, p_∞, far from the disc. When the wind approaches the rotor, the static pressure increases along the streamline and there is a

Figure 11 – Stream tube around the wind turbine rotor.

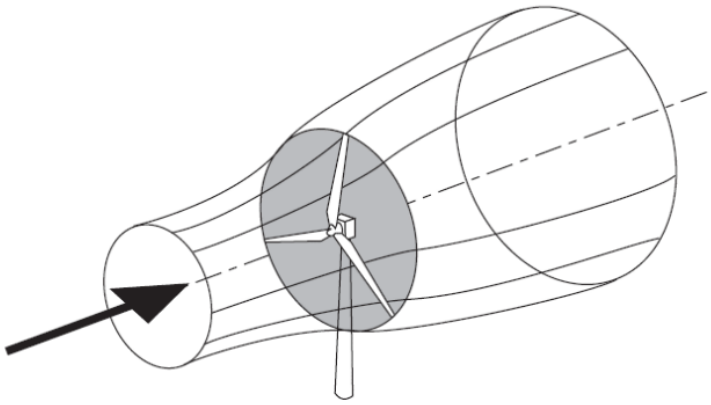

Source: (Burton et al., 2011)

Figure 12 – Velocity and pressure variation in the stream tube.

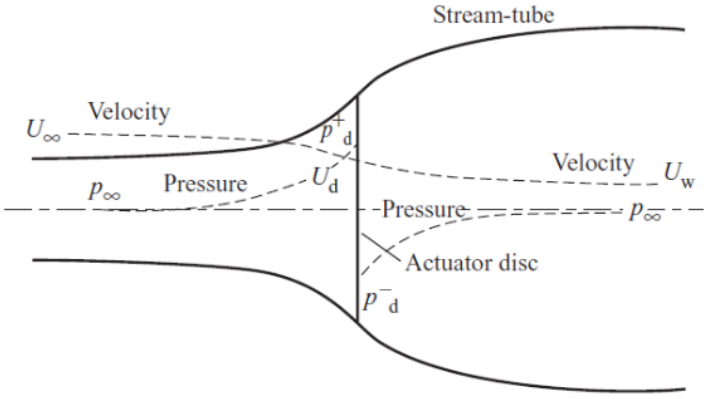

Source: (Burton et al., 2011)

discontinuity at the disc, where the pressure drop indicates the loss of mechanical energy. The axial velocity at the disc is decreased by the axial flow induction factor represented by the letter a. Thus, the velocity on the disc can be written as

$$U_D = U_\infty(1 - a).$$

This is known as the axial momentum theory, which is essentially uni-dimensional. Thus, from the Bernoulli equation applied separately to the upstream and downstream sections of the streamtube (separate equations are necessary because the total energy is different upstream and downstream), it can be demonstrated that the wake velocity is

$$U_W = U_\infty(1 - 2a).$$

Hence, the velocity U_D at the disc is the average between the far velocity U_∞ and the wake velocity U_W.

Froude (1889) also demonstrated that the force applied by a screw propeller is

$$T = 2\rho A_D U_\infty^2 a(1 - a), \tag{1}$$

and the power

$$P = 2\rho A_D U_\infty^3 a(1-a)^2. \tag{2}$$

It is very useful to define non-dimensional parameters to evaluate power and thrust. In this context, the thrust coefficient can be defined as

$$C_T = \frac{T}{\frac{1}{2}\rho A_D U_\infty^2} \tag{3}$$

or, by substituting Eq. (1),

$$C_T = 4a(1-a). \tag{4}$$

Similarly, the power coefficient can be defined as the ratio between the turbine power and the available power in the flow

$$C_P = \frac{P}{\frac{1}{2}\rho A_D U_\infty^3} \tag{5}$$

or, substituting Eq. (2),

$$C_P = 4a(1-a)^2. \tag{6}$$

So, it is easy to express the induction factor a in terms of C_P and C_T by dividing Eq. (6) by Eq. (4):

$$a = 1 - \frac{C_P}{C_T}. \tag{7}$$

This model is implemented in OpenFOAM under the class *actuationDiskSource*.

A very interesting result obtained by Betz (1920) is the maximum achievable value of the power coefficient, also known as the Lanchester-Betz limit. The maximum power coefficient occurs when

$$\frac{dC_P}{da} = 4(1-a)(1-3a) = 0,$$

which gives the optimum value for $a = 1/3$. Therefore,

$$C_{P_{max}} = \frac{16}{27} = 0.593.$$

This is related to the stream tube expansion upstream of the actuator disc because the power is available from a cross section of wind smaller than the disc.

2.2 ROTOR DISC THEORY

Additionally to the one-dimensional axial momentum theory, the angular momentum theory (Joukowsky, 1912) accounts for the rotational flow caused by the turbine rotor angular velocity. Essentially, the generated power comes from the torque applied by the fluid on the rotor. Consequently, a reaction torque must arise on the flow, causing the air to rotate in the opposite direction. The angular momentum gained by the air persists along with the wake, producing a helical flow. The kinematics of this flow is illustrated in Fig. 13.

Figure 13 – Angular velocity gained by the flow in opposite direction of the rotor rotation.

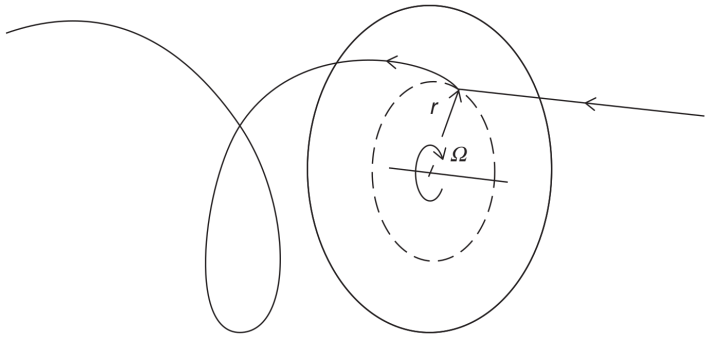

Source: (Burton et al., 2011)

While in the axial direction the flow experiences the decrease of momentum expressed by the axial induction factor a, in the tangential direction it experiences the increase of momentum expressed by the tangential induction factor a'. At the disc, the flow velocity is $\Omega r a'$, and in the wake, it is $2\Omega r a'$.

The torque can be defined as:

$$Q = \rho A_D U_\infty (1-a) 2\Omega a' r^2. \tag{8}$$

By the relation $P = Q\Omega$, and using Eqs. (2) and (8), the relation between the axial and tangential factors can be found:

$$a(1-a) = \lambda_r^2 a',$$

where λ_r is the local speed ratio, defined as

$$\lambda_r = \frac{r\Omega}{U_\infty}.$$

At the edge of the disc, $r = R$, and $\lambda = \frac{R\Omega}{U_\infty}$ is known as the *tip speed ratio*. Physically, λ is how fast the tip blade moves compared to wind speed far away.

It is interesting to point that, even with the additional tangential velocity, the maximum theoretical power coefficient is the same as for the non-rotating wake: the Betz limit. For further details about the momentum theory, Burton et al. (2011) provides an detailed presentation of the model.

2.3 BLADE ELEMENT MOMENTUM THEORY

The blade element momentum theory, usually referred to as BEM or BEMT, couples the one-dimensional momentum theory presented in sections 2.1 and 2.2, with the blade element theory, which assumes that the forces on the blade can be computed using two-dimensional airfoil characteristics. The rotor is divided into small elements in

Figure 14 – Annular ring element of the BEM theory.

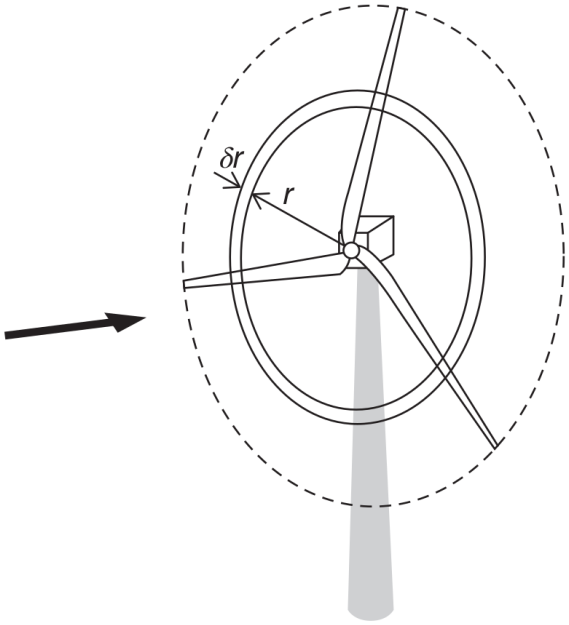

Source: (Burton et al., 2011)

the radial direction, which are the annular rings presented in Fig. 14. They are considered to be independent of each other, with no radial flow between the sections, which is a good approximation for most of the blade according to experimental data (Lock; Bateman; Townend, 1924). One should notice that this model neglects interaction between blades and all three-dimensional effects, so a tip correction may be necessary, and will be introduced in the next section.

The aerodynamic force of a single blade element is determined by its airfoil characteristics and the relative wind flow at that radial position. The sum of the contributions from all elements will provide the total torque and thrust.

In Fig. 15, the principal velocities and angles are presented for a blade element. The horizontal direction of the figure is the rotor plane, aligned with the tangential relative wind velocity $\Omega r(1+a')$, that is the sum of the blade rotation speed Ωr and the tangential induced wind velocity $\Omega r a'$. The vertical direction, aligned with $U_\infty(1-a)$, is the far wind direction. The angle β between the airfoil chord line and the plane of the disc is the twist angle, or the twist angle plus the pitch angle. The angle between the rotor plane and the relative wind velocity is ϕ. Finally, the angle of attack $\alpha = \phi - \beta$ is the effective angle for the computation of the aerodynamic forces.

Based on the tabulated airfoil data, the lift coefficient C_L and drag coefficient C_D are determined by the angle of attack α and the Reynolds number. The coefficients refer to forces in the streamwise direction for drag and transverse flow direction for lift. They

Figure 15 – Wind flow vector W relative to the blade element resulting in the angle of attack α.

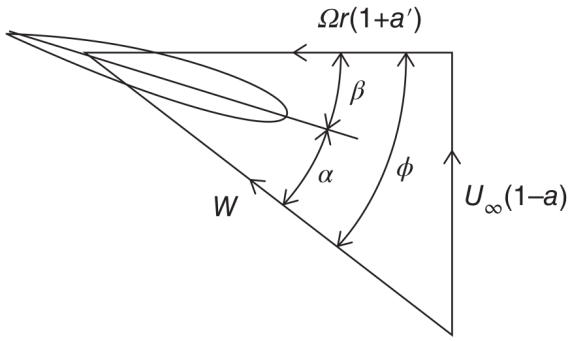

Source: (Burton et al., 2011)

Figure 16 – Corrected NACA64 airfoil coefficients of lift, drag and pitching-moment.

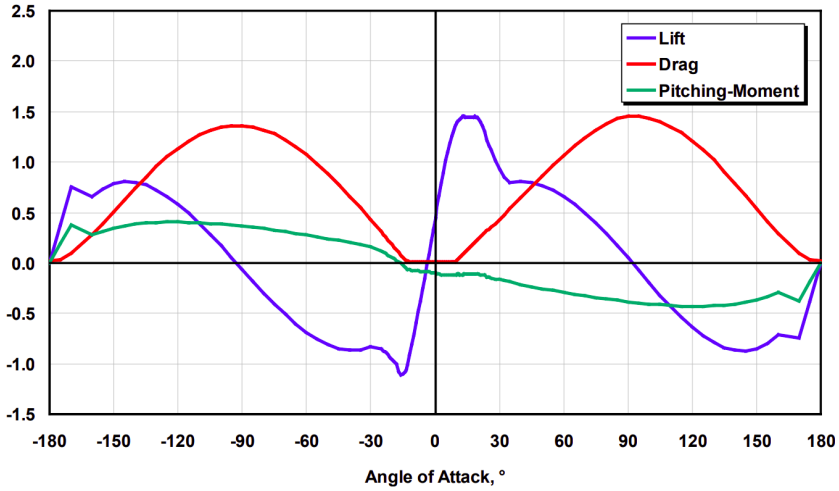

Source: (Jonkman et al., 2009)

are defined as follows:

$$C_L = \frac{L}{\frac{1}{2}\rho A W^2}, \tag{9}$$

$$C_D = \frac{D}{\frac{1}{2}\rho A W^2}. \tag{10}$$

L is the aerodynamic lift force, in the transverse flow direction, and D is the drag force, in the streamwise direction, A is the characteristic surface, in this case, the airfoil chord c times the spanwise blade element length δr. A typical tabulated airfoil coefficient is graphically represented in Fig. 16. It presents the corrected coefficients for the NACA64 airfoil, which constitute one third of the NREL 5 MW wind turbine blade. This offshore wind turbine is detailed by Jonkman et al. (2009). The corrections are made to better fit the two-dimensional data to three-dimensional experimental results. The pitching-moment, acting at the quarter chord point, tends to increase the β angle.

Usually, an airfoil is designed to provide high lift and low drag forces for small

Figure 17 – Aerodynamic forces acting on a blade section.

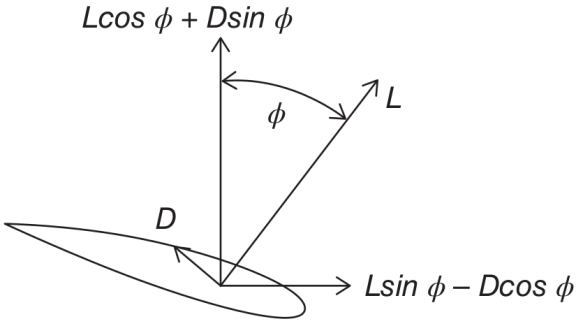

Source: (Burton et al., 2011)

angles of attack ($< 10°$). For greater angles ($> 15°$), it may stall, which means the lift sharply decreases and the drag increases. This effect may be desirable for some wind turbines under strong gust winds that should not overpass the maximum rotational speed, which could damage the electrical system. These turbines are referred to as stall regulated. However, most of the current wind turbines use active pitch control to regulate rotational speed, these are referred as pitch-regulated.

Once the aerodynamic coefficients are determined, the forces on each element are obtained from Eqs. (9) and (10), rearranged as

$$\delta L = \frac{1}{2}\rho W^2 c \delta r C_L, \tag{11}$$

$$\delta D = \frac{1}{2}\rho W^2 c \delta r C_D. \tag{12}$$

The forces acting on the blade element are presented in Fig. 17. The lift L and drag D are projected into the axial and tangential directions. The axial force is responsible for the thrust, calculated as

$$\delta T = \delta L \cos\phi + \delta D \sin\phi = \frac{1}{2}\rho W^2 B c (C_L \cos\phi + C_D \sin\phi)\delta r, \tag{13}$$

where B is the number of blades. The tangential force, multiplied by the local radius, produces the torque,

$$\delta Q = (\delta L \sin\phi - \delta D \cos\phi) r = \frac{1}{2}\rho W^2 B c r (C_L \sin\phi - C_D \cos\phi)\delta r. \tag{14}$$

In terms of the induction factors, the above expressions can be written as

$$\delta T = 2\pi r \delta r \rho U_\infty (1-a) 2a U_\infty, \tag{15}$$

$$\delta Q = 2\pi r \delta r \rho U_\infty (1-a) 2a' r^2 \Omega. \tag{16}$$

In order to obtain the torque and thrust, one may compute the induction factors by solving the following equations iteratively

$$\frac{a}{1-a} = \frac{\sigma_r}{4\sin^2\phi} C_x,$$
$$\frac{a'}{1-a'} = \frac{\sigma_r}{4\sin\phi\cos\phi} C_y,$$

where the chord solidity σ_r is defined as the total blade chord length at a given radius divided by the circumferential length around the annulus at that radius,

$$\sigma_r = \frac{Bc}{2\pi r}.$$

and the force coefficients in the axial and tangential directions are

$$C_x = C_L\cos\phi + C_D\sin\phi,$$
$$C_y = C_L\sin\phi - C_D\cos\phi.$$

Once the induction factors are determined, the total thrust and torque are obtained by integrating Eqs. (15) and (16) along the blade length. Finally, the power developed by the rotor is simply

$$P = Q\Omega, \tag{17}$$

where Ω is the rotational speed of the rotor. It is interesting to analyze the thrust and power in their non-dimensional form, which is expressed by the coefficients in Eqs. (5) and (3).

2.4 TIP LOSS

In a real rotor blade, the pressure at the tip must have a unique value due to continuity. As a result, the lift force must decrease to zero at the tip. Moreover, a spanwise pressure gradient develops near the blade tip, driving fluid from the pressure surface to the suction surface, leading to a radial flow component along the blade. Therefore, the lift component in the tangential direction will be smaller near the tip, as well as its contribution to the torque, Eq. (14). This effect implies a power reduction and it is known as *tip loss*.

To account for this three-dimensional effect, a tip correction must be incorporated to the BEM formulation. The first tip loss function was proposed by Prandtl (1919), and this correction factor is expressed by

$$F = \frac{2}{\pi}\cos^{-1}\left[\exp\left(-\frac{B(R-r)\sqrt{1+\lambda^2}}{2R}\right)\right]. \tag{18}$$

This function has a value of unity inboard and falls to zero at the edge of the rotor disc as shown in Fig. 18.

Figure 18 – Tip loss factor given by Eq. (18).

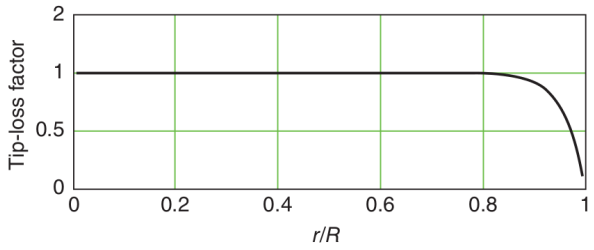

Source: (Burton et al., 2011)

Figure 19 – Root and tip loss factor.

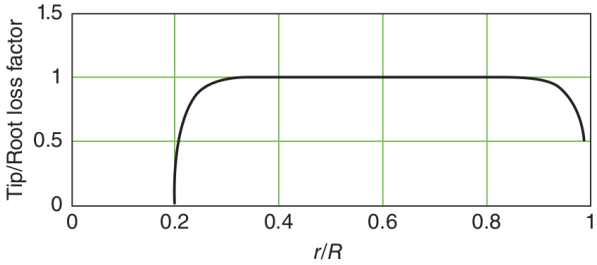

Source: (Burton et al., 2011)

Many other functions were proposed since then, and this is an ongoing topic of research (Wimshurst; Willden, 2017). Nonetheless, two functions are largely used by the research community and should be presented. One was proposed by Glauert (1935), expressed as

$$F = \frac{2}{\pi}\cos^{-1}\left[\exp\left(-\frac{B(R-r)}{2r\sin\phi}\right)\right]. \tag{19}$$

The other, more recent, was proposed by Shen et al. (2005), and reads

$$F = \frac{2}{\pi}\cos^{-1}\left[\exp\left(-g\frac{B(R-r)}{2r\sin\phi}\right)\right], \tag{20}$$

where

$$g = \exp\left[-c_1(B\lambda - c_2)\right] + 0.1 \tag{21}$$

with empirical coefficients c_1 and c_2 to be calibrated. For the NREL Phase VI rotor, an experimental wind turbine developed by NREL (Hand et al., 2001), it was found 0.125 and 21. Note that the three corrections are very similar in their formulation.

It is also possible to implement a similar correction at the blade root as the circulation must fall to zero like it does at the blade tip. Figure 19 shows the root and tip loss function for a blade root at 20% span.

2.5 CFD APPROACHES

The theory of rotor models presented in the previous sections (actuator disc, rotor disc, and BEM) can be implemented in flow solvers that use the Navier-Stokes

equations to analyze the wind turbine performance and the flow characteristics. Basically, it couples the forces computed by the rotor models and the velocities computed by the flow solver. The advantage of using computational fluid dynamics (CFD) is that more realistic conditions can be simulated with the addition of physical elements such terrain, atmospheric boundary layer (ABL), turbulence, multiple wind turbines, motion (for floating offshore wind turbines), aeroelasticity, and a variety of other conditions.

Additionally, in the CFD simulations the rotor models may vary in terms of complexity. It is possible to simulate a wind turbine using a very simplified model of actuator disc, in which the whole turbine geometry is modelled as a simple disc, or a very refined model, in which the tower, nacelle, and blades geometry are accurately modelled in a full blade-resolved simulation. An intermediate model, the actuator line, does not need to model the blade geometry explicitly, but still provides good details about the flow around the blades by using blade airfoil tabulated data.

This section presents the most relevant models available in OpenFOAM for wind turbine simulations, introducing the actuator disc models (ADM), the actuator line model (ALM), and the blade resolved approach. The last one is not in the scope of this work, but the reader should be aware of its advantages and drawbacks.

2.5.1 Actuator Disc Model

In the actuator disc model (ADM), the wind turbine geometry is not modeled in the grid, and this is an important advantage of this method in terms of mesh resolution and computation cost. Instead, the actuator disc (AD) models the wind turbine forces by extracting momentum from the Navier–Stokes equations with the addition of a momentum sink. For an incompressible case, the flow is governed by the following equations

$$\nabla \cdot \vec{u} = 0, \tag{22}$$

$$\frac{\partial \vec{u}}{\partial t} + (\vec{u} \cdot \nabla)\vec{u} = -\frac{1}{\rho}\nabla p + \nu \Delta \vec{u} + \vec{f}. \tag{23}$$

Equation (22) is an expression of the mass conservation and ensures the continuity of the flow, and Eq. (23), derived from Newton's second law of motion, is the momentum equation for fluid dynamics for incompressible and adiabatic flow. The last term, $\vec{f}$, is the source term, by which the actuator forces are applied in the flow.

The following subsections present the actuator disc models available in OpenFOAM, either in version 7 from openfoam.org, or version 1906 from openfoam.com.

2.5.1.1 actuationDiskSource

The most basic model of an actuator disc available in OpenFOAM is the *actuationDiskSource* class. It applies sources in the velocity field within a specified region to

enable actuator disc models to impose the thrust load of horizontal axis turbines in the surrounding flow field. The source term is uniformly distributed along with the disc, so it is also referred to as the uniformly loaded disc.

Two options for force computation are available: Froude's one-dimensional ideal actuator disc method and the variable-scaling actuator disc method. The first model uses the theory described in section 2.1, and for further details one may read Froude (1889) and Burton et al. (2011). For the second model, the principal references are Laan et al. (2015a) and Laan et al. (2015b).

This model is already implemented on a tutorial case named *turbineSiting*, in which two wind turbines are placed on a complex terrain geometry.

2.5.1.2 radialActuationDiskSource

This model is very similar to the *actuationDiskSource*, with the additional option of providing a radial thrust distribution for the thrust load at the rotor. This is done simply by multiplying the thrust magnitude computed by the Froude's method by a given fourth order polynomial function,

$$T(r) = T(C_0 + C_1 r^2 + C_2 r^4),$$

where T is the thrust computed with Froude's method, r is local radius, and C_* are the polynomial coefficients, which the user can define to fit the desired turbine characteristics.

2.5.1.3 rotorDiskSource

The most complex formulation of the actuator disc available in OpenFOAM, the *rotorDiskSource* class, brings two important improvements. One is the computation of tangential forces on the rotor plane, not only axial forces as the *actuationDiskSource* does, inducing a rotational flow in the wake more similar to the reality. The second change is the computation of aerodynamic forces using the BEM theory presented in section 2.3. In the *actuationDiskSource* model, the forces are calculated from integral coefficients (C_P and C_T), while in the *rotorDiskSource* the forces are computed from the airfoil characteristics. This allows a radial force variation according to the blade characteristics.

An important remark is that the original code was developed by Wahono (2013) to compute the aerodynamic forces of a helicopter rotor but it did not take into account axial inflow. In order to make it valid for wind turbine applications, it is necessary to add the correct force projections. Thus, the results obtained with this model may have nonphysical aspects, but illustrate the potential capabilities of the *rotorDiskSource*. Another remark is that the original code defines lift as the axial force and drag as the tangential force.

A detailed description and some proposed corrections for this model, as well as how to implement it, can be found in Patrao (2017) for a propeller performance estimation.

Figure 20 – A schematic of actuator line and actuator disc turbine models.

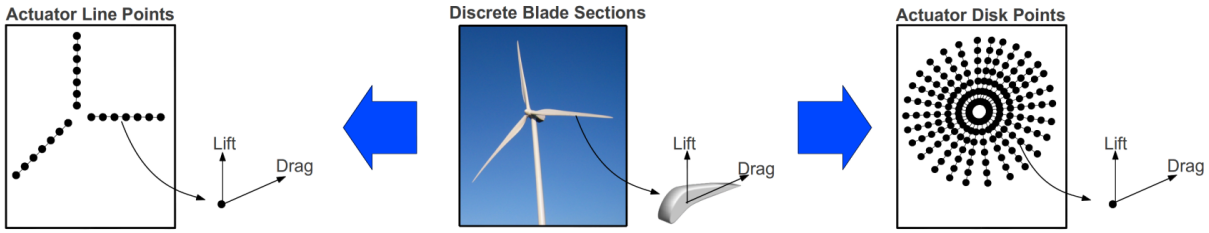

Source: (Martinez et al., 2012)

2.5.2 Actuator Line Model

The actuator line model (ALM) is an unsteady aerodynamic model that combines a three-dimensional Navier-Stokes solver with the technique in which body forces are distributed radially along each of the rotor blades. It was introduced by Sørensen and Shen (2002) to overcome limitations of the actuator disc model, notably its axisymmetric response. In the ALM, each blade is represented by a set of segments along its axis that rotates as a real rotor. Therefore, detailed dynamics of the different wake structures, such as the tip and root vortices, may be studied. The lift and drag forces of the blade elements are computed, as in the BEM theory, from tabulated airfoil data.

Both ADM and ALM do not simulate any wall, nor need to use a no-slip condition. Viscous effects from the boundary layer are introduced only as integrated quantities through the use of airfoil data (Sørensen; Shen, 2002). This is the main advantage of this kind of model because it does not require an extensive refinement near the blades, saving computational cost. For this reason, ADM and ALM are very useful tools for complex simulations, and thus, for real engineering applications. When the flow near the turbine is important to be analyzed, ALM should be chosen. For a global analysis, in which near wake structure details are not relevant, ADM may be more interesting. A comparison between ALM and ADM is shown in Fig. 20.

An important remark is that the grid mesh of this model is not dynamic. Only the location where the blade forces are applied, the actuator lines/points, rotates. The lift and drag airfoil forces are computed as in Eqs. (11) and (12), and similarly to BEM, C_D and C_L depend on the angle of attack and Reynolds number. However, the aerodynamic forces should not be applied at a single point, they need to be distributed smoothly on several mesh points to avoid numerical instabilities. In real life, the viscous and pressure forces act on the blade wall, but in the ALM model the force f of a singular actuator point is smeared along the grid mesh points by a three-dimensional Gaussian function as the following

$$f_\epsilon = f \otimes \eta_\epsilon, \qquad \eta_\epsilon = \frac{1}{\epsilon^3 \pi^{3/2}} \exp\left[-\left(\frac{d}{\epsilon}\right)^2\right] \tag{24}$$

where $d = |\vec{x} - \vec{e}_i|$ is the distance between the grid point and the ith actuator point, and

Figure 21 – NREL S826 airfoil mesh refinement for a blade-resolved simulation.

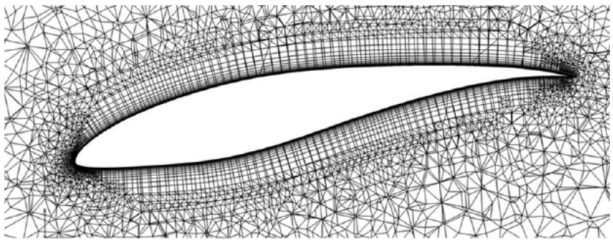

Source: (Mittal et al., 2016)

ϵ is the smearing factor, a parameter that determines how far the force is spread. This parameter is usually set between 2 and 3 times the grid cell size as recommended by Troldborg (2009), or 20% of the chord for finer mesh discretization as stated by Dağ and Sørensen (2020). The important of this parameter is further discussed in Section 3.4.1.

An additional use of the actuator lines or points is the modelling of tower and hub. Again, instead of representing the geometry of these elements by modeling a wall, it is possible to model them as fixed actuator points that only produce drag forces. A common setup is to define its drag coefficients based on cylindrical bodies.

The ALM formulation is not directly implemented in the OpenFOAM. However, the open-source code *turbinesFoam* provides a library that enables the use of this model. Section 4.1.2 introduces this useful tool. Several other codes use ALM formulation: Xcompact3d, developed by the Imperial College London, SOWFA, by NREL, and EllipSys3D, by DTU, are some examples.

2.5.3 Blade-Resolved

The final CFD modelling approach to be presented is the so called blade-resolved, the most expensive simulation in terms of computational cost, but also the one with the highest fidelity, since it models the full geometry of the wind turbine. Figure (21) presents the mesh refinement near the blade for the BT1 wind turbine. This turbine has 0.894 m of diameter, and a blade resolved simulation was conducted with 32 million nodes (Mittal et al., 2016). One may note the level of refinement near the wall blade, and how small the first elements should be to correctly compute the viscous boundary layer (in this case 0.006 mm).

This should be the most reliable method regarding the accuracy, but very difficult to use in practical applications, since it needs a lot of computational time to perform a single simulation of an isolated wind turbine. Hence, it is practically unfeasible, with this model, to simulate a complete wind farm in a reasonable time with the existing computational resources. For this reason, this type of simulation is not in the scope of the present work.

3 LITERATURE REVIEW

This chapter presents a literature review of the most important aspects of wind turbine modelling and the recent works on simulating the flow around wind turbines with actuator models. The state of the art and the future perspectives of this important research topic are described in the following sections. It begins by introducing the flow dynamics of wind turbines, and then it presents some of the relevant results available for actuator model simulations, discussing the importance of the main numerical parameters.

3.1 WIND TURBINE WAKES

The flow around a wind turbine can be divided in three separate regions: the induction region, the near-wake region, and the far-wake region. These regions are presented in Fig. 22 by the instantaneous and time-averaged flow. The upstream region where the presence of the turbine reduces the inflow velocity is the induction region. The downwind region is called the wake and is usually divided into the region immediately downstream of the turbine, called the near-wake, and the region further downstream, called the far-wake.

The near-wake is up to one rotor diameter downstream according to Vermeer, Sørensen and Crespo (2003), but it is also stated that it can have a length of 2-4 rotor diameters according to Porté-Agel, Bastankhah and Shamsoddin (2020). In this region, the flow is affected by the number of blades, hub and nacelle geometry, blade aerodynamics, including stalled flow, three-dimensional effects, and tip vortices. Therefore, it has a highly complex and heterogeneous flow field.

The far wake is the region beyond the near wake, where global wind turbine parameters, such as thrust and power coefficient, and inflow conditions are likely enough to describe the mean flow distribution (Porté-Agel; Bastankhah; Shamsoddin, 2020). Hence, modelling the actual rotor is less important to understand the influence of wind turbines in farm situations (Vermeer; Sørensen; Crespo, 2003).

The evolution and stability of tip and root vortices have been studied numerically and experimentally. The main focus has been given to tip vortices as they are the most persistent coherent structure (Sherry; Sheridan; Jacono, 2013). Wind tunnel with PIV measurements reported that tip vortices have some random fluctuations around their statistically averaged position, a phenomenon referred to as *vortex wandering* or *vortex jittering* (Heyes; Jones; Smith, 2004). According to these authors, vortex wakes exhibit unsteadiness from sources other than turbulence. The mutual inductance instability results in the pairing of tip vortices and ultimately their breakdown (Eriksen; Krogstad, 2017). Furthermore, under turbulent boundary-layer inflow conditions, the lifetime of tip vortices is significantly reduced due to the relatively high turbulence intensity and wind shear (Khan; Odemark; Fransson, 2016).

Wake meandering relates to the random unsteady oscillations of the entire wake with

Figure 22 – Schematic flow regions around a wind turbine subject to a turbulent boundary layer. The instantaneous (top) and time-averaged (bottom) flow features are presented.

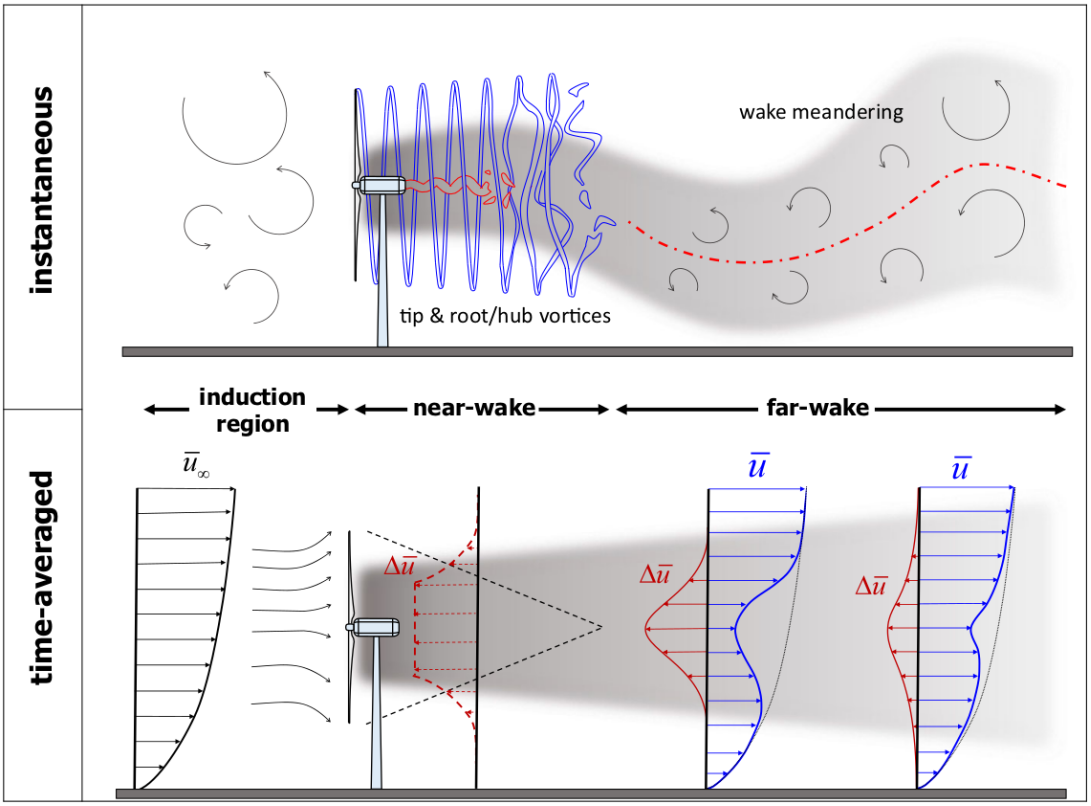

Source: (Porté-Agel; Bastankhah; Shamsoddin, 2020)

respect to the time-averaged wake centre-line. Some authors state that wake meandering is caused by very large turbulent eddies in the incoming boundary layer (Porté-Agel; Bastankhah; Shamsoddin, 2020). According to Larsen et al. (2008), the wake recovery is governed by small turbulent eddies, but the whole wake is advected passively by turbulent eddies larger than twice the rotor diameter. A commonly reported characteristic of wake meandering is that lateral displacements are much more pronounced than vertical ones.

The power losses due to interactions of wind turbine wakes in wind farms stimulated the development of wake mitigation strategies. By intentionally reducing the performance of a single wind turbine it is possible to improve the whole wind farm power production. The most effective strategy is the use of yaw angle control to deflect the wakes away from the downwind turbines (Schottler et al., 2017). The wake deflection increases with: the increase of yaw angle, the increase of thrust coefficient, the decrease in incoming turbulence intensity, and the increase of thermal stability (Churchfield et al., 2016). This suggests that the yaw-angle control of wind turbines could work well for offshore wind farms.

It is known that thermal effects play a significant role in wind turbine performance and wake flows (Porté-Agel; Bastankhah; Shamsoddin, 2020). Thermal stability affects the mean shear and turbulence intensity of the incoming flow as demonstrated by experimental

data (Machefaux et al., 2016) and numerical simulations (Abkar; Porté-Agel, 2015). These studies found that turbine wakes recover considerably faster and display stronger meandering in the convective boundary layer (CBL) compared with the neutral ABL and the stable boundary layer (SBL), due to higher turbulence intensity. This impacts the diurnal cycle, as the power deficit due to turbine wakes is considerably smaller during the daytime (CBL) than during the night (SBL).

3.1.1 Wind Farms

As the flow around a single turbine is stratified into different regions, the flow around and inside wind farms can also be separated into different zones. Similarly as the upwind region of one turbine, the flow immediately upstream of the wind farm is the wind farm induction zone, where a cumulative blockage effect induced by the wind farm as a whole decelerates the incoming boundary layer flow and deflects it upwards due to mass conservation. Branlard (2017) showed that the wind speed may easily decrease 3% at a distance of 2.5 diameters upstream the wind farm.

Right after the leading edge of the wind farm is the entrance and flow development region, where there is the growth of an internal boundary layer (IBL) following Elliot's $x^4/5$ power-law (Elliott, 1958). In the case of sufficiently large wind farms, the IBL may grow until it reaches the ABL, receiving momentum from the free atmosphere. The growth of the IBL together with the ABL continues further downstream until it reaches the fully developed state. In this zone, the averaged flow is homogeneous in the streamwise direction and the power extraction by the wind turbines is exclusively balanced by the turbulent vertical transport of kinetic energy from the flow above. This asymptotic case is also referred to as infinite wind farm case. Numerical studies by Wu and Porté-Agel (2017) have shown that this regime is attained after two or more orders of magnitude larger than the ABL height.

Close to the trailing edge of the wind farm, there may be an exit region, where a large acceleration improves the wind turbines performance (Wu; Porté-Agel, 2017). Finally, downwind of the wind farm, there is the wind farm wake region, where the absence of turbines induces an accelerating flow and downward flux of mean momentum due to mass conservation. This zone can persist for a range of 5–20 km and is important for farm-to-farm interactions in high wind energy regions.

Some studies analyzed the effect of wind farms on local meteorology. For example, Roy, Pacala and Walko (2004) showed that wind farms may have a significant impact on near-surface air, usually warming and drying it. Also, wind farm parametrization can be implemented in weather and climate model by the addition of surface roughness length, usually in global climate models (GCM), or as an elevated sink of momentum and source of turbulent kinetic energy (TKE), in mesoscale numerical weather prediction (NWP) models.

A common issue in onshore wind farms, unlike offshore, is that the terrain topography may have a major impact on the inflow conditions. This topic is specially critical because most of the research on the aerodynamics of wind farms is limited to flat terrains. In order to model the effect of topography in a simple manner, a straightforward idea is to simply superpose the turbine wake flow (on flat terrain) over the topography flow (without turbines). However, some inaccuracies may arise due to the non-zero pressure gradient, elevation of the wake, and flow separation.

It is common to perform studies with Gaussian or sinusoidal hill geometries.Yang et al. (2015) compared LES simulations and experimental tunnel data of a turbine placed downwind of a sinusoidal hill and observed a faster wake recovery because of the increased entrainment of ambient flow into the turbine wake, which is due to the enhanced turbulent transport in both spanwise and vertical directions. Regarding wind farms placed on wide hills, Politis et al. (2012) found that a turbine placed on top of a single Gaussian hill has a slower wake recovery. It has been shown (Shamsoddin; Porté-Agel, 2017) that the pressure gradient can noticeably affect the wake recovery in such a way that wakes recover faster under favorable pressure gradient and slower under an adverse pressure gradient.

A detailed review of wind turbine and wind farm flows is presented in Porté-Agel, Bastankhah and Shamsoddin (2020).

3.1.2 Wake Modelling

Regarding wind turbine wakes, the most simple way to model this phenomenon is utilizing an analytical formulation. Several analytical models have been proposed for the prediction of the average velocity deficit on the wake region and are used by commercial and open-source software as WAsP, from DTU, and FLORIS, from NREL. One of the pioneering analytical wake models, proposed by Jensen (1983), assumes a top-hat shape for the velocity deficit in the wake. The problem is that it tends to underestimate the velocity deficit at the wake centre and overestimate it at the edges of the wake. To overcome this issue, Bastankhah and Porté-Agel (2014) proposed a new model based on a Gaussian distribution that has a better agreement with experimental wind tunnel data.

These analytical models have low computational cost ($\sim 10^{-3}$ CPU hours per simulation) and are very useful for optimizing layout and control of wind farms over flat terrain with techniques that generate thousands of cases. There are also analytical formulations for the vertical distribution of the mean area-averaged wind speed in infinite (fully-developed) wind farms, as proposed by Abkar and Porté-Agel (2013).

Whenever more sophisticated turbulence resolving numerical tool is needed, one must solve the Navier-Stokes equations with computational fluid dynamics (CFD).

3.2 COMPUTATIONAL FLUID DYNAMICS

The Reynolds-averaged Navier–Stokes (RANS) technique has been extensively used to study wind turbine flows. However, with the fast growth of computational power, important progress has been made in the last decade in the development of large eddy simulations (LES) for wind energy applications. Despite the relatively high computational cost of LES ($\sim 10^3 - 10^4$ CPU hours per simulation), it can yield accurate simulations of realistic turbulent ABL flow around wind turbines and wind farms (Stevens; Martínez-Tossas; Meneveau, 2018). Nonetheless, LES of complex turbulent flows is known to be sensitive to the parametrization of subgrid-scale turbulent fluxes and forces, including turbine induced forces (Porté-Agel; Bastankhah; Shamsoddin, 2020).

For more than a decade, LES has been used with actuator models to study wind turbine flows (Revaz; Porté-Agel, 2021). This approach, together with wind tunnels experiments, field measurements, and analytical modelling, are providing important insights for wind turbine flow dynamics. Breton et al. (2017) provides a survey of modelling methods for high-fidelity wind farm simulations using LES and some of the available experimental data from wind tunnels and field measurements.

LES has the advantage over most RANS models in that it can properly reproduce the dynamics of the unsteady anisotropic turbulent atmosphere. It resolves the largest and most energetic turbulent structures, and models the smallest length scales providing more accuracy than RANS while demanding less computational cost than direct numerical simulation (DNS). In contrast to RANS, where the computational cost is only weakly dependent on the Reynolds number (Re), the computational cost of LES scales roughly with Re^2. Close to solid boundaries, where there is a boundary layer, LES is extremely expensive because it requires refinement in three directions, whereas RANS only requires refinement in the direction normal to the wall (Sanderse; Pijl; Koren, 2011). A possibility is to employ a hybrid approach: RANS to resolve the attached boundary layers and LES outside the wall region, so-called detached eddy simulation (DES).

Regarding LES simulations, the numerical details may have different effects for non-turbulent inflows and realistic turbulent flows. According to Revaz and Porté-Agel (2021), most of the works on the sensitivity of actuator models were performed based on the simplest case, and there is a need for further studies with realistic turbulent inflows, accurate measurements of the flow, thrust and power, and accurate description of turbine geometry and aerodynamic behavior of the turbine blades.

Finally, it is important to mention that the process of testing a CFD model consists of two steps: verification ('solving the equations right') and validation ('solving the right equations'). The first step evaluates the errors of approximating the continuous equations by discrete ones, here is for example the grid convergence study. And the second step requires comparison with experimental data to assess modelling errors, generally, from

turbulence modelling, blade approximation and inflow conditions (Sanderse; Pijl; Koren, 2011).

3.3 ACTUATOR MODELS

There are mainly three types of actuator models developed for rotor simulations. In chronological order, and also with increasing complexity and computational cost, they are: actuator disc model (ADM), actuator line model (ALM), and actuator surface model (ASM). The first two models are presented in Chapter 2, and the last and more recent one is described in detail by Shen, Sørensen and Zhang (2007). This model is an extension of the ALM but modelling each blade element with more actuator points to overcome the difficulty to represent the flow past an airfoil using only one point force as it is done by the actuator line. There is also a variation of the classical actuator disc model, that is the ADM with rotation (ADM-R) proposed by Wu and Porté-Agel (2011). This model is similar to the ALM, but with an increased number of actuator lines, such that the entire disc is formed. It can be seen as an ALM for which the forces are averaged over one rotational period. The advantage in comparison to the ALM is that the grid can be coarser and the drawback is that tip vortices are not captured.

Figure 23 illustrates the differences and similarities between the wake flow generated by ALM and ADM. Close to the rotor, on the left side of both images, the flow is significantly distinct because ALM provides detailed turbulent structures around the blade and tip vortices, while ADM gives an axisymmetrical result. However, far from the rotor, on the right side of both images, the flow is very similar as both present comparable flow structures.

Several studies on fully developed wind farm flows use the ADM version that only imposes a set of axial forces reconstructed from the thrust coefficient and the local flow velocity. The tangential forces are not of major importance for the main results according to Meyers and Meneveau (2010). It was also shown by Wu and Porté-Agel (2011) that

Figure 23 – Wake flow created by ALM and ADM, where the blue isosurface is of the second invariant of the velocity-gradient tensor and the contours are of streamwise velocity.

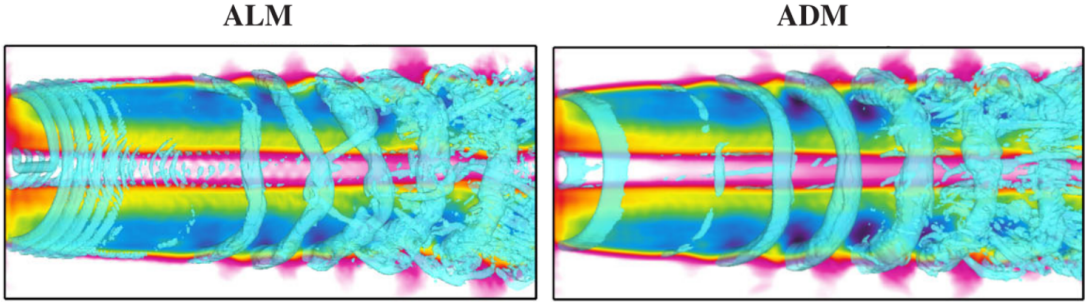

Source: (Martínez-Tossas; Churchfield; Leonardi, 2015)

the non-uniform force distribution is more important than the tangential forces for the improved accuracy of the flow prediction.

Comparisons with experiments demonstrate that the simplest version of the actuator disc, in which loads are constant, provides useful information about the overall flow behaviour for axisymmetric flow conditions, but important flow dynamics are not captured when the actual loading variation is not used (Sørensen et al., 2020). Simisiroglou et al. (2016) found that the shape of the force distribution can be felt in the wake at least five diameters downstream the turbine, which may impact the inflow conditions of the surrounding turbines in a wind farm. In addition, Porté-Agel et al. (2011) demonstrated that the azimuthal forces may also be important to capture the near-wake behaviour correctly. A study on how to include body forces, carried out by Laan et al. (2015a), showed that knowing the actual rotor loads provides a much more reliable simulations of the wake than simply assuming arbitrary shapes. In a recent study, Sørensen et al. (2020), proposed a general and universal analytical body force model that includes axial and azimuthal force distributions with no need for any prior knowledge about the turbine, excepts for the rated wind speed and nameplate capacity.

Regarding validation of CFD results, most of the wind tunnel experiments of the last decades have been carried out under uniform and nearly laminar inflow to study the airflow around wind turbines in free-stream (Vermeer; Sørensen; Crespo, 2003). Only in the last few years have experiments begun to investigate the interaction between turbulent boundary layer flows around wind turbines. They provided valuable information about the physics of wakes and turbulent structures and helped the validation of analytical and CFD models. In the field experiments, the early data was obtained using anemometers mounted on meteorological masts, and more recently, remote sensing technologies such as scanning wind lidars and radars are providing new insights and valuable data-sets.

3.4 SINGLE TURBINE

According to Porté-Agel, Bastankhah and Shamsoddin (2020), the prediction of wind turbine performance is complicated by the high Reynolds number of the ABL flow, its inherent unsteadiness due to the diurnal cycle and synoptic-forcing variability, the ubiquitous nature of thermal effects, and the heterogeneity of the terrain. The authors underline that the effect of ABL turbulence is particularly important for the wake flows and their superposition in wind farms, as they are responsible for power loss and fatigue loads. Consequently, improvements in the prediction of the flow behaviour under ABL conditions can potentially help increase the economic feasibility of wind energy projects.

The results provided by actuator models can be very sensitive to simulation parameters like grid resolution and how the actuator force is projected onto the flow field. A comparison study conducted by Martínez-Tossas, Churchfield and Leonardi (2015) showed

Figure 24 – NREL 5 MW power output as a function of grid resolution for different ϵ values at uniform inflow of 8 m/s.

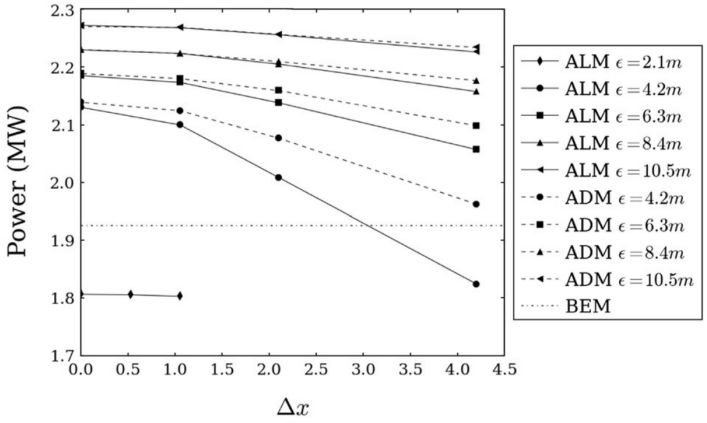

Source: (Martínez-Tossas; Churchfield; Leonardi, 2015)

that ALM is more sensitive than ADM, although for converged grids, power prediction differs by only 1%. It was found that the power prediction increases consistently with the smoothing parameter (ϵ) and a very small value must be used to accurately predict the power, that is why these models generally overestimate turbine power generation. Additionally, it was shown that for a constant ϵ, as the grid is coarsened, the predicted power decreases. Grid resolution and ϵ influence is shown in Fig. 24. The grid resolution must be smaller than the smoothing parameter, reaching grid independence for $\Delta_g < \epsilon/5$, and spurious numerical oscillations for $\Delta_g > \epsilon/2$, also observed by Troldborg (2009).

In OpenFOAM calculations of ALM, Arabgolarcheh et al. (2021) found an optimum mesh size with a balance between cost and accuracy for 80 grid elements per rotor diameter, for the two-bladed NREL Phase VI. A typical resolution would be 100 points along the rotor diameter, which is considered a very fine mesh since the flow itself would require a resolution in the order of 10 points for the same length (Porté-Agel et al., 2011).

Although Martínez-Tossas, Churchfield and Leonardi (2015) do not give a definite value, the authors show that ϵ should be around the size of the characteristic blade chord length, most likely, it should vary with span and should be some ratio of the local chord length. A recent evaluation of actuator disc models by Revaz and Porté-Agel (2021) found that the smoothing parameter has a strong impact on the rotor predictions and a moderate impact on the wake flow, so this parameter would not be so critical in studies focusing on the wake flow as it is for rotor predictions. It was also found that non-isotropic projections and grids should be used to optimize the computational setup. Further, the authors studied the effect of the nacelle and tower and concluded that their presence increase the velocity deficit in the near wake and reduce the rotor coefficients towards a better prediction. For the ADM case, it was found grid convergence for 10 grid points along each direction across the rotor.

Simulations conducted by Troldborg, Sorensen and Mikkelsen (2010) used a numer-

ical mesh with about 8.4×10^6 grid points to study the basic features of both the near and far wake. This provides an idea of the order of grid elements required for ALM simulations. The authors pointed out that in ALM the time step is mainly limited by the rotational speed of the rotor because the movement of the blade tip during one time step should not exceed the length of the cell. This latter requirement, sometimes referred to as $\mathrm{CFL_{tip}}$, is far more restrictive than the original CFL condition, and in all of the computations carried out the maximum CFL number rarely exceeded 0.2.

Troldborg, Sorensen and Mikkelsen (2010) evaluated different tip speed ratios (TSR) and showed that the higher the TSR, the faster the wake transits to a turbulent state. For a TSR = 11.78, the tip vortices completely broke down shortly downstream of the rotor, while for TSR = 7.07 the tip and root vortices were shown to become unstable approximately 5 rotor diameters downstream. For lower TSR ($\sim$ 5 and 3) the wake remained practically stable in the simulated domain.

Regarding the inflow condition, in Sørensen et al. (2020), the basic flow equation of momentum conservation used three force terms on the right hand side. Besides the turbine loads, there was the wind shear that prescribes the boundary layer, following the method described by Troldborg et al. (2014), and the turbulence introduction, after the synthetic atmospheric turbulence field previously generated using the Mann model (Mann, 1994).

3.4.1 The Smoothing Parameter

According to Ma et al. (2020), there is still confusion about the optimal value of the Gaussian width, and the effect of each parameter used in an isotropic kernel on an ALM simulation result is still unclear. The smoothing parameter ϵ will strongly affect the torque result in ALM simulations and it may not converge for large values. Larger ϵ causes an over-prediction of the normal velocity of each blade element but has little effect on the tangential velocity. Figure 25 illustrates the wake flow generated for different ϵ values.

The optimum smoothing length scale in the projection of body forces has been studied by several authors. Troldborg, Sorensen and Mikkelsen (2010) found a good compromise between reducing oscillations without smoothing out too much the oscillations for $\epsilon = 2\Delta_g$ for Cartesian grids. $\epsilon = 1.5\Delta_g$ lead to nonphysical oscillations. They also worked with polar grids, with fixed actuator lines, while a rotational velocity at the boundaries created the rotational reference frame. For the polar case, $\epsilon = \Delta_g$ was used. The agreement between the results of different grids was quite good, although the computation in the polar grid generally under-predicted axial and tangential induction.

Based on an analytical solution to the linearized inviscid flow response to a Gaussian force, Martínez-Tossas, Churchfield and Meneveau (2017) found that the optimal smoothing width should be on the order of 14%-25% of the chord length of the blade, and the position of force should be located at about 13%-26% downstream of the leading edge of the blade.

Ma et al. (2020) proposed an anisotropic regularization kernel, arguing that using

Figure 25 – NREL 5 MW vorticity contours predicted by the ALM (left column) and ADM (right column) for two different ϵ values. Mesh resolution of $\Delta_g = 1.05\,\mathrm{m}$

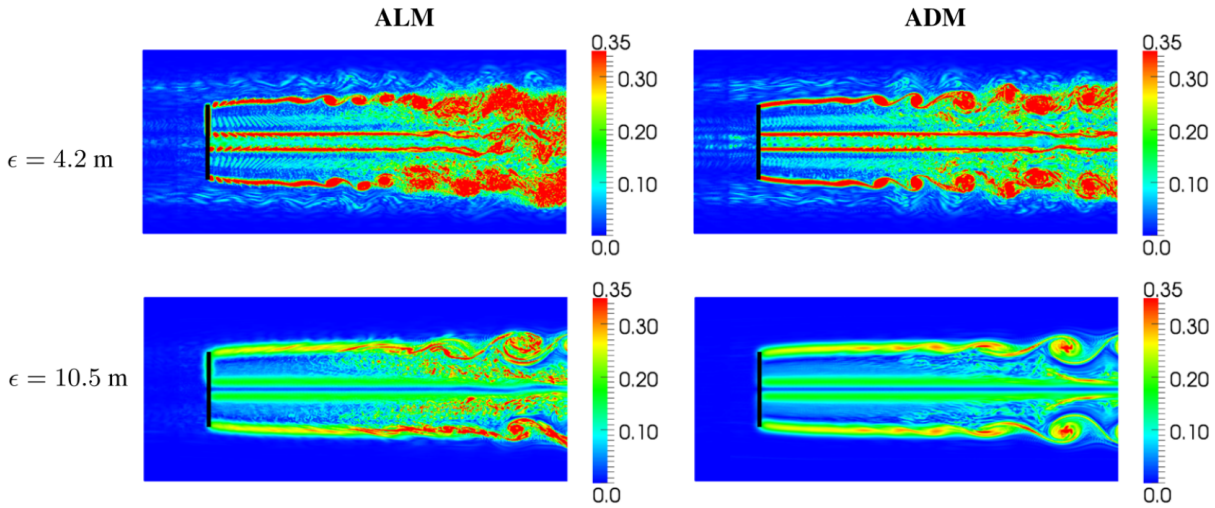

Source: (Martínez-Tossas; Churchfield; Leonardi, 2015)

the standard regularization kernel, the conceptual shape of a wind turbine blade will be like a cylinder, which is inconsistent with its real shape. Therefore, instead of one single ϵ, there will be three smoothing parameters, one for each direction of the local blade element coordinates. According to the authors, this approach is able to better model the shape of the wind turbine blades, alleviating the need of tip correction.

Recently, Jha and Schmitz (2018) proposed an advanced actuator line model to overcome some inconsistencies from force projection of the ALM, as the superposition of forces and projection of forces beyond the tip blade. The differences between the volumetric body force projection of ALM with constant ϵ, ALM* with ϵ varying with an elliptical chord c^*, and the proposed actuator curve embedding (ACE) model are illustrated in Fig. 26.

Figure 26 – Comparison between ALM force projection with constant ϵ with respect to the grid size or chord, versus ACE.

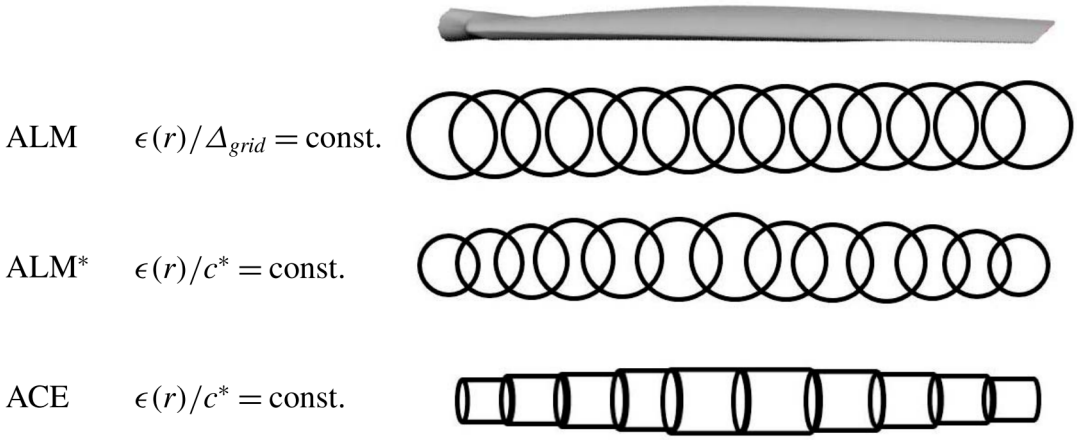

Source: (Jha; Schmitz, 2018)

3.5 TURBINES IN TANDEM

Recent numerical simulations were conducted using ALM implemented in OpenFOAM with the turbinesFoam library extension (Bachant; Wosnik, 2019) with LES and tip correction (Shen et al., 2005). Regarding horizontal axis wind turbines (HAWT), Onel and Tuncer (2020b) estimated the wake induced power loss with two NREL 5 MW aligned in tandem, and in Onel and Tuncer (2020a), the authors compared the effect of yawed configurations. They found typically the same trends previously presented when varying the numerical parameters: the predicted power increases with the smoothing parameter and grid resolution. A comparison between smoothing parameter based on the chord blade and grid size showed better prediction for the latter. The authors found a good compromise on accuracy and computational cost with 64 grid elements per rotor diameter, a smoothing parameter $\epsilon = 1.25\Delta_g$ and $\text{CFL}_{tip} = 1.80$. Under uniform or ABL inflow, for two wind turbines operating at the same fixed rotational speed, the turbine 7 diameters downstream presented an extremely high power loss of 86%, probably due to the absence of turbulence on the inflow, which leads to a slow wake recovery, and proper wind turbine control (the angular speed was kept constant). The large power loss found is in agreement with other ALM works (Schmitz; Jha, 2013) and blade-resolved RANS simulations (Miao et al., 2017).

For a yaw angle of 25° on the upstream turbine, Onel and Tuncer (2020a) found that the downstream turbine experiences a power loss of 32%. The reduction of wake loss in the yawed configuration overcomes the power loss (∼15%) of the upstream turbine that is not aligned with the mean wind. (Miao et al., 2017) showed that when the upstream wind turbine yaw 30° there is an increase of 2.3% of the total power. However, for −30° yaw, the total power may decrease 3.3% because the vortex structures display different behaviors according to the rotation and yaw direction.

A previous study with turbinesFoam was conducted by Yu, Zheng and Ma (2018) with RANS k-ω SST, and tip correction for NREL 5 MW simulations. The grid size near the rotor was around 3 m (42 elements per rotor diameter) with 3 million cells. Power and thrust coefficients were compared with BEM results and differed 5 and 6% respectively. Two turbines in tandem were analyzed spaced by 6, 7, and 8 diameters, while the TSR of the downstream turbine was fixed in a slightly lower value than the one of the upstream turbine (6.1 vs 7.55) for a uniform 8 m/s wind speed. A power loss of 60% was found, similar to results provided by Jha et al. (2014), where LES was used two evaluate the tandem configuration performed for a neutral boundary layer (NBL) and moderately-convective boundary layer (MCBL).

3.6 FLOATING OFFSHORE WIND TURBINES

Some studies were carried out with ALM applied to floating offshore wind turbines (FOWT). Li et al. (2015) underline that the degrees of freedom added by floating structures create components of wind speed that can lead to violation of conservation hypotheses of models traditionally used in fixed turbines, such as the BEM. Thus, using the ALM model, the authors simulated a FOWT with surge and pitch movements with typical frequencies. The results show that the surge movement has little effect on the integrated loads, while the pitch movement brings significant changes in the aerodynamic performance of the turbine.

A CFD solver using OpenFOAM has been developed by the University of Shanghai to simulate various hydrodynamic problems. One of the modules presented in Wang, Zhao and Wan (2019) is the ALM used to simulate a FOWT with 6 degrees of freedom coupled to the solver naoe-FOAM-SJTU. At each time interval, the aerodynamic forces calculated by the ALM are injected into the hydrodynamic model that calculates the new platform position.

Finally, the NREL (National Renewable Energy Laboratory) has been developing simulations with the Simulator for Wind Farm Applications (SOWFA) coupled with the OpenFAST software for platform and turbine movement. In Johlas et al. (2020), the ALM is applied in the study of the NREL 5 MW mounted on an OC3-UMaine spar platform and an OC4-DeepCwind semi-submersible. It was noticed that the FOWT wake is deflected upwards when compared to fixed turbines, and this phenomenon is more intense on the spar platform.

The trends and future challenges of floating offshore wind turbine aerodynamics are presented in Micallef and Rezaeiha (2021). Due to the multi-physical aspects and complexity of the problem, several research areas surrounds FOWT aerodynamics: hydrodynamics, manufacturing and installation, materials, control, structures, aeroelasticity, and of course, aerodynamics. The authors conclude that the existing literature has been focused on

isolated solo floating turbines, and studies on the interactions between the floating turbines are scarce. The majority of works analyzed the NREL 5 MW wind turbine. No work was indicated about the IEA 15 MW, but the challenge of compressibility effects is pointed as a challenge for 15 MW+ rotors of the future because of higher tip speed ratios.

3.7 FUTURE PERSPECTIVES

In Porté-Agel, Bastankhah and Shamsoddin (2020) some future perspectives of research questions that remain unanswered in wind turbine flows understanding are listed. Among others, the authors underline the necessity of extending analytical wake models to turbulence quantities, developing physics-based theory for wakes superposition in realistic flows, investigating further the role of atmospheric turbulence scales, thermal stability and topography on wind turbines, build computationally efficient models and strategies to predict the entire range of flow scales, particularly, coupling of coarse-resolution RANS-based weather models with high-resolution models, such as LES.

Regarding the fluid turbulence research, Meneveau (2019) poses seven questions which answers may lead to improvements in wind energy harvesting. In a nutshell, these questions underline the need for better analytical, synthetic and reduced order models of turbulence, better model coupling and basic understanding of flow phenomena governing kinetic energy entrainment and limiting power densities.

Further, Veers et al. (2019) outline three grand challenges in the science of wind energy. The first is to improve the understanding of atmospheric and wind power plant flow physics. Secondly, the aerodynamics, structural dynamics, and offshore wind hydrodynamics of enlarged wind turbines. The last, is systems science for integration of wind power plants into the future electricity grid. Since these challenges are interdependent, dealing with them is a role for integrative wind energy science. Engineering, science and mathematics are, therefore, imperative to develop innovative technologies, and a summary of the disciplines that covers wind energy science is presented in Fig. 27. Addressing these challenges could enable wind power to provide half of the global electricity needs and perhaps beyond.

The present work is an attempt to push the limits of the knowledge frontier in the subjects of wind turbine simulations. In particular, by understanding the nuances of actuator disc and line models and their capability of predicting turbine performance and flow dynamics.

Figure 27 – Spectrum of disciplines that, if integrated, can comprehensively address the grand challenges in wind energy science.

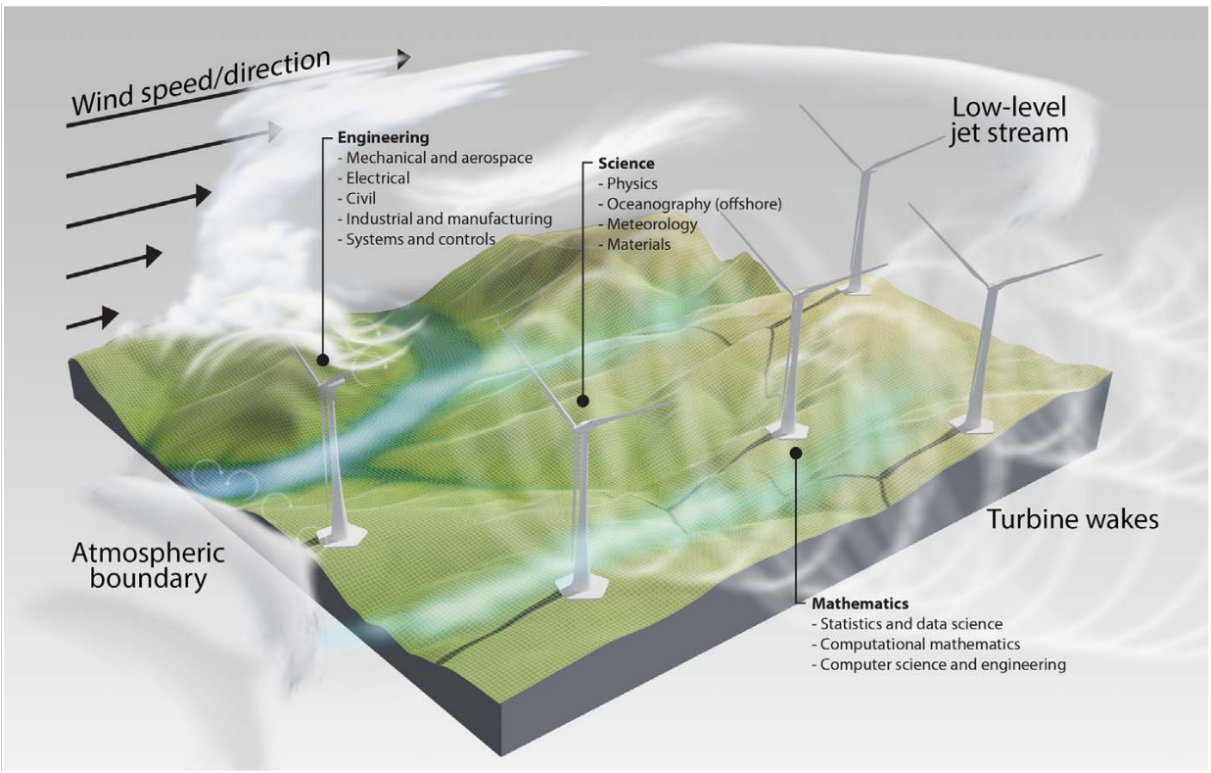

Source: (Veers et al., 2019)

4 SIMULATION RESULTS

Under the scope of the aerodynamic simulations, different numerical models of wind turbine rotors were investigated. They range from the most simplified model, the actuator disc, passing through the rotor disc, until a more complex model, the actuator line, with BEM theory comparisons.

This section begins by introducing the numerical tools used and then presents the main simulation results obtained with the previously described models. All the results refer to an isolated wind turbine rotor or two rotors in tandem configuration, with no tower and no ground, under uniform inflow. For the actuator disc simulations, turbulence was modelled with RANS and for the actuator line, it was modelled with LES.

4.1 NUMERICAL TOOLS

The most important numerical tools for wind turbine simulation used in this work are briefly described in this section. They are all open-source and under continuous development.

4.1.1 OpenFOAM

OpenFOAM (Open-source Field Operation And Manipulation) is an open-source toolbox mainly used for CFD applications based on the finite volume method (Weller et al., 1998). It was created in 2004 by OpenCFD and is written in C++. Currently, two main developers that provide the code: The OpenFOAM Foundation (openfoam.org) and ESI-OpenCFD (openfoam.com). The first releases its versions based on a sequence identifier (e.g. 7 for the seventh release), and the second based on date-of-release identifier *YYMM* (e.g. 1906 for the June 2019 release). This work used both releases as some functions available in one version may not properly work in the other.

Currently, there are three actuator disc models implemented in OpenFOAM: the *actuationDiskSource*, the *radialActuationDiskSource* and the *rotorDiskSource*, already described in sections 2.5.1.1 to 2.5.1.3. The numerical simulations of this work used the first and the last model.

4.1.2 turbinesFOAM

TurbinesFoam is an open-source library implemented in OpenFOAM that allows the use of the actuator line model for vertical or horizontal axis wind turbine applications. It was developed by Bachant, Goude and Wosnik (2016) who adapted functions such as interpolation, Gaussian projection, and vector rotation from NREL's SOWFA (Fleming et al., 2013). The great advantage of turbinesFoam is the inheritance of all the OpenFOAM functionalities, such as mesh generator, turbulence models (both RANS and LES), various

boundary conditions for uniform wind or atmospheric boundary layer (ABL), among others. However, a disadvantage of this software is the lack of an implemented control system, therefore the rotor must keep a fixed rotational speed and blade pitch throughout a simulation. Regarding this issue, the development of a control algorithm is desirable.

4.1.3 OpenFAST

OpenFAST, formerly known as FAST (Jonkman; Jr et al., 2005), is a multi-physics, multi-fidelity tool for simulating the coupled dynamic response of wind turbines. Mainly developed by NREL, it couples computational modules for aerodynamics, hydrodynamics, structural, control and electrical system dynamics to enable coupled nonlinear aero-hydro-servo-elastic simulation in the time domain. The module responsible for the aerodynamic calculations is AeroDyn, which has originally four sub-modules: rotor wake/induction, blade airfoil aerodynamics, tower influence based on potential flow, and tower drag. The BEM model has several available corrections such as Prandtl tip or hub-loss, skewed-wake, among others. Recently, a free vortex wake module named OLAF and an aeroacoustics model were included in AeroDyn.

4.2 ACTUATOR DISC MODEL

The simplest rotor model simulated in this work is the actuator disc. The results of the CFD simulations are presented in this section. It begins with a code improved by the author, followed by a single rotor under uniform inflow for three important wind turbines in the research community, the NREL 5 MW, DTU 10 MW, and IEA 15 MW, and then two turbines in tandem configuration. For these cases, turbulence has been modelled with RANS employing k-ε two-equation model, the most adopted one. The importance of the value of the turbulence variables at the inlet boundary is also discussed.

Firstly, the OpenFOAM class *actuationDiskSource*, described in section 2.5.1.1, was modified to compute the power and thrust based on the C_P and C_T turbine curves and the flow velocity at a user-defined upstream point, the U_∞. Once the coefficients are determined by the inflow velocity, the turbine thrust can be computed from the thrust coefficient definition, Eq. (3), and the turbine power computed from the power coefficient, Eq. (5).

However, none of these forces is directly applied on the flow. Instead, the CFD model applies only the thrust computed from the expression developed by Froude (1889) in Eq. (1), which is usually higher than the thrust computed from the coefficient definition, and take into account the induction factor a that couples C_P and C_T as shown in Eq. (7). The difference between the thrust computed from the definition of C_T and the expression from Froude (1889) is probably because C_P and the C_T from the turbine specification curves were computed by BEM with tip correction.

Figure 28 – Coefficient curves of power (a) and thrust (b) for three wind turbines: NREL 5 MW, DTU 10 MW and IEA 15 MW.

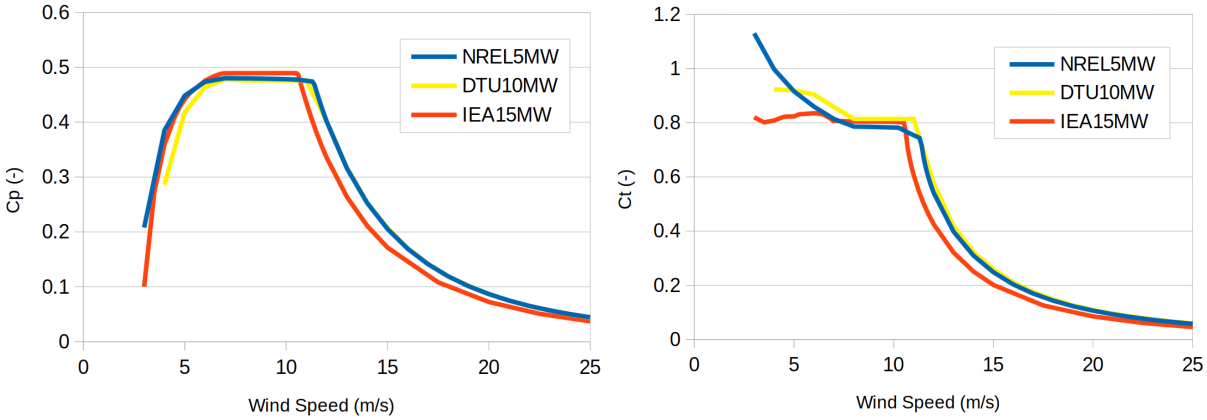

(a) Power coefficient.

(b) Thrust coefficient.

4.2.1 Setup

Three turbines, the NREL 5 MW, DTU 10 MW, and IEA 15 MW, were simulated with the same parametric mesh. The power and thrust coefficient curves are provided in Fig. 28. They were extracted from the respective wind turbine documentation.

One must notice that the OpenFAST rotor thrust variable (*RotThrust*) includes gravity and inertial terms, thus, in order to compute C_T, these terms must be subtracted. For a steady simulation, it means the extraction of the gravity term only, which in OpenFAST variables is:

$$\text{RotMass*Gravity*sin(ShftTilt+YawBrRDyt)} = 94.05\,\text{kN}$$

for the NREL 5 MW case. Where ShftTilt is the the angle (in degrees) between the rotor shaft and the horizontal plane, and YawBrRDyt is the tower-top/yaw bearing angular (rotational) pitch deflection (relative to the undeflected position).

The meshes used in the simulations were developed with the most basic mesh generator in OpenFOAM, the BlockMesh. It is a useful tool to create structured meshes and smoothly refined regions. Figure 29 illustrates a mesh of 1.7 mi elements used on ADM simulations of two turbines in tandem configuration located at the centre of the $y-z$ plane. The most refined region comprises the two rotors and the wake between them.

Simulations for a single turbine were conducted in meshes with $6D \times 6D \times 8D$ domain size, with the rotor placed $3D$ downstream the inlet, as some studies do for actuator line simulations. Regarding the domain for the tandem configuration, the first turbine was located $6D$ downstream the inlet, and the second $10D$ upstream the outlet boundary, both are $6D$ from the sides, top, and bottom. The grid size at the rotor, shown in Fig. 30, is 4% of its diameter, that is 5.04 m for the NREL 5 MW case.

Figure 29 – Mesh for two wind turbine rotors in tandem configuration.

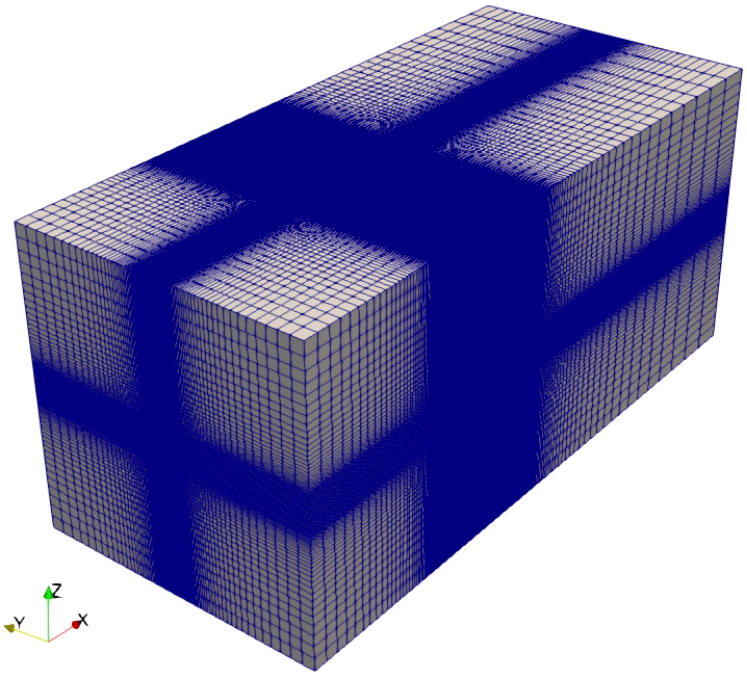

Figure 30 – Discretization of the actuator disc (front view) coloured by pressure for $U = 8m/s$.

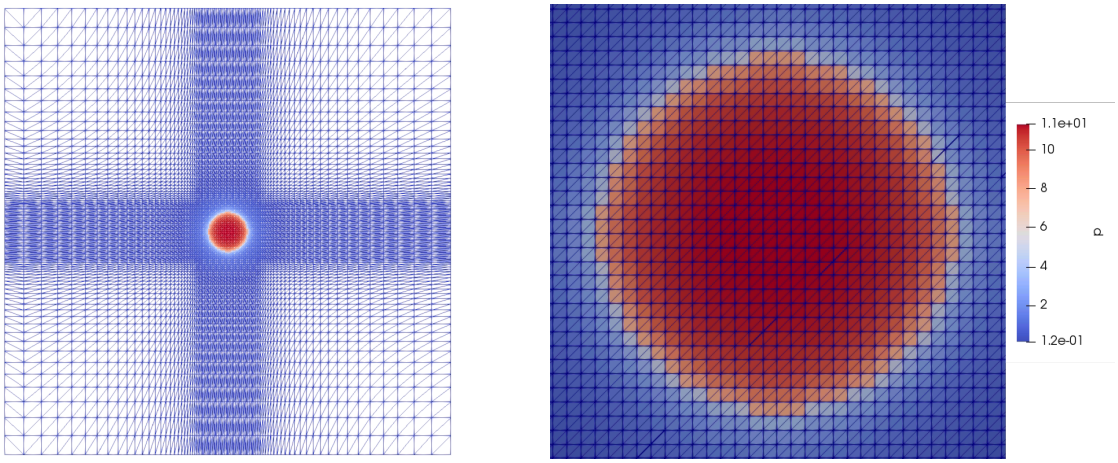

(a) Wide view.

(b) Close view.

Figure 31 – Actuator disc coloured by velocity magnitude (front view).

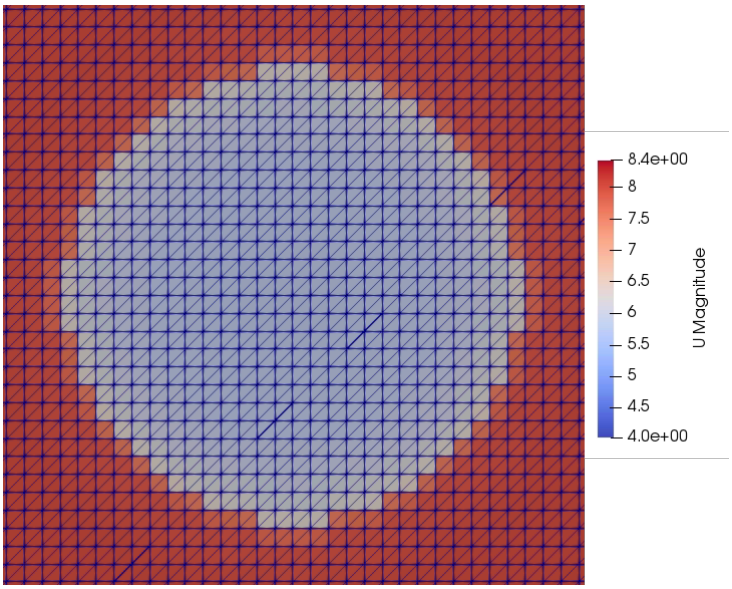

4.2.2 Results

Figure 30b presents the front side of the rotor disc as a high pressure region, and Fig. 31 shows that the disc is also a low velocity region. These two images exemplify a permeable disc, which is how the rotor is modelled by the ADM.

4.2.2.1 Single turbine

The results for a single turbine subjected to an inflow wind speed of 8 m/s is very similar for the three different turbines as shown in Fig. 32. The velocity fields are practically the same because the three turbines have nearly equal C_P and C_T at the referred wind speed. Thus, the non-dimensional results will be very similar although the dimensional ones (power and thrust) will definitely differ. Regarding the power, the turbines NREL 5 MW, DTU 10 MW, and IEA 15 MW generated 1.88 MW, 3.73 MW, and 6.94 MW respectively.

4.2.2.2 Two turbines

The velocity magnitude of two NREL 5 MW in tandem separated by $5D$ is shown in Fig. 33. The wake persists even $10D$ downstream the turbine, but is feeble. The pressure field, presented in Fig. 34, is uniform on the disc, as expected for this model, and smaller on the downstream turbine, as this turbine generates less power due to wake loss and consequently extracts less momentum from the flow.

In Fig. 35, the graph on the right shows the pressure (in red) and velocity magnitude (in yellow) plotted on the axial line passing through the center of two IEA 15 MW turbines aligned in tandem. One may visualize numerically what happens to these variables in the vicinity of the rotor and compare with the theory presented in section 2.1 and Fig. 12.

Figure 32 – Velocity field for a single actuator disc for three different wind turbines with the same parametric mesh.

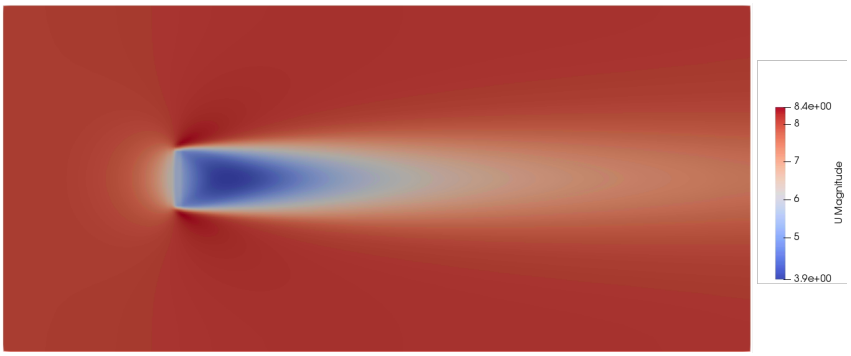

(a) NREL 5 MW.

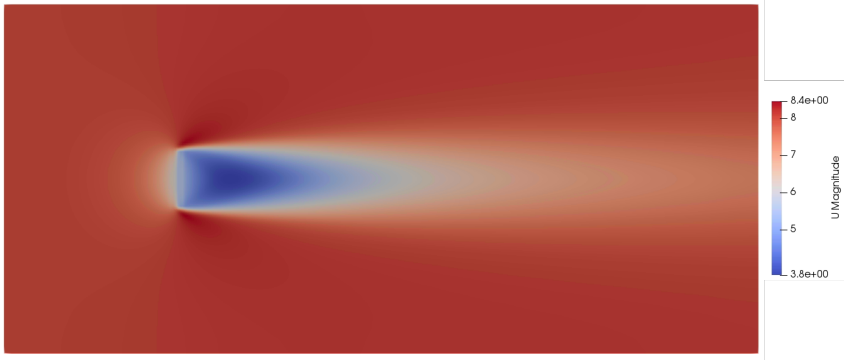

(b) DTU 10 MW.

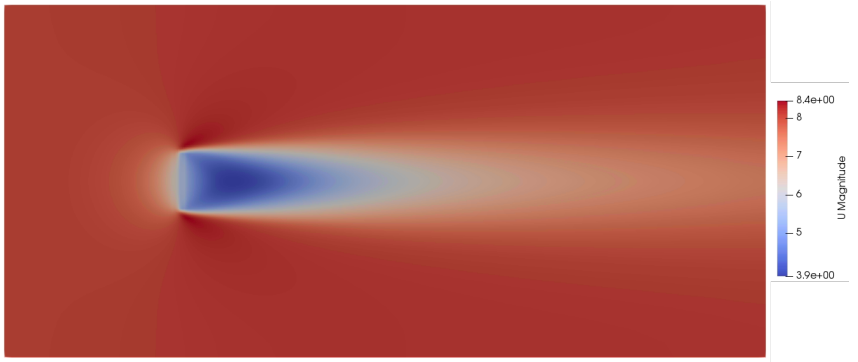

(c) IEA 15 MW.

Figure 33 – Velocity magnitude of two NREL 5 MW turbines in tandem with a larger domain.

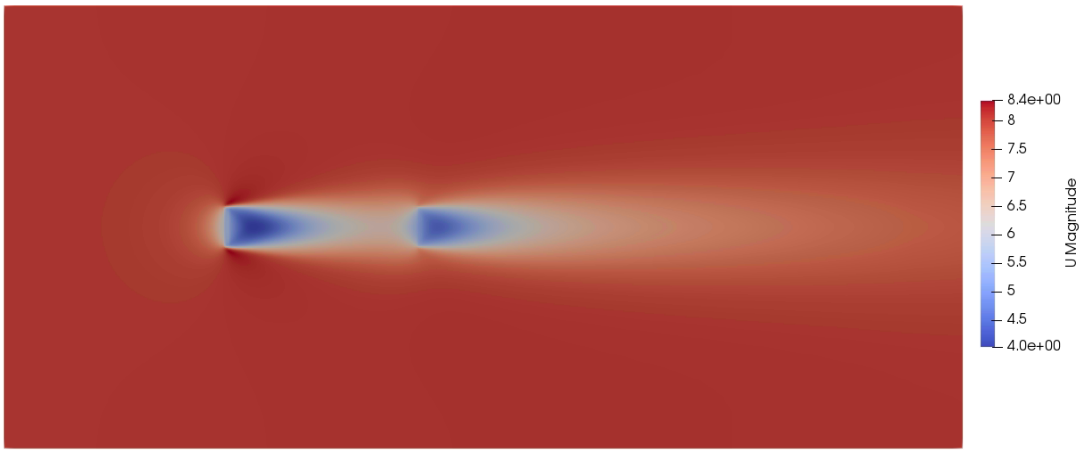

Figure 34 – Pressure field in the vicinity of two NREL 5 MW turbines in tandem.

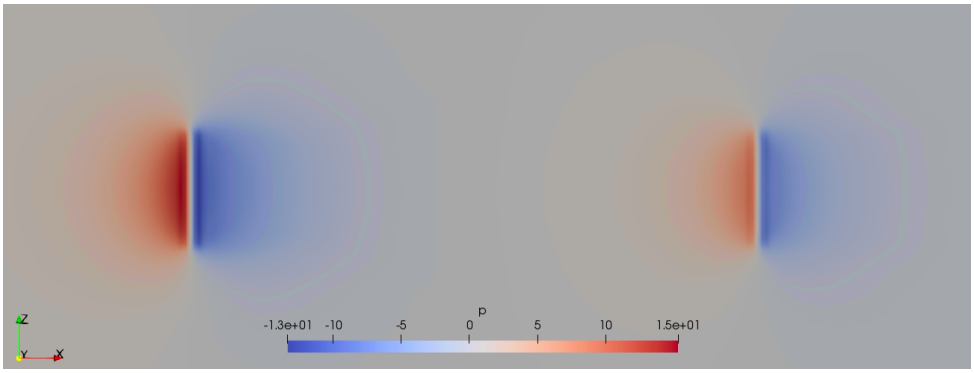

The pressure in the fluid increases just before reaching the rotor, and as it passes through it, it undergoes a sharp drop which represents the extraction of energy from the fluid by the turbine. Analyzing the velocity curve, it can be seen that the fluid decelerates as it approaches the rotor and just downstream it has its minimum value, characterizing the wake region. Slowly, the wake dissipates and wind speed increases, but without reaching the initial level.

Due to this wind speed behaviour, selecting an upstream point for the reference velocity (U_∞) requires some attention. For the first turbine, it is interesting to use as a reference velocity the furthest upstream point, where the flow is less affected by its presence, close to the inlet. However, for the second turbine, downstream, it is more challenging to determine the far wind speed, as it is strongly disturbed by the turbine upstream. Thus, we chose the point of highest fluid velocity between the two turbines, which is the region that is the least affected by the presence of both. This distance may vary from case to case, but the simulations showed that it usually occurs about 1 diameter upstream the second turbine, as shown in Fig. 35 by the local maximum value of the yellow curve.

Figure 35 – Velocity field indicating the axial centre line in white (a) and the plot of velocity magnitude $[m/s]$ in yellow and normalized pressure $[m^2/s^2]$ in red at this line (b) for two IEA 15 MW in tandem configuration at rated wind speed.

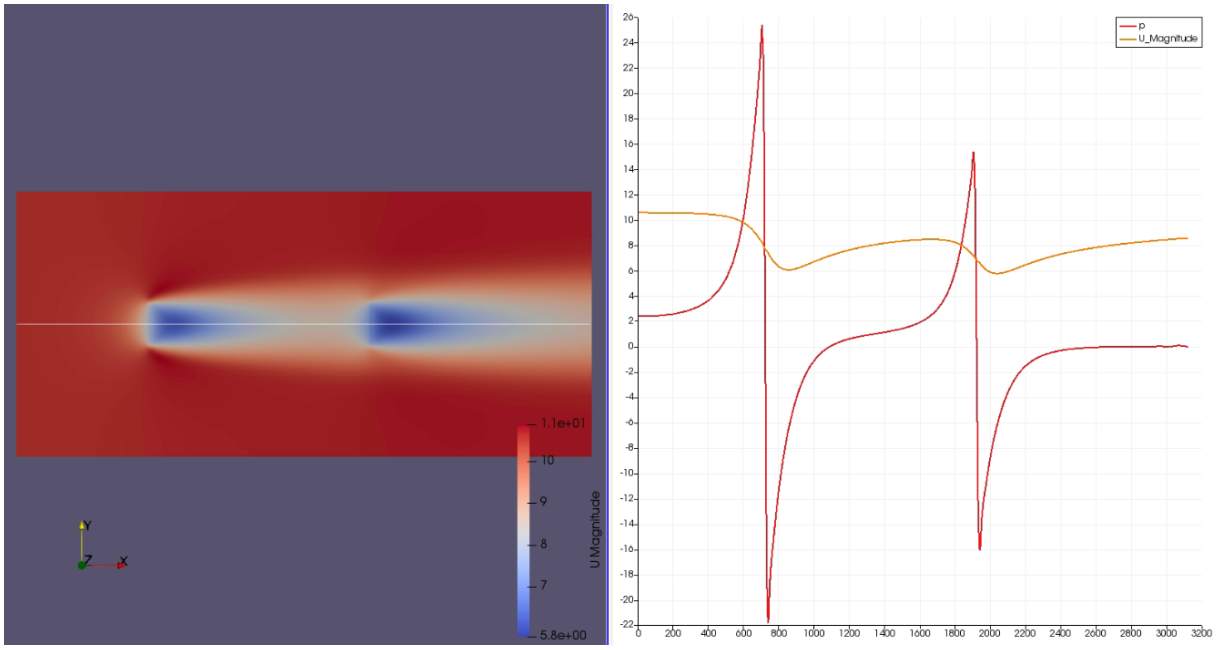

Table 1 – Turbulence variables at inlet for cases simulated with k-ε model with three different turbulence intensities: high (Fig. 36a), medium (Fig. 36b), and low (Fig. 36c).

Turb. Intensity	k (m^2/s^2)	ε (m^2/s^3)
High	3.8	5.0×10^{-3}
Medium	7.8×10^{-2}	7.7×10^{-6}
Low	3.8×10^{-5}	1.6×10^{-10}

4.2.2.3 Inlet turbulence properties in RANS

In the Reynolds Averaged Navier–Stokes (RANS) simulations, also called RAS in the OpenFOAM, the turbulence is modelled to solve the flow with reasonable computational cost. However, it is crucial to correctly define the inlet turbulence properties at the boundary domain, because the results can be highly affected by a small change on these parameters. Whether the turbulence is modelled by the k-ϵ, k-ω SST, or any other turbulence model, one should define the inlet turbulence parameters, such as k and ε for the k-ε model, or k and ω for the k-ω SST model.

Figure 36 presents the velocity field for three different inlet turbulence properties of the k-ε model summarized in Tab. 1. The high, medium, and low turbulence intensity values were tested for two IEA 15 MW in tandem configuration subjected to rated speed, uniform inflow (10.59 m/s).

By observing these figures, it is clear that the turbulence parameters on the inlet

Figure 36 – Velocity field around two IEA 15 MW in tandem with different k and ε at inlet as referred in table 1.

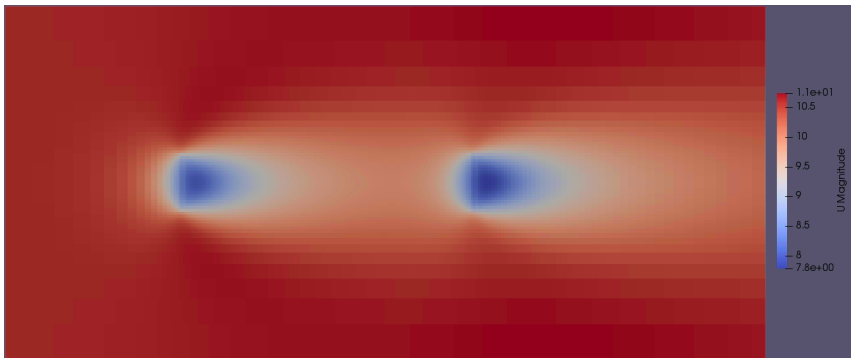

(a) High intensity.

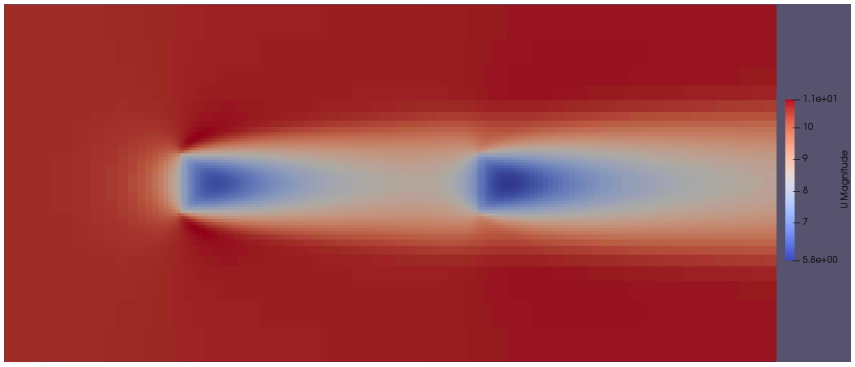

(b) Medium intensity.

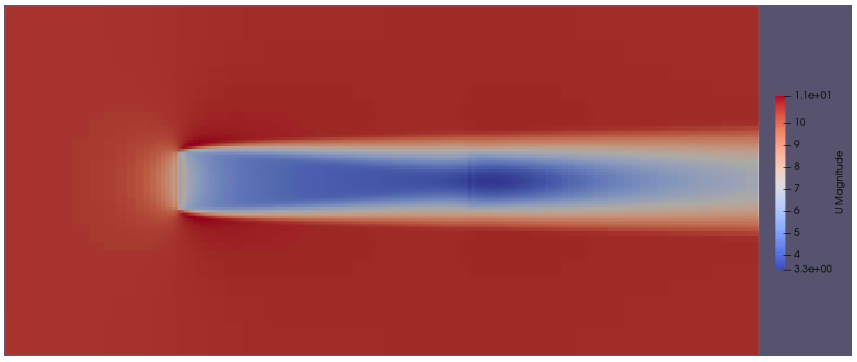

(c) Low intensity.

boundary have a huge impact on the simulation. Regarding the second turbine, downstream, its power generation will strongly decrease with lower k and ε values, because the flow velocity decreases in the wake. This occurs due to the characteristics of turbulence: the higher the kinetic energy (k) and dissipation (ε), the more perturbed will be the wake behind the first turbine, and the shorter its influence downstream.

As a result, in the simulation of the IEA 15 MW wind turbine submitted to the rated wind speed, the power generated by the first turbine is similar in the three cases and around 15 MW, but the power of the downstream turbine changes from 13 MW for the high k-ε values, to 8.3 MW for the medium values, and surprisingly 0.6 MW for the low values, representing almost a complete loss of power, what is not expected on a real scenario.

4.2.2.4 Turbine spacing

The next step was to simulate two turbines in tandem configuration, aligned with the inflow direction, varying the turbine spacing. Again, the results for the different turbines were essentially the same, so there is no need to show all of them, it suffices to present only the NREL 5 MW results for 8 m/s inflow speed. Nonetheless, the tandem configuration provides very different results according to the distance between turbines. So, turbine spacing was simulated for 5, 7.5, and 10 diameters, comprising the usual distances in real wind farm applications. Figure 37 shows the velocity field for these distances.

It is clear that the longer the distance between turbines, the less the effect of the wake on the downstream turbine. One can notice that the turbine placed 5 diameters downstream (Fig. 37a) encounters a flow field with less energy than that placed 10 diameters downstream (Fig. 37c). In terms of power production, the impact may be huge. For 5 diameters, the power of the downstream turbine is 0.95 MW, for $7.5D$ it is 1.24 MW, and for 10 diameters it is 1.41 MW, while the upstream turbine generates 1.86 MW for the three cases. This effect is also referred to as wake loss.

Therefore, by enlarging the turbine spacing, the wake loss drops, and the energy production increases, which is desirable. On the other hand, larger distances increase the capital cost due to longer array cables and larger array footprint. Some studies show that the optimum turbine spacing should be around $15D$ in fully developed wind farm boundary layers (Meyers; Meneveau, 2012), but in real applications, the distance usually remains about 6 to 8 diameters.

4.2.3 Rotor Disc Model

As pointed in section 2.5.1.3, the OpenFOAM *rotorDiskSource* class presents some physical inconsistencies for wind turbine modelling because it does not take into account the axial inflow wind velocity term. Despite that, results are presented to illustrate the

Figure 37 – Two NREL 5 MW aligned in tandem configuration for three different spacing distances: 5, 7.5 and 10 diameters. Note that total domain length increases with the spacing.

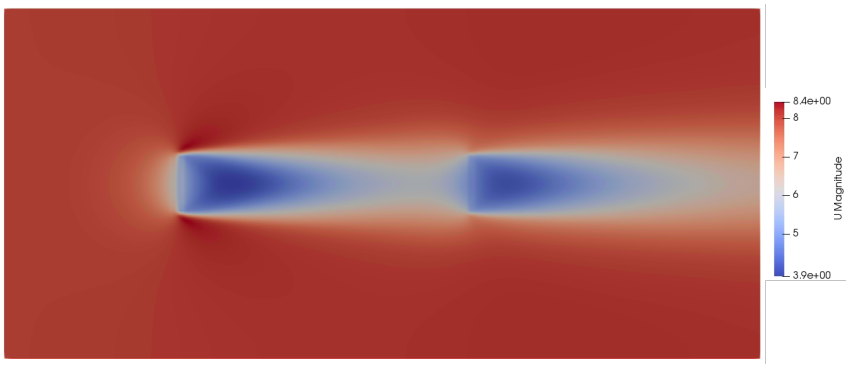

(a) 5D.

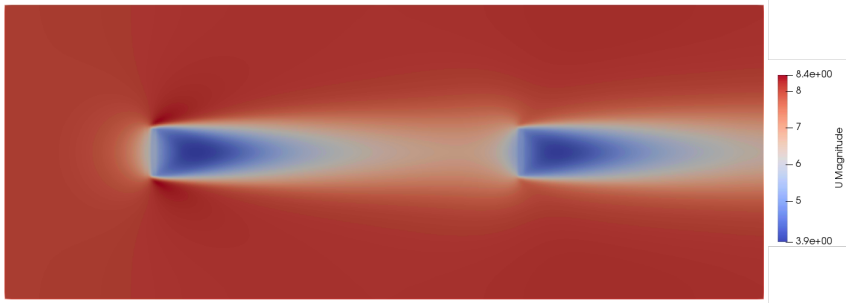

(b) 7.5D.

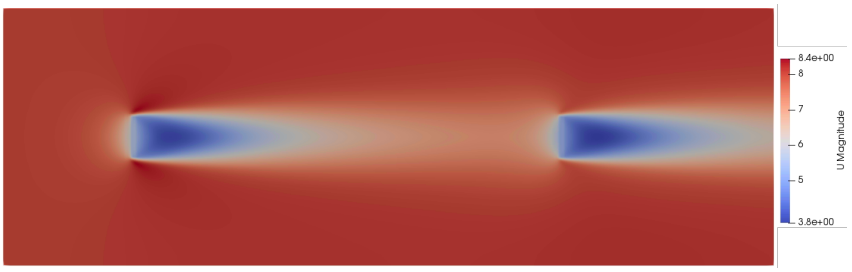

(c) 10D.

potential capabilities of this type of modelling. Figure 38 exhibits how the tangential forces on the disc results on a rotational flow in the wake region downstream the turbine. Additionally, Fig. 39 presents how the flow velocity changes radially according to the blade characteristics, in this case for the NREL 5 MW rotor without the hub.

Figure 38 – Isosurfaces of vorticity equals to 0.2 of the rotor disc model of NREL 5 MW.

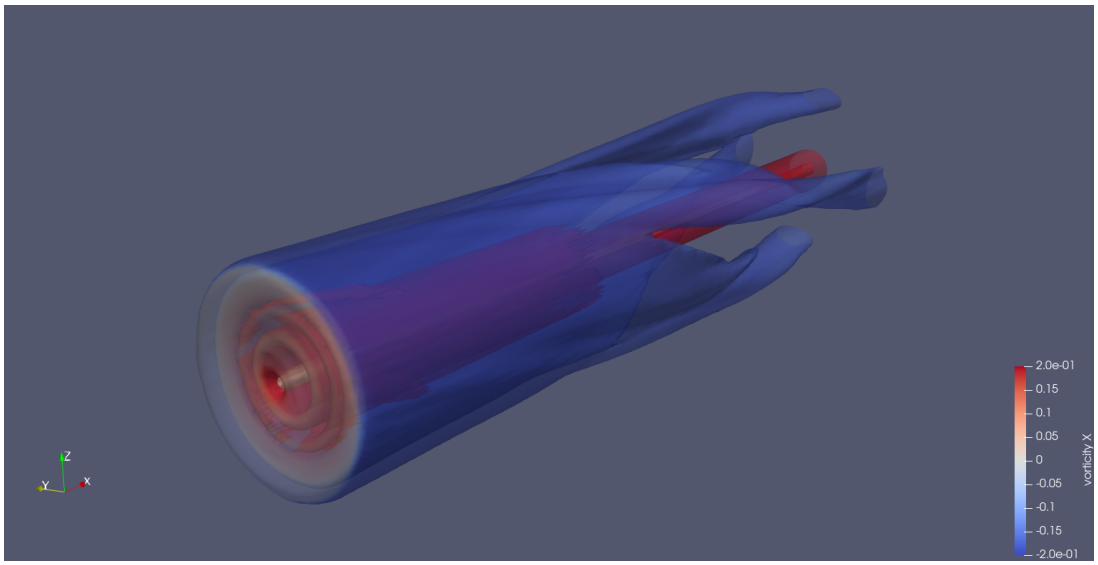

Figure 39 – Velocity field of the rotor disc model of NREL 5 MW.

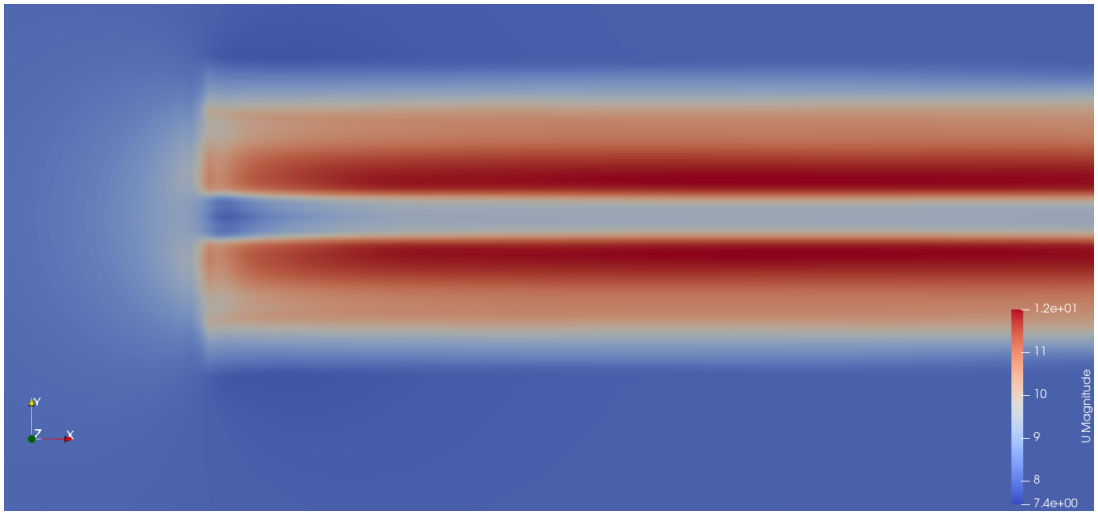

4.3 ACTUATOR LINE MODEL

A more refined model than the actuator disc is the actuator line (ALM). This section presents numerical results of this model using the LES Smagorinsky turbulence model. It begins with a verification of the *turbinesFoam* code, then, it presents a comparison of the results with the well established BEM model (Blade Element Momentum), as well as suggestions for the creation of the computational mesh and preliminary results of the tandem configuration.

The mesh used in this type of simulation is similar to that presented in the actuator disc section. One may notice that the mesh is not dynamic, so all the grid elements remain fixed during the simulation, just as it was for the actuator disc. The difference is that the actuator lines (or points) rotate, thus the points where the forces are applied on the flow (the blades) are constantly moving. This is the reason why it is possible to model the

Figure 40 – Iso-surfaces of vorticity equals to 0.25 for IEA 15 MW. Simulations carried out with actuator lines.

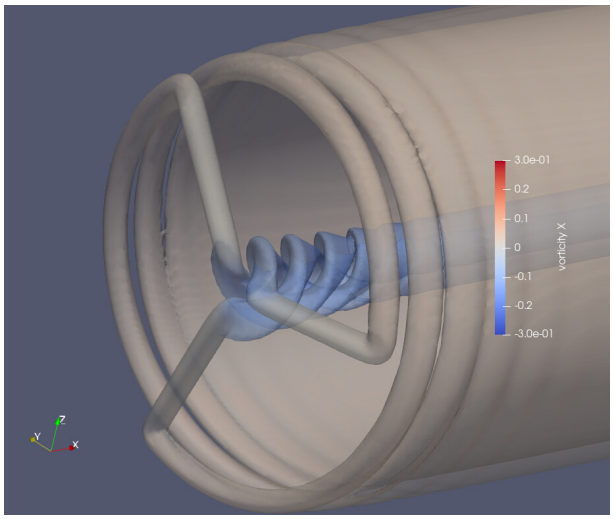

blade rotation and tip vortices without moving the mesh.

Figure 40 presents the iso-surfaces of vorticity for the IEA 15 MW rotor coloured by the vorticity in the x direction. The turbine is rotating clockwise for the reader, and each tip blade produces a helical vortex. This phenomenon, more commonly seen in ship propeller experiments underwater due to cavitation, is rarely seen in real wind turbines because of the transparent nature of the wind flow. Fortunately, this phenomenon was recorded under sun and rain concomitant conditions and presented previously in Fig. 9. Now the reader can visualize the same phenomenon occurring in a numerical simulation and a real life situation.

On the other hand, one thing that is not realistic is the root vortices seen in Fig. 40 in blue colors. Since the simulation does not model the hub, the root of the blade is expected to generate the same pattern as the tip, leading to root vortices. In real life turbines, there is no "edge" on the root because it is connected to the hub, but there is still a wake generated by the hub itself.

The tip vortices are also shown in Fig. 41a, which instead of presenting iso-surfaces of vorticity, presents the iso-surfaces of the Q parameter – the second invariant of the velocity gradient tensor – which filters part of the vorticity and usually results in more clear visualization of the turbulent flow structures. Figure 41b presents the same condition with the addition of the mesh discretization, so the reader can visualize it and note that the grid must be much more refined than the actuator disc (Fig. 31) in order to resolve the detailed structures of the tip vortices.

4.3.1 Code verification

In order to verify the correct computation and usage of *turbinesFoam*, it is useful to compare its results with another ALM tool. In this case, we used *WInc3D* (Deskos; Laizet;

Figure 41 – Iso-surfaces of Q parameter equals to 0.005 for IEA 15 MW, actuator line simulations.

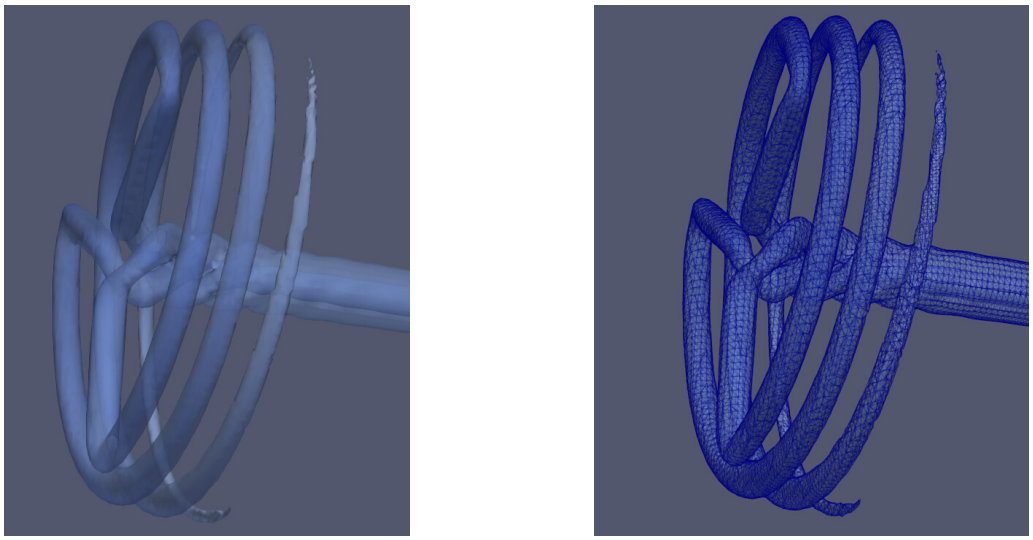

(a) (b)

Figure 42 – Comparison of forces along the turbine blade for two ALM codes with a coarse mesh.

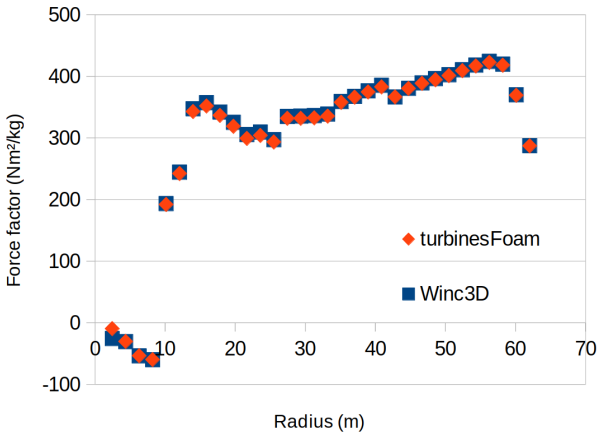

(a) Axial force factor

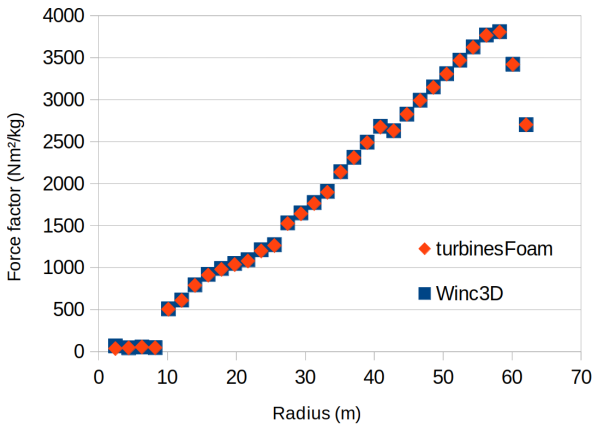

(b) Tangential force factor

Palacios, 2020), a wind farm simulation code built upon the high–order finite difference numerical solver *Incompact3D* (Laizet; Lamballais, 2009), developed by the researchers from Imperial College London. The simulations with *WInc3D* were carried out by Dr. Lucas Franceschini.

In this verification, forces along the blade are compared on the axial (Fig. 42a) and tangential (Fig. 42b) directions for the NREL 5 MW turbine on a coarse mesh. Both codes compute the forces normalized by the fluid density ρ, thus this force factor is the force divided by density which has the unit $\mathrm{N} \cdot \mathrm{m}^3/\mathrm{kg}$. In Fig. 42, the factor is shown per unit length and the radius position along the blade.

The results show a very good agreement for all actuator points, except the one at the blade root, which was found to be wrong in this Winc3D specific simulation. Hence,

the *turbinesFoam* code was verified and its usage understood. One important remark of this code is that in the input of the blade characteristics, the twist angle should be mainly negative, which is the opposite of the NREL 5 MW blade characteristics provided in Jonkman et al. (2009). In other words, one should multiply NREL's values of twist angle by (-1).

4.3.2 Comparison with BEM

One way of verifying the ALM simulation is to compare its results with a well established model that has already been validated with experimental data. Hence, this section presents a comparison between ALM and BEM results for the well known NREL 5 MW wind turbine rotor. The actuator line model was simulated with *turbinesFoam* and the BEM results were calculated with OpenFAST. It is important to mention that none of the calculations reported in this subsection considered tip correction factors for comparison purposes.

The primary variables that one should look at when analyzing a wind turbine simulation are the integral power and thrust coefficients,C_P and C_T respectively. Then, a finer way to compare two simulations is to analyze the loads along the blade, more specifically the axial and tangential forces with respect to the rotor plane. Later, for a more profound look, one can analyze C_D and C_L computed for the local airfoil sections, and look for its variables of influence such as flow relative velocity at a specific blade location, angle of attack, and Reynolds number.

Figures 45 and 46 compare the BEM results with different mesh refinements of the CFD code using ALM. The most coarse mesh is represented by the ALM-A case and the most refined one by the ALM-F case. The ALM cases from A to F were conducted with homogeneous mesh, and a finer case, ALM-G, was conducted with non-homogeneous mesh to save computational time. Also, an extrapolation for C_P and C_T was made to obtain a grid independent solution using the Richardson extrapolation (Richardson, 1910).

A summary of the cases is presented in Tab. 2. The first column is the case name, followed by the number of cells in millions, the grid size normalized by the rotor diameter Δ_g/D in percentage, the power coefficient C_P and thrust coefficient C_T, and the relative error compared to the BEM reference result.

The results from Figures 45 and 46, and Tab. 2 were submitted in the Wind Energy scientific journal with the collaboration of researchers from the University of Twente and the High-Performance Computing Center Stuttgart (HLRS). In the paper (Liu et al., 2022), it was shown that other ALM codes (WInc3D and UTwente-LES) provided the same results presented here, and some guidelines for ALM modelling were further discussed. It was found that the accuracy mainly depends on the grid spacing, and the actuator points should be spaced about three times the grid size.

In Fig. 43, the variation of the power and thrust coefficients is graphically presented,

Table 2 – Summary of different mesh refinements and Richardson extrapolation results of power and thrust coefficients compared with BEM. Number of cells and grid size Δ_g indicated.

Case	No. of cells (10^6)	Δ_g/D (%)	C_P (-)	C_T (-)	C_P err (%)	C_T err (%)
A	1.18	6.25	0.6350	0.8765	19.7	8.62
B	3.98	4.17	0.6019	0.8574	13.45	6.24
C	9.44	3.13	0.5870	0.8502	10.64	5.36
D	31.9	2.08	0.5722	0.8423	7.86	4.38
E	75.5	1.56	0.5623	0.8351	6.00	3.48
F	255	1.04	0.5524	0.8277	4.12	2.57
G*	5.82	0.78	0.5462	0.8224	2.97	1.91
Rich. Ext.	-	-	0.5293	0.8091	0.23	0.26
BEM	-	-	0.5305	0.8070	0	0

*Non homogeneous mesh.

Figure 43 – Power and thrust coefficients of NREL 5 MW for different mesh refinements using ALM.

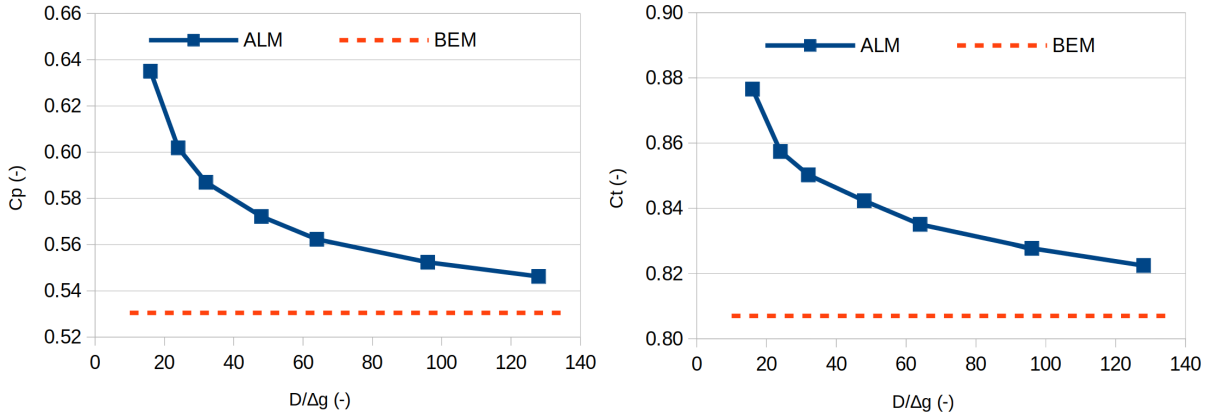

(a) Power coefficient

(b) Thrust coefficient

according to the refinement of the mesh. Full convergence was not achieved due to computational cost limitations. However, there is a clear tendency to converge to the BEM result, and for a discretization with more than 120 elements per turbine diameter, the error is less than 3%.

Previous works (Martínez-Tossas; Churchfield; Leonardi, 2015) had shown that the mesh refinement would increase the power prediction. However, the apparent difference is because they fixed ϵ at a specific length in meters, and we fixed it with respect to the grid size ($\epsilon = 2.5\Delta_g$).

If we want to extrapolate the numerical results to what would represent an infinite number of cells in the mesh, we can use the Richardson extrapolation. Figure 44 graphically shows this extrapolation (red dot), and the excellent agreement (difference $< 0.3\%$) with the BEM result (red dashed line).

After analyzing the integral power and thrust coefficients, it is interesting to evaluate

Figure 44 – Richardson extrapolation of coefficients of NREL 5 MW of ALM compared to BEM results.

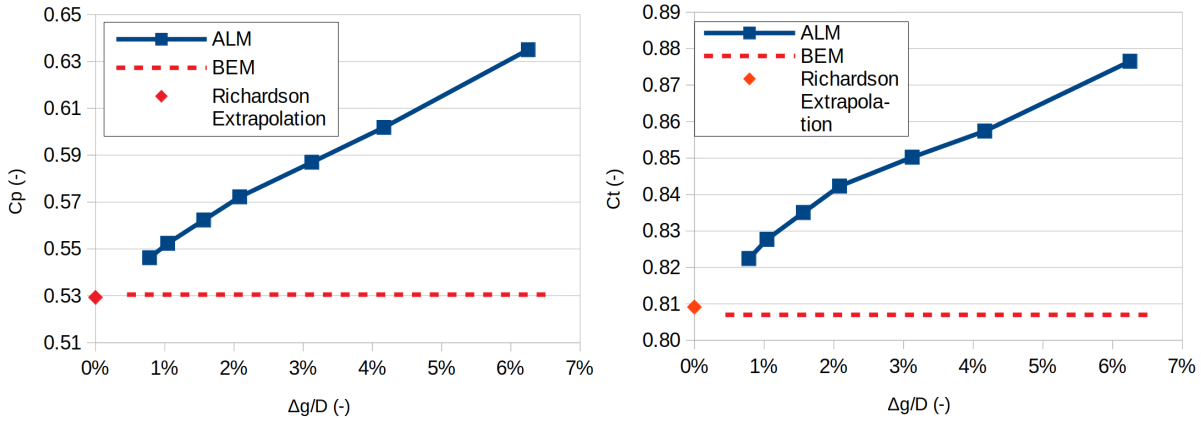

(a) Power coefficient

(b) Thrust coefficient

Figure 45 – Tangential forces along NREL 5 MW blade.

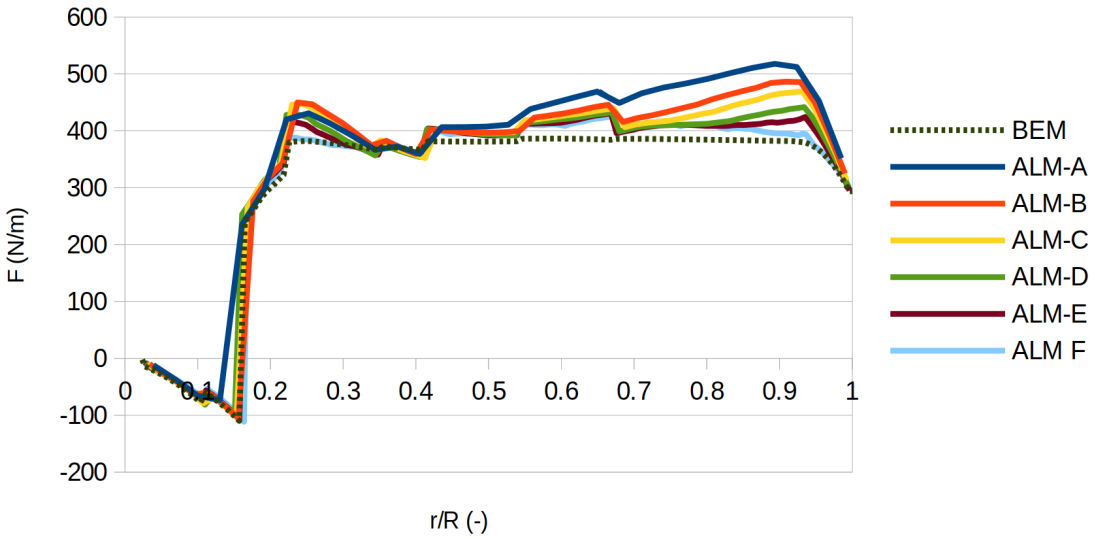

the forces acting along the turbine blades, and how they behave when refining the mesh. Figures 45 and 46 show the tangent and axial forces respectively. The most abrupt changes in the force profile are mainly due to the change of blade airfoil. Note that axial loads are one order of magnitude greater than tangential ones, the latter being responsible for the generation of torque and, consequently, power and electrical energy.

It can be noticed that in simulations with coarser meshes the forces are overestimated, but even in the most refined case, some differences persist. Therefore, a more in-depth investigation was carried out on the variables that originate such forces, notably the airfoil lift and drag coefficients and the angle of attack of the flow at the blade actuator points.

Figure 47a presents the drag coefficient C_D along the entire blade of the NREL 5 MW comparing the Actuator Line Model (ALM-E) and the BEM. Figure 47b zoom in the region from 20% to the tip of the blade, so the reader can have a better visualization. The

Figure 46 – Axial forces along NREL 5 MW blade.

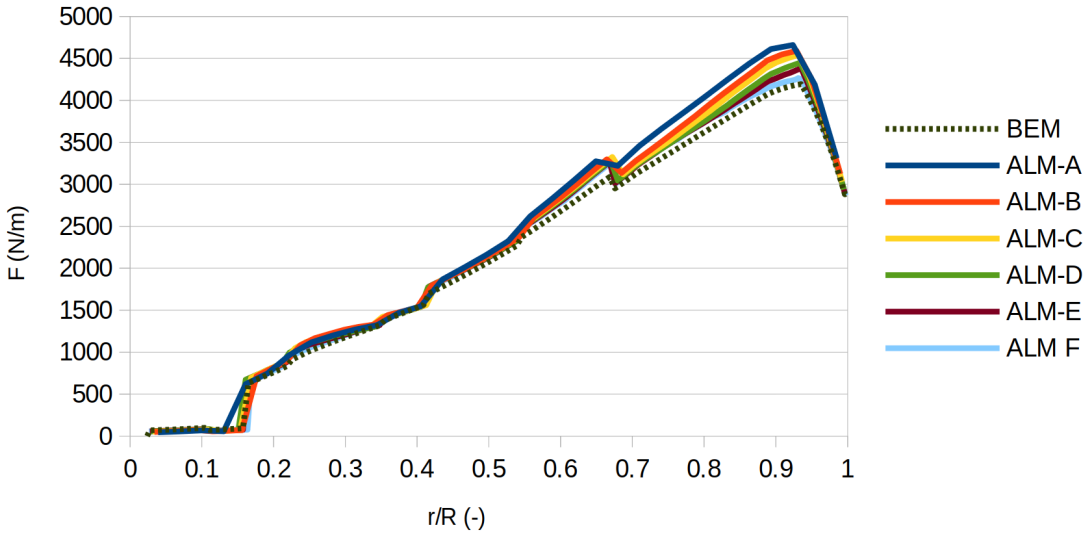

Figure 47 – Comparison between BEM and ALM results for airfoil drag coefficients along the NREL 5 MW blade.

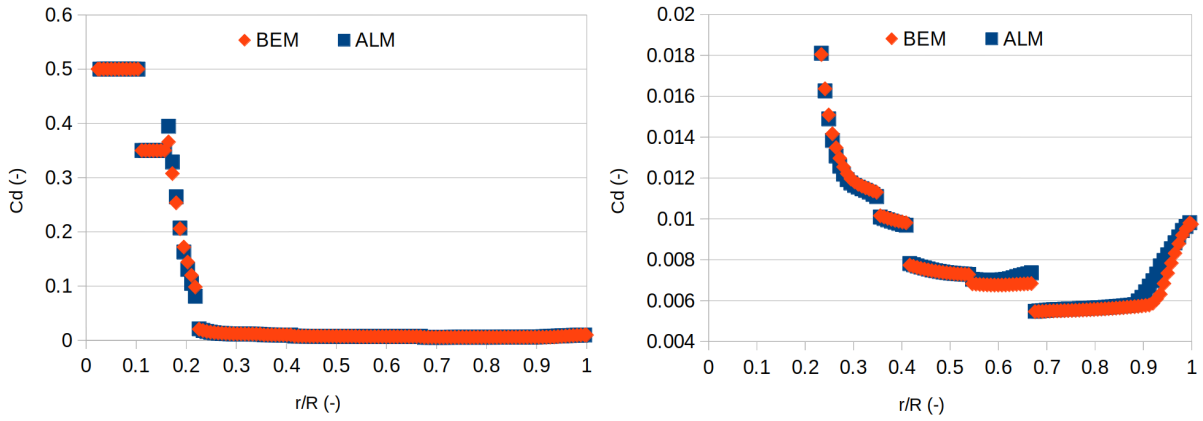

(a) Entire blade.

(b) Zoom.

differences are small for most of the blade, with slightly mismatched values near the tip of the blade, but with little influence on the forces as the absolute values of C_D are very small (less than 0.01 for most of the blade). This is expected in airfoils since they are designed to perform under high lift and low drag regimes. The exception near the root, where the C_D is 0.5, occurs because the blade profile in this region is a circle for structural purposes.

Regarding the lift coefficient C_L, the absolute values are much higher than those for C_D as shown in Fig. 48a for the entire blade. By zooming the graph to better visualize the results in the range from $r/R = 0.3$ to the tip (Fig. 48b), one may note differences up to 5% between the ALM and BEM in some regions, such as in 60% of the blade. Obviously, these differences will alter the resulting forces and hence power and thrust. Moreover, since the relative wind speed near the tip is higher, a slight change in the coefficient may imply important differences in force, and concerning the torque, these forces will effectively impact the computed power. This can be verified in Tab. 2, in which the power coefficient

Figure 48 – Comparison between BEM and ALM results for airfoil lift coefficients along the NREL 5 MW blade.

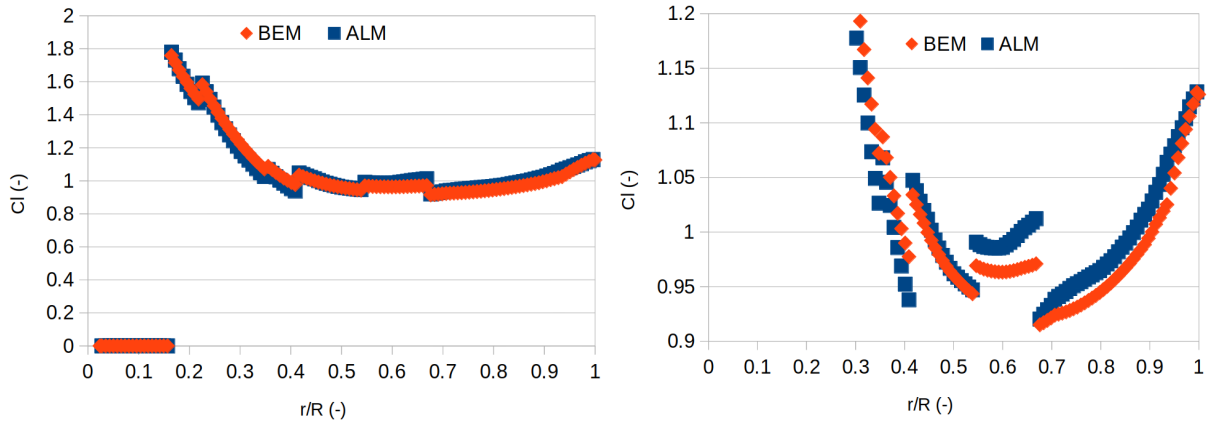

(a) Entire blade.

(b) Zoom.

usually has a larger error compared to thrust. This can certainly be improved with the use of tip correction factors.

The lift and drag coefficients of an aerofoil depend on its geometry, flow speed, and angle of attack. For a given aerofoil geometry, the angle of attack has a bigger influence on the coefficients, so usually, the aerodynamic coefficients are given for a specific Reynolds regime. *turbinesFoam* can compute the coefficients based on variable Reynolds number, but this option was not used in this work. Hence, the coefficients of each airfoil depend essentially on the angle of attack and this variable must be analyzed in order to understand the different results between ALM and BEM.

Again, the values are shown all along the blade in Fig. 49a and zoomed in for easy viewing in Fig. 49b. These results are very interesting because, unlike those previously presented, there is a structural difference between one model and another. In the case of BEM, the points present discontinuities where there is a change in the airfoil profile, whereas in the case of the Actuator Line (ALM) the points form a continuous curve. Here is an intrinsic difference of the models that would explain minor differences between them regardless the mesh refinement. BEM treats the flow radially independently, while the ALM model, which uses CFD, is governed by the Navier-Stokes equations and, therefore, the entire flow is coupled, avoiding discontinuities.

4.3.3 Homogeneous and Non-Homogeneous Mesh

A mesh grid is denominated homogeneous if all the cells have the same size. It can be useful for increasing computational performance in specifically designed codes, or to simulate small turbulence scales in the whole domain in DNS simulations for example. However, CFD simulations are usually performed under non-homogeneous mesh, in which cell size varies according to the flow characteristics. Generally, regions with strong gradients

Figure 49 – Comparison between BEM and ALM results for the angle of attack (AoA) along the NREL 5 MW blade.

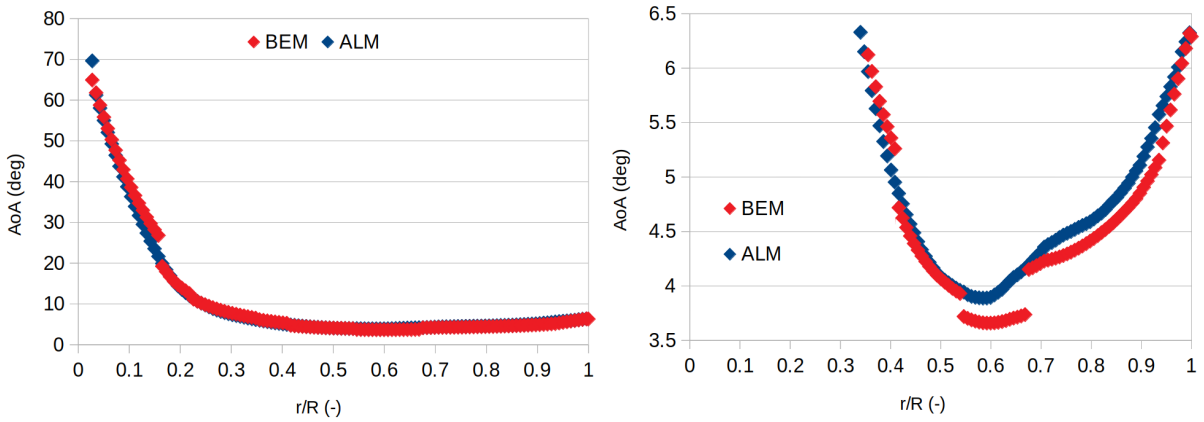

(a) Entire blade.

(b) Zoom.

should be well refined, while regions far from the interest subject can be less refined to save computational cost.

In this context, it is important to know how the cell size far from the rotor could impact the rotor performance. For this purpose, a comparison between homogeneous and non-homogeneous mesh was conducted, both having the same cell size at the rotor disc, but the latter presenting less refinement far from the disc.

Fig. 50 shows two meshes with the same refinement in the rotor region, but the one on the left is homogeneous and the one on the right has coarser elements away from the rotor. They represent the refinement of the ALM-B case, and have 3.98 mi elements for the homogeneous case and 0.27 mi for the non-homogeneous case. For the ALM-F case, the homogeneous mesh with 255 mi elements was simulated making parallel use of 1056 processors and simulated 1 physical second in 20 minutes of CPU. Its non-homogeneous analogue case had a mesh of 3.25 mi elements and with 24 processors simulated 1 physical second in 5 minutes of CPU. This means a speed-up of around 176 times. Most importantly, in terms of results, both had practically equal integral coefficients (differences less than 0.05%). Therefore, it can be stated that the mesh in the far field can be coarser than close to the rotor to save computational cost and maintain the result accuracy. Thus, what would be the case ALM-G, with 604 mi elements and mesh size 0.78% of the rotor was simulated only in non-homogeneous mesh with 5.82 mi elements and the results included in the graphs of Figures 43 and 44 and the Tab. 2.

4.3.4 Tandem Configuration

When two rotors are placed in tandem configuration under uniform inflow an interesting phenomenon is observed. Since the inflow has no significant perturbations or turbulence, the wake of the first turbine is stable for a long period. However, as the flow

Figure 50 – Comparison between homogeneous (a) and non-homogeneous (b) meshes with the same cell size at rotor disc.

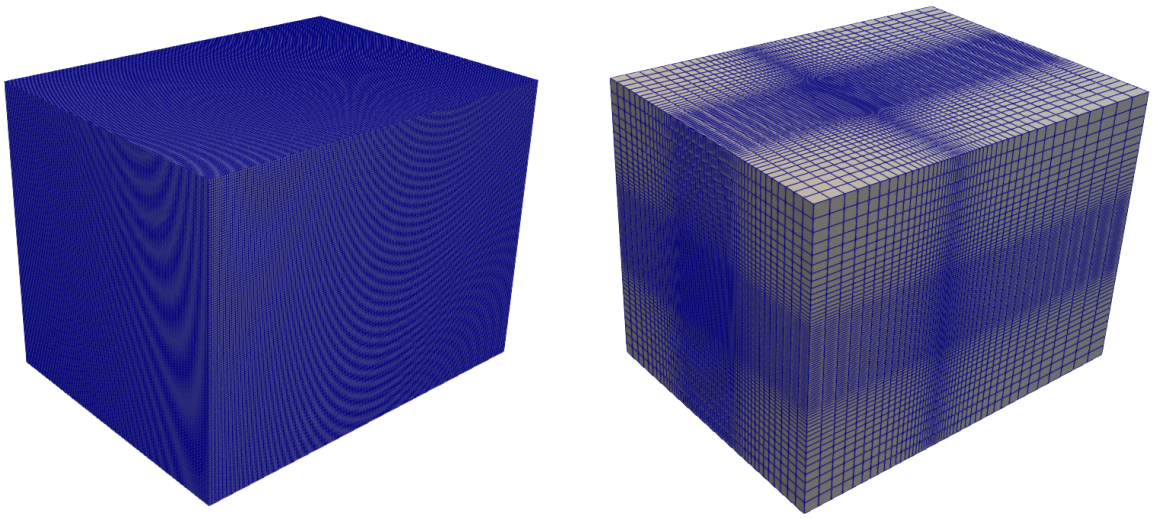

(a) Homogeneous mesh.

(b) Non-homogeneous mesh.

Figure 51 – Iso-surface of vorticity for two IEA 15 MW in tandem.

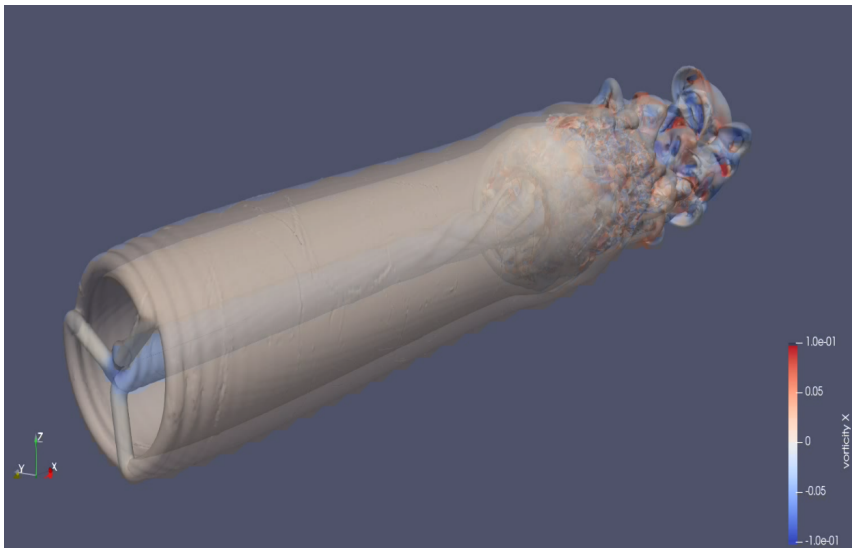

that reaches the second turbine is strongly perturbed, the second wake is rapidly unstable and generates a complete turbulent flow. This behaviour can be observed in Fig. 51, which presents the iso-surfaces of vorticity, and Fig. 52, which is a cut plane of the same variable.

As a consequence of the stable wake, the power production of the downstream turbine is highly affected. Preliminary simulations have shown a power production 10 times smaller in the downstream turbine compared to the upstream one. Regarding the thrust, the force is 2 times smaller.

In real life, there is always an atmospheric boundary layer (ABL) developed by the presence of the ground. For this reason, a simulation with a no-slip bottom boundary was performed to analyse the wake behaviour (Fig. 53). As expected, the presence of the

Figure 52 – Vorticity cut plane for two IEA 15 MW in tandem.

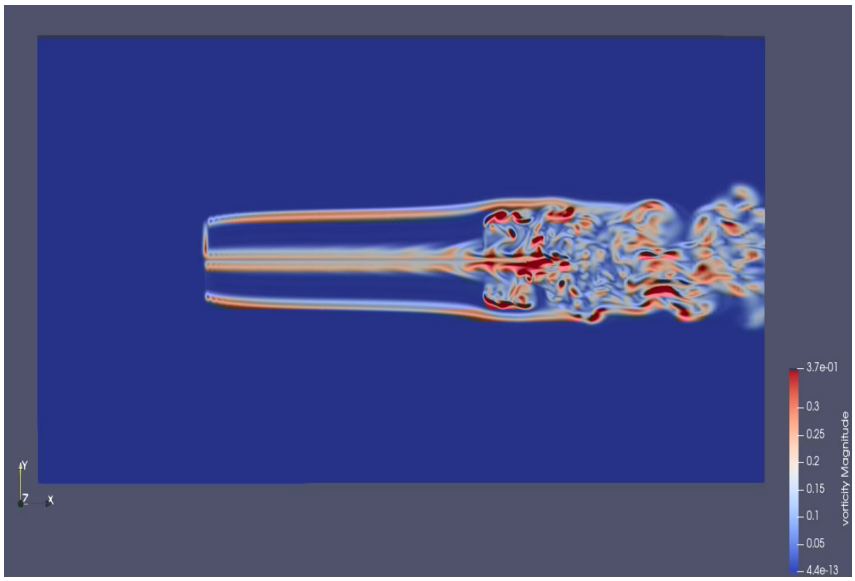

Figure 53 – Iso-surfaces of vorticity 0.25 coloured by X vorticity for the IEA 15 MW with no-slip ground.

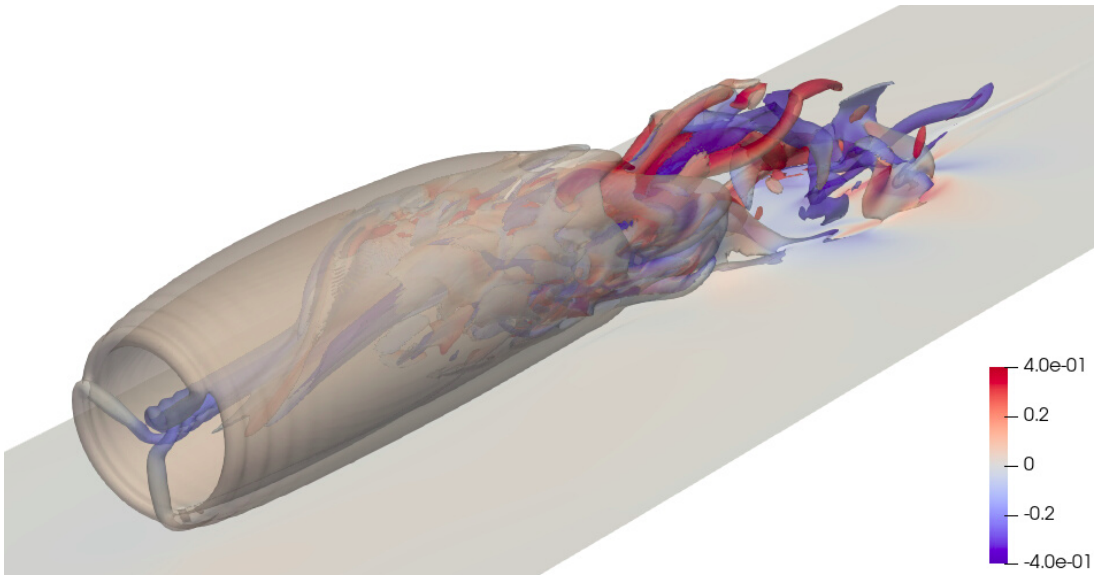

atmospheric shear layer induces fluctuations in the flow that lead to a turbulent wake.

The next steps to model a more realistic situation should be the addition of the hub and tower, turbulence on the inflow, a control system to regulate the turbine, and ABL stability condition due to vertical temperature gradient.

4.3.5 Turbulent Inlet

Typically, laminar flow does not represent a real situation when dealing with large wind flow scales. Thus, to set up a more realistic simulation, it is mandatory to consider a turbulent flow at the inlet of the computational domain.

In RANS simulations, the introduction of turbulence is quite straightforward as

already seen in the actuator disk chapter. The turbulence quantities are modelled with variables such as turbulent kinetic energy k and dissipation ϵ, which represent averaged dynamics. So, one can easily adjust the turbulence intensity at the inlet by tuning these parameters in the boundary conditions. However, in LES simulations, the turbulence is not modelled, instead, it is computationally resolved for scales larger than the cell size. Therefore, in LES simulations the turbulence only exists if there are oscillations in the velocity and pressure field.

There are basically two approaches for introducing turbulence at the inlet of LES simulations. One is to develop turbulence in a precursor simulation, and the other is to use a synthetic turbulence generator at the inlet boundary condition.

The first method consists of running a previous simulation without the turbine for a long period of time until the turbulent structures develop and achieve a converged condition. Usually, periodic boundary conditions are set at the inlet/outlet, as an infinity channel flow. Afterwards, the outlet variables are used at the inlet of the main simulation, with the turbine. Therefore, one must record all the variables for all time steps, which is very expensive in terms of computational space memory, or run both simulations coupled, which is expensive in terms or processing time.

The other method assumes that turbulence can be generated synthetically by a mathematical model, that is a boundary condition. In current OpenFOAM versions, there are two velocity boundary conditions for synthetic turbulence generation, the *turbulentDigitalFilterInlet* and the *Divergence-Free Synthetic Eddy Method* (DF-SEM). The first model includes synthesised eddies by a divergence-free turbulence field that can reproduce almost all possible states of Reynolds stress anisotropy (Poletto; Craft; Revell, 2013). The second method generates synthetic turbulence-alike time-series by random number set (mostly white noise), and a group of target flow statistics, and it is described in detail by Klein, Sadiki and Janicka (2003).

4.3.5.1 Precursor simulation

An atmospheric boundary layer (ABL) was modelled using the precursor simulation technique. We tried to reproduce real averaged measured data at a pier on the Brazilian south coast (Nassif et al., 2020). Figure 54 presents the mesh and the flow field after the development of turbulent structures. A periodic condition was defined at the inlet and outlet boundaries, to model an “infinity channel flow”, and at the lateral boundaries the same boundary condition was applied to allow cross sectional flow. The upper boundary was set as symmetry and the bottom as the no-slip condition. There are a few parameters to control the ABL shape. The mean velocity is generated by a pressure gradient and the shear by the modelled roughness at the bottom boundary.

The results presented in Fig. 55 show that the numerical setup was unable to accurately reproduce the same flow dynamics. With a converged setup in time and space,

Figure 54 – Mesh and velocity field of a turbulent flow produced by a precursor simulation.

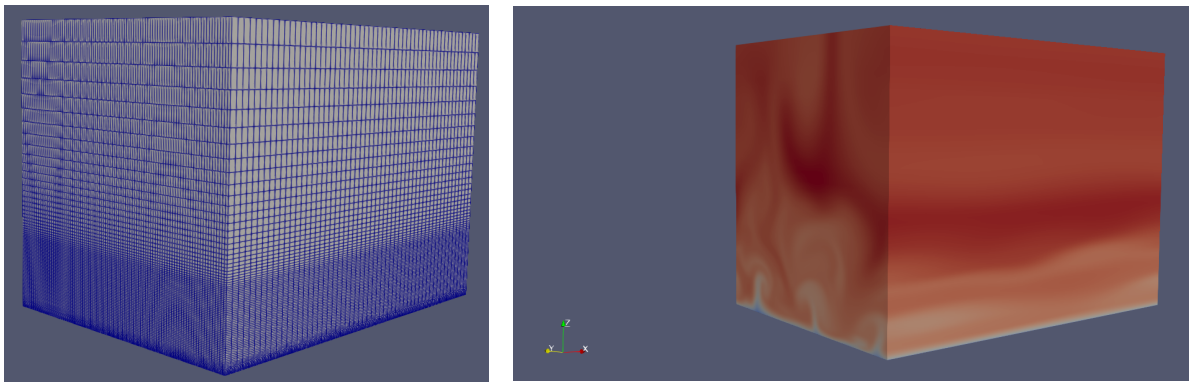

(a) (b)

Figure 55 – Mean profiles of velocity and turbulent intensity in a precursor simulation compared to real LIDAR data in a pier.

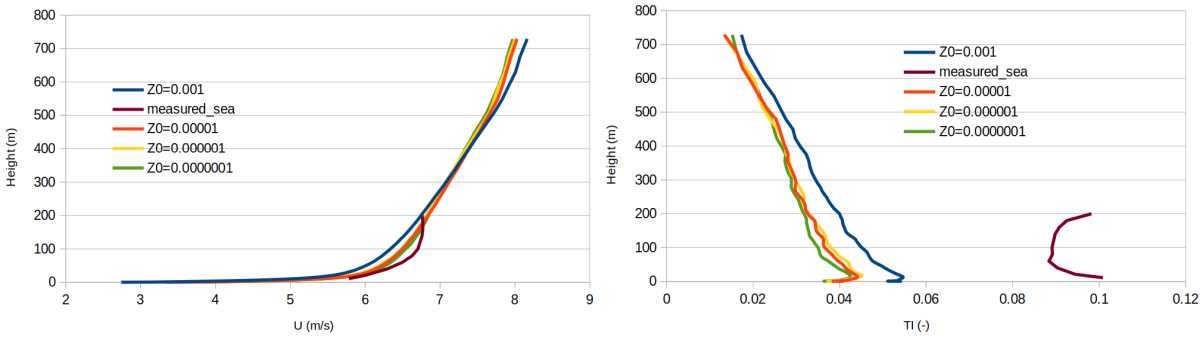

(a) Wind velocity mean profile in a precursor simulation.

(b) Turbulent intensity mean profile in a precursor simulation.

the increase of roughness at the bottom generates a turbulence intensity profile closer to the measured values, while the wind shear profile gets further away from it, thus, it was not possible to reproduce both curves. Moreover, the turbulence profile has a different shape than that produced by the simulation. Some explanations for these differences are the influence of coastal breezes that were not considered in the model, and that the real data is an averaged data of several months. Besides, our model does not include thermal effects, which usually plays a crucial role in the production of turbulence in atmospheric flows.

This result is useful to understand the limitations of a precursor simulation beyond the computational costs. A huge drawback of this modelling is the impossibility of adjusting parameters to have the desired flow configuration. Aiming for a more flexible tool, we chose a synthetic turbulence generator for the following results.

Figure 56 – Mesh and velocity field of a turbulent flow produced by the synthetic turbulence generator model DF-SEM.

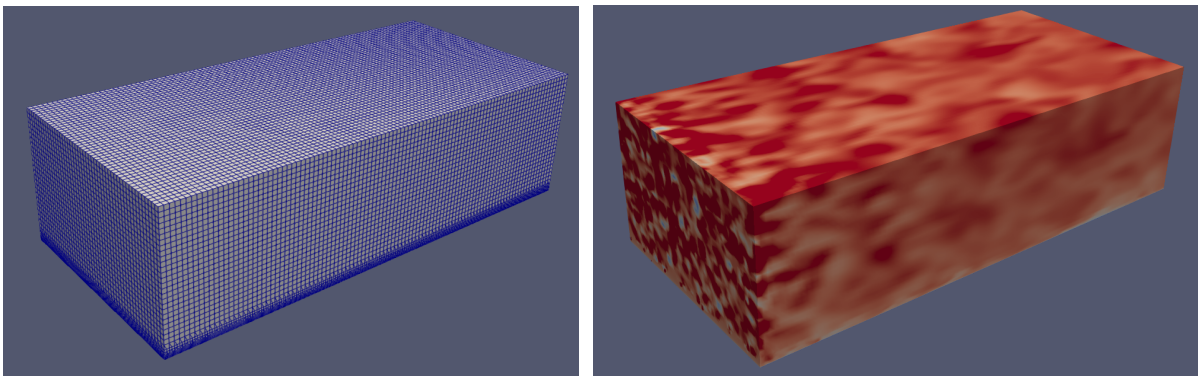

(a) (b)

4.3.5.2 Synthetic Turbulence

The present work used the OpenFOAM model DF-SEM for generating synthetic eddies at the inlet boundary. Mainly, three variables must be defined: the mean velocity U_{mean}, the turbulent length scale L, and the Reynolds Stress Tensor R. The mean velocity was defined by a log law profile with 8 m/s at the hub height, the turbulent length scale was set to be half of the rotor radius, i.e. 60 m, and the diagonal of the Reynolds Stress Tensor was computed using 10% of turbulence intensity. Figure 56 presents the flow field produced by the synthetic turbulence model.

The difference between the turbulent flow produced by the precursor simulation and the synthetic generator can be observed in Figures 54b and 56b. The turbulence in the last was intentionally set to be higher and close to measurement data, while the turbulence in the first is smaller and produced by the bottom boundary only. The better control of turbulent parameters and the flexibility to easily increase or decrease turbulence intensity is a great advantage of the synthesized turbulence model.

4.3.6 Final Results

The final results presented in this work refer to the actuator line model (ALM) with large eddy simulation (LES) and synthetic turbulence at the inflow. Two offshore IEA 15 MW wind turbines in tandem configuration were simulated for different spacing distances: $5D$, $7.5D$, and $10D$.

Regarding the mesh, the whole domain is divided into cubes of 30 m, which is 12.5% of the rotor diameter. At the wake region, each cube is divided 2 times in each direction, so the cell size is 7.5 m (3.13% of D), and at the bottom, there are 3 levels of refinement, so it is 3.75 m (1.56% of D). Finally, at the rotor region, the cell is refined one more time, so the size is 1.875 m (0.78% of D), which is refined enough to correctly compute power and thrust coefficients as presented in Section 4.3.2.

Figure 57 – Mesh for two IEA 15 MW in tandem configuration spaced by $5D$.

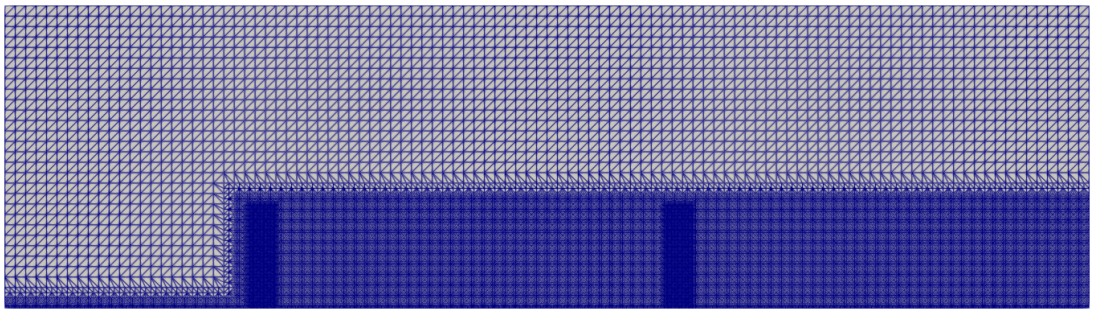

Figure 58 – Closer look at turbine level mesh.

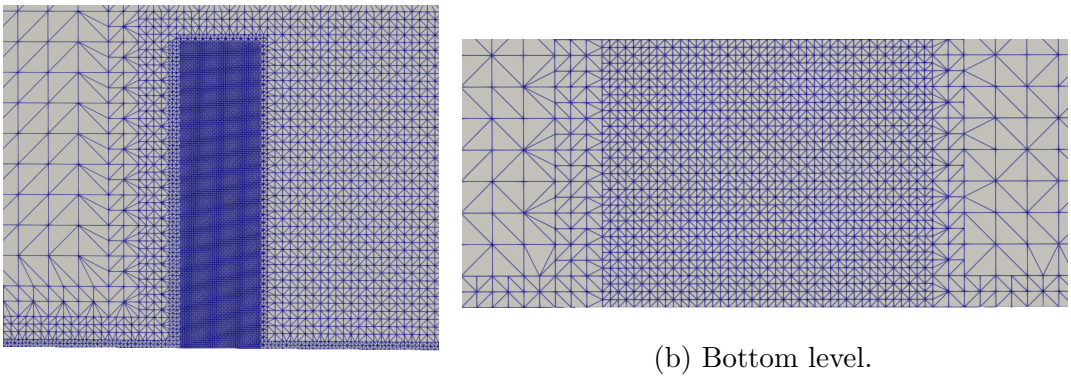

(a) Turbine level.

(b) Bottom level.

The mesh used for $5D$ of turbine spacing is presented in Fig. 57, and a closer view at the turbine level is shown in Fig. 58.

The mean wind speed at hub height (150 m) is 8 m/s and the rotation is fixed at $TSR = 9$. The turbulent parameters were set so the flow reached the first turbine with a turbulent intensity of around 10% as measured in real situation by the LIDAR case presented in the last section. Firstly, only the blades were modelled, with no tower or hub.

The instantaneous wind speed magnitude is presented in Fig 59 for two IEA 15 MW in tandem configuration spaced by 5 diameters. The turbulent structures observed on the left side of the figure are generated at the inlet by the synthetic turbulent boundary condition. Downstream the first turbine, smaller turbulence structures are generated by the blades, and the low wind speeds colored in blue characterize the wake region. The flow reaches the downstream turbine and the wake develops into lower wind speeds. Also, the iso-contours of the Q parameter are plotted around the turbines and provide a good visualization of the tip vortices surrounding the rotor.

Although the instantaneous profile can provide interesting insights about the turbulence structures developed in the flow, the analysis of the averaged flow may give a better comprehension of the flow. In order to know the necessary time to average the flow, a probe measured the wind speed upstream of the first turbine, and three moving averages were calculated. The averaged wind speed for periods of 60 s, 600 s, and 1500 s are presented in Fig 60. It shows that 1-minute average is not sufficient to determine an

Figure 59 – Side view of the instantaneous wind speed around two IEA 15 MW in tandem configuration spaced by $5D$. Iso-surfaces of Q parameter equals to 0.05.

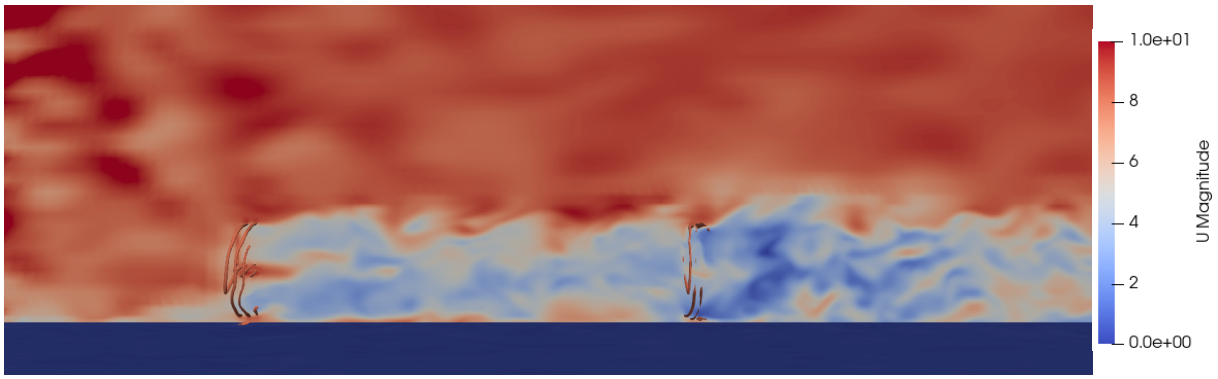

Figure 60 – Stream-wise wind speed along time and three moving averages.

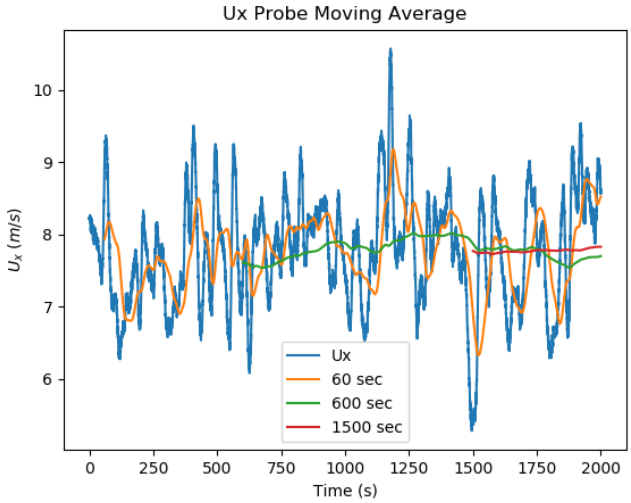

averaged wind speed, while 10 minutes provides a ruffly good average. Definitely, 1500 s is enough to average the flow oscillations.

Based on this result, the flow variables were averaged along the 1500 last simulation seconds, and the mean wind speed can be visualized in Fig. 61. The similarities between these results and those presented in Fig 37, for actuator disk models using RANS model, show that the last is a good approximation for the mean flow. The jet flow observed in the rotor center occurs due to the absence of a hub. It is also possible to visualize lower wind speed near the ground due to the sheared profile.

Figure 62 shows the mean pressure field, and again the result is similar to what was previously presented in Fig 34. We can see a high pressure zone upstream the rotor and a low pressure zone downstream, with a stronger pressure gradient at the first wind turbine. As in the velocity field, it is possible to observe the absence of a hub.

When the space between turbines increases, the flow characteristics are similar, but the wake has more time and space to recover. Figure 63 presents the top view of the instantaneous wind speed for rotors spaced by $10D$. It is clear that the lower wind speeds,

Figure 61 – Side view of the mean wind speed for two IEA 15 MW in tandem configuration spaced by $5D$. Iso-surfaces of Q parameter equals to 0.05.

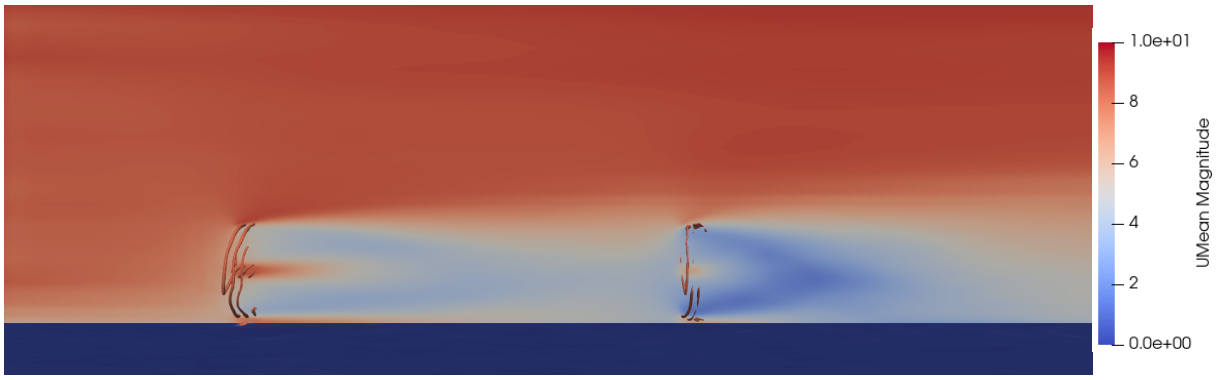

Figure 62 – Side view of the mean pressure field and two IEA 15 MW in tandem configuration spaced by $5D$.

Figure 63 – Top view of the instantaneous wind speed for two IEA 15 MW in tandem configuration spaced by $10D$.

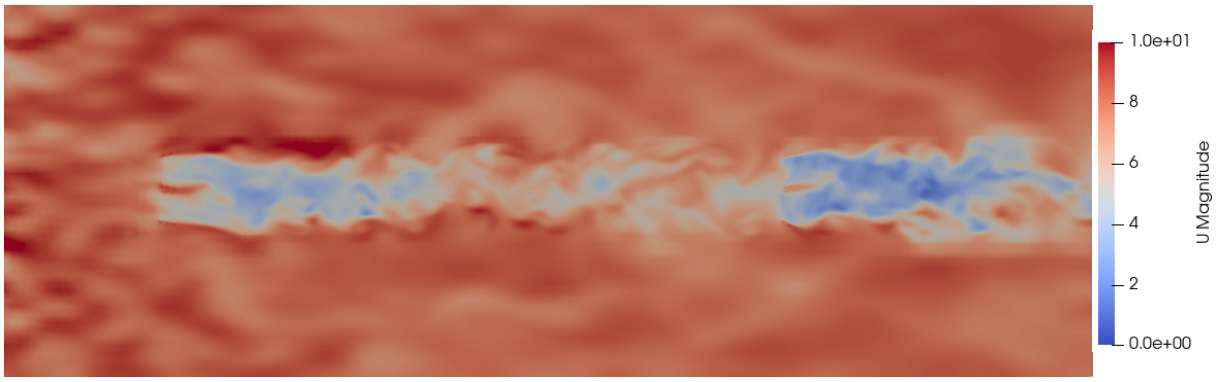

represented by blue colors dissipate more before the flow reaches the second wind turbine. The mean wind flow is presented in Fig 64. It is interesting to notice that the wake width does not vary significantly along the flow, and how much it grows will be graphically presented later in Fig. 67.

After the flow field visualizations of isolated cases, more details can be obtained by comparing multiple cases in graphics. The first comparison is the effect of the different turbine spacing in the vertical wind profile. Figure 65a compares the profiles at 1 diameter downstream the first turbine, and Fig 65b at 1 diameter downstream the second turbine.

Figure 64 – Top view of the mean wind speed for two IEA 15 MW in tandem configuration spaced by $10D$.

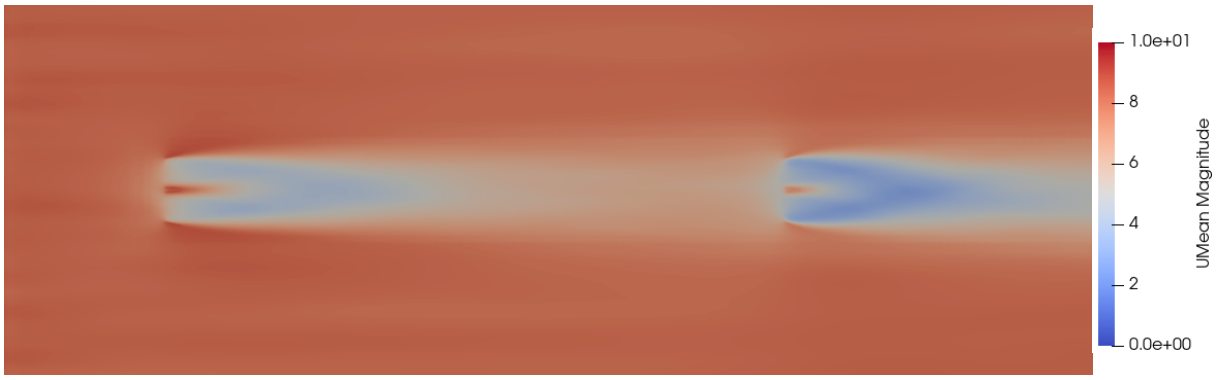

Figure 65 – Vertical wind profile for different turbine spacing at 1 diameter downstream the first turbine (a) and 1 diameter downstream the second turbine (b).

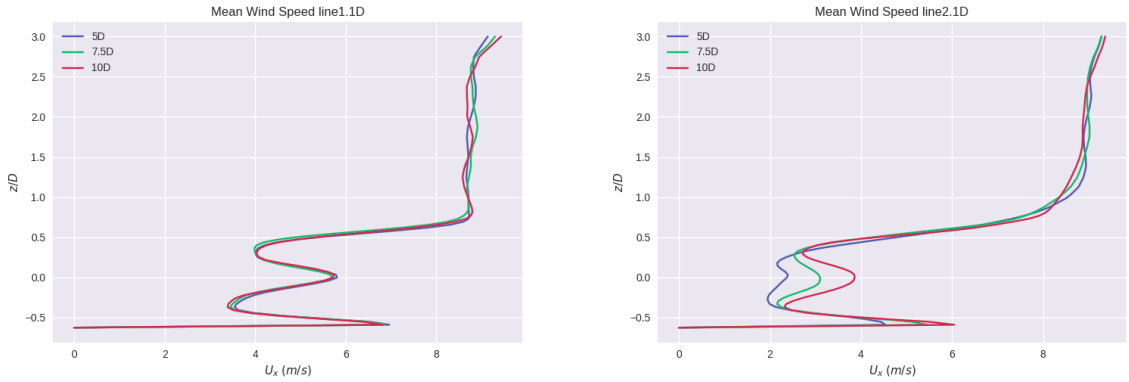

(a) (b)

As expected, for the three cases the vertical profile is the same at 1 diameter downstream the first turbine, there are no differences in the flow at this point because the effect of the second turbine there is negligible. However, for 1 diameter downstream the second turbine, important differences appear. The blue curve presents the flow velocity for the case in which the turbines are spaced by $5D$, thus it is at 6 diameters ($5D + 1D$) downstream the first turbine. The red curve presents the case of $10D$ spacing, so the curve is plotted at $11D$ downstream the first turbine. In the case of larger spacing, the wake recovery is higher because the wake has more time and space to dissipate. The $7.5D$ case is an intermediate position between the other ones. Downstream from the second turbine, the wind speed at the hub height for the $10D$ case is almost 2 times the wind speed for the $5D$ case in Fig. 65b, which in terms of power increase is very significant since it scales with the velocity to the third power. In a wind farm, where several rows are placed, this effect would be even more amplified. This is the reason why it is rare to place wind turbines less than $5D$ downstream.

Besides the vertical profile, it is also important to analyze how the flow changes in the stream-wise direction. For this purpose, the wind speed at a stream-wise line passing

Figure 66 – Stream-wise line passing at the center-line (a) and at $R/2$ above the center line (b) for different turbine spacing.

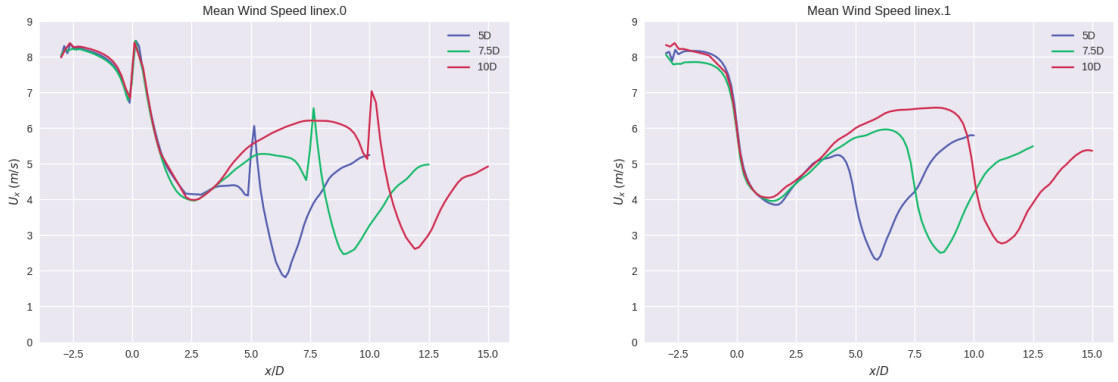

(a) (b)

at the rotor center and at $R/2$ above it are presented in Fig. 66 for the three turbine spacings. Due to the absence of a hub, there is a velocity peak at the hub location that represents a jet. Thus, in Fig. 66a, where the stream-line at the hub is presented, there is a peak for all cases close to $x/D = 0$, which is the first turbine position, and three other peaks: at $x/D = 5$, for the blue curve, at $x/D = 7.5$, for the green curve, and $x/D = 10$, for the red curve, which are the respective downstream turbine position.

However, in Fig. 66b, where the results for the line at $R/2$ above the hub are presented, profiles without these velocity peaks are obtained. At this height the effects of the hub jet are minor, and the wake recovery can be analyzed. The inflow wind speed (8 m/s) decelerates before reaching the turbine at $x/D = 0$, and reaches a minimum velocity around $1.5D$ downstream the turbine. After this point, the wake starts to dissipate and recover the energy at a similar rate for all cases. For the $5D$ spacing (blue curve), the wake has less time and space to recover before reaching the downstream turbine. For the $10D$ case, the wake recovers for a longer period, which allows the maximum wake speed to be 25% greater than in the $5D$ case.

For the upstream wind turbine, the power coefficient remained around 0.55 for all cases. However, for the downstream turbine, a substantial increase in power was observed for larger spacing. At $5D$, the predicted power coefficient of the downstream turbine was 0.24, for $7.5D$ it was 0.30, and for $10D$ it was 0.34. That means a boost of more than 40% in power by doubling the distance. The thrust coefficient at the upstream turbine was 0.83, and for the downstream turbines 0.61, 0.66, and 0.69 for $5D$, $7.5D$ and $10D$ respectively, an increase of 14% in the thrust force comparing the extreme cases.

The turbulent flow plays a significant role in the downstream turbine forces. Without turbulence, as presented in Section 4.3.4, the rate between the predicted power for the upstream and downstream turbine was around 10, but with the addition turbulence, it was about 2. Therefore, modelling turbulence is fundamental to have a more realistic simulation,

Figure 67 – Transverse lines of wind speed at hub height for a turbine spacing of 5 diameters (a) and 10 diameters (b).

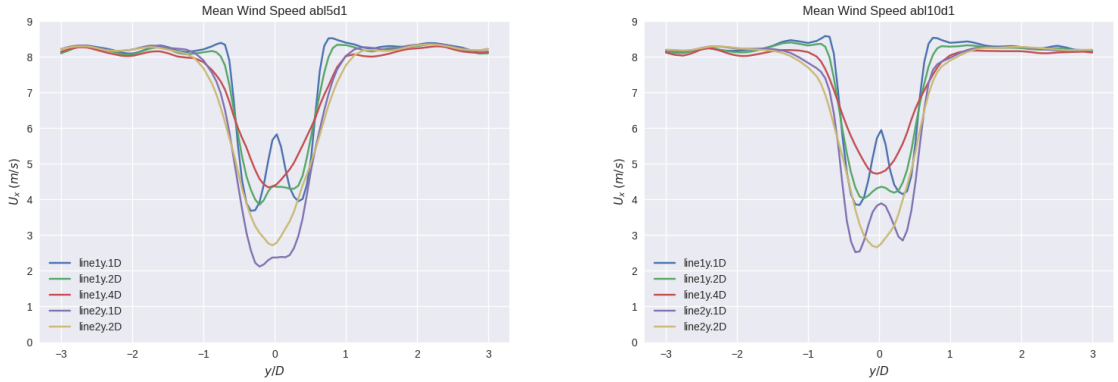

(a) (b)

but one should be aware that the levels of turbulence will significantly impact the results. Thus, each site and situation will demand a specific set of turbulence parameters.

The three cases have different domain sizes since the outlet boundary is 5 diameters downstream the downstream turbine, which has a different location for each case. Therefore, for all the cases, the wake after the second turbine recovers $5D$ downstream. One may notice that the outlet wind speed in Fig. 66b is higher the shorter the turbine spacing is. This occurs because the turbulence that reaches the downstream turbine is higher for shorter distances, so the wake recovery is faster. It is clear that turbulence enhances wake recovery and could possibly increase power production at downstream turbines, but we have to bear in mind that the fluctuation in the loads may be undesirable (this analysis is not in the scope of this work).

Now we analyse profiles along horizontal lines perpendicular to the flow direction: the y-direction. Transverse lines of wind speed at hub height for a turbine spacing of 5 diameters and 10 diameters are presented in Fig 67. Regarding the legend, "line1" refers to the first wind turbine, and "$1D$" refers to 1 diameter downstream it. So, "line2y.2D" presents the wind profile in the y-direction at the x position 2 diameters downstream the second wind turbine.

Comparing the case for $5D$ spacing (Fig. 67a) and $10D$ spacing (Fig. 67b), the blue and green curves are practically the same since they refer to 1 and 2 diameters downstream the first turbine. For the red curve, at 4 diameters downstream the first turbine, the $5D$ case presents lower wind speeds because the flow is already affected by the presence of a second turbine at $5D$ downstream. The most different curve is the purple one, which represents the flow 1 diameter downstream the second wind turbine, and the lowest values for the $5D$ case. The last curve, yellow, is again similar for both cases since the wake recovers faster for the $5D$ case.

The most interesting observation in these plots is the asymmetry close to $y/D = 0$

Figure 68 – Vertical wind profile at 1 diameter downstream the first turbine for a model with and without hub.

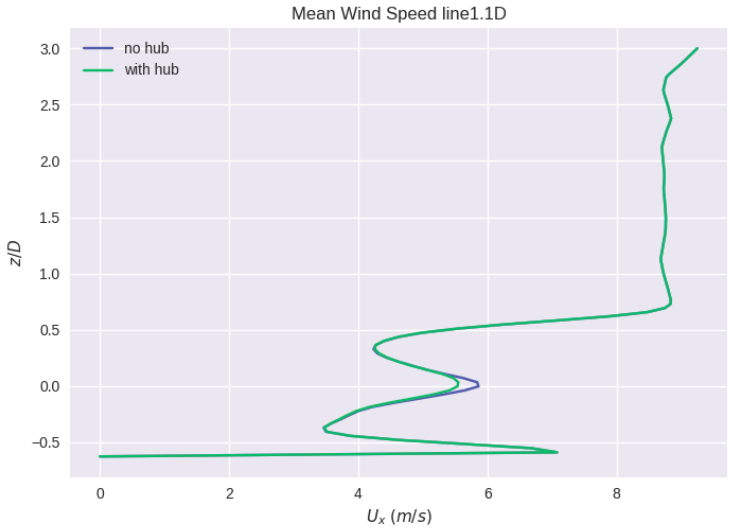

axis. One can notice that the left-hand side has slightly lower wind speeds than the right-hand side. This is due to the wake rotation and the presence of an atmospheric boundary layer. On the left-hand side, the rotational wake brings less energy from below, while on the right-hand side the wake brings more energy from above, where wind speeds are higher. An attentive look at the tip vortices in Fig. 61 reveals that the wind turbine rotates in the x-direction. So, at the hub height, the blade moves downward at the negative side of the y-axis. However, the wake rotates in the opposite side of the wind turbine, since the flow imposes momentum in the blade, and the blade imposes momentum in opposite direction. Therefore, in the negative side of the y-axis, the wake brings flow from below, with less energy, resulting in lower values on the left side of the plots in Fig. 67. This confirms that the simulation agrees with the theory, and correctly reproduces the rotational wake dynamics.

Considering the importance of modelling the hub and tower, a test was made by modelling the hub as an actuator point with a very high drag coefficient (~ 10), and an actuator line with a cylinder drag coefficient (~ 1) at the tower location. For example, for a wind tunnel model scale, Stevens, Martínez-Tossas and Meneveau (2018) chose $C_D = 4$, and the first author of that work used $C_D = 9.18$ in a recent collaboration of wind farm in an experimental model scale.

The vertical profile downstream the turbine is presented in Fig 68. Very small differences are observed, except for a slightly lower wind speed at hub height. Similarly to Fig. 66, streamwise lines passing at the center-line with and without a hub model is presented in Fig 69. The wind speed profile is similar at the whole domain, except at the hub location where the presence of the hub results in a smaller peak.Other techniques of modelling the hub, such as immersed boundary method, can lead to more important

Figure 69 – Stream-wise line passing at the center-line with and without a hub model.

Figure 70 – Stream-wise line passing at $R/2$ above the center-line for higher and lower turbulence intensity for two turbines spaced by 5 diameters.

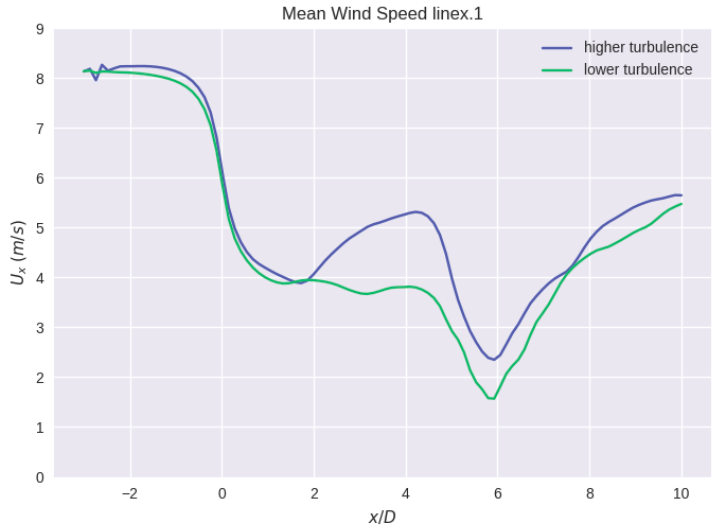

impacts on the flow. The fact that the actuator point does not impose a zero velocity (or no-slip condition at the hub surface) allows an easier flow solution, but probably a less realistic one. Modelling the hub by actuator lines or points remains a research topic to be improved.

Finally, a comparison is made for different turbulence intensities for the $5D$ case. Figure 70 presents the stream-wise line passing at $R/2$ above the center-line for higher and lower turbulence intensity for the $5D$ case. The wake recovery after the first turbine is higher for the most turbulent case, what is expected, and a result already seen comparing the wake for $5D$ and $10D$ spacing. However, the wake downstream the second turbine has a similar recovery for both cases. This occurs because at this point the inlet turbulent

condition is less significant than the turbulence produced by the two turbines in tandem. In other words, the flow after two turbines is almost independent of the inlet conditions, for close turbine spacing. This is an interesting result for wind farms with several layers because it means that for the third row of wind turbines the flow characteristics have low dependence on the inflow parameters which becomes an advantage for modelling techniques.

5 CONCLUSION

The present work introduced the current wind energy context and some of the research topics involved in its development. The need for renewable energy sources is a growing demand, and wind energy is playing a fundamental role in the transition to a sustainable future. Among many topics that surround wind turbine physics, aerodynamics was the central theme of this work.

The fundamentals of rotor modelling were presented and the state of the art was examined. The actuator models have been extensively used to simulate wind turbines and wind farms, analyzing performance and wake flow. The most appropriate model depends on the subject of interest. When the focus is the general aspects of the flow, in a wind farm, for example, the flow dynamics close to each rotor may not be as relevant as the far wake, thus the actuator disc model (ADM) should be appropriate. Although ADM is unable to provide details about the flow structures in the near-wake region due to its axisymmetric behaviour, it provides satisfactory results for wind turbine performance and overall flow dynamics.

On the other hand, when the near-wake turbulent structures are important, for example, when the wind turbine faces the wake from a close turbine or the interaction of the rotor and its own wake is the subject of interest, the suitable method should be the actuator line model (ALM). It captures the influence of each blade and the smaller turbulent structures such as tip and root vortices. However, since the $\mathrm{CFL}_{\mathrm{tip}}$ is more restrictive than the usual CFL condition, the time-step in ALM simulations must be considerably smaller than in ADM simulations, leading to higher computational cost. Still, this model is much less costly than bladed-resolved simulations and can provide accurate results for wind farm performance and wake dynamics.

In this work, the numerical tools used to simulate wind turbines were: OpenFOAM, for flow field calculations and actuator disc model, turbinesFoam, for actuator line, and OpenFAST for BEM computations. We found that the simplest ADM available in OpenFOAM can provide reasonable turbine performance predictions based on the C_T and C_P curves. However, the more complex ADM, which uses the blade element theory, has some physical inconsistencies and needs some corrections concerning the force calculations for wind turbine applications. The turbinesFoam library, which implements ALM in OpenFOAM, was verified with another open-source software (Winc3D), with an excellent agreement, and results compared with BEM had a very good agreement for finer meshes.

The importance of turbulent inlet condition for RANS simulations was evaluated. Higher turbulence intensity leads to faster wake recovery, increasing the power production of the downstream turbine in tandem arrangements. In addition, we examined the spacing between two wind turbines in tandem. For larger distances, the wake loss was smaller, and the energy production was larger, which is desirable. On the other hand, larger spacing

increases the capital cost due to longer array cables and larger array footprint. In real applications, this parameter remains about 6 to 8 diameters.

In ALM simulations with LES, the numerical parameters can have a considerable impact on the results. We have fixed the smoothing force projection to $\epsilon = 2.5\Delta_g$ and showed that the mesh refinement reduces the power and thrust and converges to BEM results. Previous works had shown that mesh refinement would increase the predicted value of power production. However, the apparent difference is because in those works, the authors fixed ϵ at a specific length, and in this work we fixed it with respect to the grid size. We demonstrated that coarse grid meshes overestimate the forces specially near the tip, thus a tip correction would provide better a prediction for C_P and C_T in this case.

Furthermore, the angle of attack (AoA) was compared in ALM and BEM simulations showing an intrinsic difference between the models, which explains small differences even for a converged mesh. The AoA curve provided by BEM had some discontinuities because it considers the flow to be radially independent. In contrast, the ALM provided a continuous curve because the model is governed by the three-dimensional Navier-Stokes equations and, therefore, the entire flow is coupled, avoiding discontinuities.

An interesting investigation about the type of mesh refinement was conducted by analyzing the turbine performance results between homogeneous and non-homogeneous meshes. We found that the grid size far from the rotor has no impact on the power and thrust prediction. This is a very useful result because it proves that the mesh can be coarsened far from the turbine with no loss in performance prediction. However, a comparison study of the wake flow was not done and can be conducted in future works.

In addition, two turbines in tandem were simulated with ALM and LES. We found a significant wake loss, in agreement with other numerical investigations, but probably far from reality because of the laminar inflow condition. For this reason, the addition of a turbulent inlet was analyzed. Two techniques were investigated, the precursor simulation and the synthetic turbulence generator. The latter, less computational costly and more flexible to adjust turbulence parameters, was implemented by the DF-SEM OpenFOAM boundary condition.

The final results of this work compared different turbine spacing, levels of turbulence, and hub and tower modelling. The better wake recovery for $10D$ case compared to $5D$ increased the power prediction of the downstream turbine by more than 40%, which explains why short distances are not usual in operational wind farms. Further, the absence of a hub implied an unrealistic jet at the hub height and the modelling of it by actuator point was tested with no significant impact on the flow. Thus, the appropriate hub and modelling should be a topic of refinement for future models. Also, the levels of turbulence showed an important impact on the wake recovery of the first wind turbine, but not very significant for the second one. This is an important finding for a wind farm of several rows close to each other since it suggests that the inlet turbulent quantities have little impact

on the downstream turbines, a great advantage for modelling techniques.

Finally, to simulate a more realistic situation, the addition of an appropriate model of the hub and tower, ABL stability condition due to the vertical temperature gradient, aeroelasticity, control system for variable rotation, and rotor motion for floating offshore applications are desirable for future works.

BIBLIOGRAPHY

Abkar, M.; Porté-Agel, F. The effect of free-atmosphere stratification on boundary-layer flow and power output from very large wind farms. *Energies*, Multidisciplinary Digital Publishing Institute, v. 6, n. 5, p. 2338–2361, 2013. Cited in page 44.

Abkar, M.; Porté-Agel, F. Influence of atmospheric stability on wind-turbine wakes: A large-eddy simulation study. *Physics of fluids*, AIP Publishing LLC, v. 27, n. 3, p. 035104, 2015. Cited in page 43.

Arabgolarcheh, A.; Jannesarahmadi, S.; Benini, E.; Menegozzo, L. Numerical study of a horizontal wind turbine under yaw conditions. *Mathematical Problems in Engineering*, Hindawi, v. 2021, 2021. Cited in page 48.

Bachant, A. G. P.; Wosnik, M. *turbinesFoam: v0.1.1, Actuator line modeling extension library for OpenFOAM*. Zenodo, 2019. Available on: <https://doi.org/10.5281/zenodo.3542301>. Cited in page 51.

Bachant, P.; Goude, A.; Wosnik, M. Actuator line modeling of vertical-axis turbines. *arXiv preprint arXiv:1605.01449*, 2016. Cited in page 55.

Bastankhah, M.; Porté-Agel, F. A new analytical model for wind-turbine wakes. *Renewable energy*, Elsevier, v. 70, p. 116–123, 2014. Cited in page 44.

Betz, A. Das maximum der theoretisch möglichen ausnutzung des windes durch windmotoren. *Zeitschrift fur das gesamte Turbinenwesten*, v. 20, 1920. Cited in page 30.

BP. Energy Outlook. 2020. Available on: <https://www.bp.com/en/global/corporate/energy-economics/energy-outlook.html>. Cited in page 22.

Branlard, E. *Wind turbine aerodynamics and vorticity-based methods: Fundamentals and recent applications*. : Springer, 2017. v. 7. Cited in page 43.

Breton, S.-P. et al. A survey of modelling methods for high-fidelity wind farm simulations using large eddy simulation. *Philosophical Transactions of the Royal Society A: Mathematical, Physical and Engineering Sciences*, The Royal Society Publishing, v. 375, n. 2091, p. 20160097, 2017. Cited in page 45.

Burton, T.; Jenkins, N.; Sharpe, D.; Bossanyi, E. *Wind energy handbook*. : John Wiley & Sons, 2011. Cited 7 times in pages 29, 31, 32, 33, 34, 36, and 38.

Churchfield, M. et al. Using high-fidelity computational fluid dynamics to help design a wind turbine wake measurement experiment. In: IOP Publishing. *Journal of Physics: Conference Series*. 2016. v. 753, n. 3, p. 032009. Cited in page 42.

Dağ, K. O.; Sørensen, J. N. A new tip correction for actuator line computations. *Wind Energy*, Wiley Online Library, v. 23, n. 2, p. 148–160, 2020. Cited in page 40.

Deskos, G.; Laizet, S.; Palacios, R. Winc3d: A novel framework for turbulence-resolving simulations of wind farm wake interactions. *Wind Energy*, Wiley Online Library, v. 23, n. 3, p. 779–794, 2020. Cited in page 68.

Elliott, W. P. The growth of the atmospheric internal boundary layer. *Eos, Transactions American Geophysical Union*, Wiley Online Library, v. 39, n. 6, p. 1048–1054, 1958. Cited in page 43.

Eriksen, P. E.; Krogstad, P.-Å. Development of coherent motion in the wake of a model wind turbine. *Renewable Energy*, Elsevier, v. 108, p. 449–460, 2017. Cited in page 41.

Fleming, P. et al. *SOWFA super-controller: A high-fidelity tool for evaluating wind plant control approaches*. 2013. Cited in page 55.

Froude, R. E. On the part played in propulsion by differences of fluid pressure. *Trans. Inst. Naval Architects*, v. 30, p. 390, 1889. Cited 4 times in pages 28, 29, 38, and 56.

Glauert, H. *Aerodynamic Theory, edited by WF Durand.* : Springer-Verlag, Berlin, 1935. Cited 2 times in pages 28 and 36.

GWEC, G. W. E. C. Global Wind Report. 2021. Available on: <https://gwec.net/global-wind-report-2021/>. Cited 5 times in pages 18, 19, 21, 22, and 23.

Hand, M. M. et al. *Unsteady aerodynamics experiment phase VI: wind tunnel test configurations and available data campaigns*. 2001. Cited in page 36.

Heyes, A.; Jones, R.; Smith, D. Wandering of wing-tip vortices. In: *Proceedings of 12th international symposium on the applications of laser techniques to fluid mechanics. Lisbon, Portugal*. 2004. Cited in page 41.

IEA, I. E. A. Technology Roadmap: Wind Energy. Paris, 2013. Available on: <https://www.iea.org/reports/technology-roadmap-wind-energy-2013>. Cited in page 24.

IEA, I. E. A. Electricity Market Report. Paris, 2020. Available on: <https://www.iea.org/reports/electricity-market-report-december-2020>. Cited in page 21.

IEA, I. E. A. World Energy Outlook. Paris, 2020. Available on: <https://www.iea.org/reports/world-energy-outlook-2020>. Cited in page 20.

IEA, I. E. A. Net Zero by 2050: A Road Map for the Global Energy Sector. Paris, 2021. Available on: <https://www.iea.org/reports/net-zero-by-2050>. Cited in page 22.

IPCC, I. P. o. C. C. Global Warming of 1.5°C: Special Report. 2018. Available on: <https://www.ipcc.ch/sr15/>. Cited 2 times in pages 18 and 21.

IPCC, I. P. o. C. C. Climate Change and Land. 2019. Available on: <https://www.ipcc.ch/srccl/>. Cited in page 20.

IRENA, I. R. E. A. Global Renewables Outlook. 2020. Available on: <https://www.irena.org/publications/2020/Apr/Global-Renewables-Outlook-2020>. Cited in page 22.

Jensen, N. A note on wind turbine interaction. *Riso-M-2411, Risoe National Laboratory, Roskilde, Denmark*, p. 16, 1983. Cited in page 44.

Jha, P. K.; Churchfield, M. J.; Moriarty, P. J.; Schmitz, S. The effect of various actuator-line modeling approaches on turbine-turbine interactions and wake-turbulence statistics in atmospheric boundary-layer flow. In: *32nd ASME Wind Energy Symposium*. 2014. p. 0710. Cited in page 52.

Jha, P. K.; Schmitz, S. Actuator curve embedding–an advanced actuator line model. *Journal of Fluid Mechanics*, Cambridge University Press, v. 834, 2018. Cited 2 times in pages 50 and 51.

Johlas, H.; Martínez-Tossas, L.; Lackner, M.; Schmidt, D.; Churchfield, M. Large eddy simulations of offshore wind turbine wakes for two floating platform types. In: IOP Publishing. *Journal of Physics: Conference Series*. 2020. v. 1452, n. 1, p. 012034. Cited in page 52.

Jonkman, J.; Butterfield, S.; Musial, W.; Scott, G. *Definition of a 5-MW reference wind turbine for offshore system development*. 2009. Cited 2 times in pages 33 and 69.

Jonkman, J. M.; Jr, M. L. B. et al. Fast user's guide. *Golden, CO: National Renewable Energy Laboratory*, Citeseer, v. 365, p. 366, 2005. Cited in page 56.

Joukowsky, N. Vortex theory of screw propeller, i. *Trudy Otdeleniya Fizicheskikh Nauk Obshchestva Lubitelei Estestvoznaniya*, Gauthier-Villars Paris, v. 16, n. 1, p. 1–31, 1912. Cited in page 30.

Khan, M.; Odemark, Y.; Fransson, J. H. Effects of inflow conditions on wind turbine performance and near wake structure. *Open Journal of Fluid Dynamics*, Scientific Research Publishing, v. 7, n. 1, p. 105–129, 2016. Cited in page 41.

Klein, M.; Sadiki, A.; Janicka, J. A digital filter based generation of inflow data for spatially developing direct numerical or large eddy simulations. *Journal of Computational Physics*, Elsevier, v. 186, n. 2, p. 652–665, 2003. Cited in page 77.

Laan, M. P. van der et al. The k-ε-fp model applied to double wind turbine wakes using different actuator disk force methods. *Wind Energy*, Wiley Online Library, v. 18, n. 12, p. 2223–2240, 2015. Cited 2 times in pages 38 and 47.

Laan, M. P. van der et al. The k-ε-fp model applied to wind farms. *Wind Energy*, Wiley Online Library, v. 18, n. 12, p. 2065–2084, 2015. Cited in page 38.

Laizet, S.; Lamballais, E. High-order compact schemes for incompressible flows: A simple and efficient method with quasi-spectral accuracy. *Journal of Computational Physics*, Elsevier, v. 228, n. 16, p. 5989–6015, 2009. Cited in page 68.

Larsen, G. C.; Madsen, H. A.; Thomsen, K.; Larsen, T. J. Wake meandering: a pragmatic approach. *Wind Energy: An International Journal for Progress and Applications in Wind Power Conversion Technology*, Wiley Online Library, v. 11, n. 4, p. 377–395, 2008. Cited in page 42.

Li, P.; Cheng, P.; Wan, D.; Xiao, Q. Numerical simulations of wake flows of floating offshore wind turbines by unsteady actuator line model. In: *Proceedings of the 9th international workshop on ship and marine hydrodynamics, Glasgow, UK*. 2015. p. 26–28. Cited in page 52.

Liu, L. et al. Evaluating the accuracy of the actuator line model against blade element momentum theory in uniform inflow. *Wind energy*, Wiley Online Library, v. 25, n. 6, p. 1046–1059, 2022. Cited in page 69.

Lock, C.; Bateman, H.; Townend, H. *Experiments to verify the independence of the elements of an airscrew blade.* : HM Stationery Office, 1924. Cited in page 32.

Ma, Z.; Lei, L.; Dowell, E.; Zeng, P. An experimental study on the actuator line method with anisotropic regularization kernel. *Energies*, Multidisciplinary Digital Publishing Institute, v. 13, n. 4, p. 977, 2020. Cited in page 49.

Machefaux, E. et al. An experimental and numerical study of the atmospheric stability impact on wind turbine wakes. *Wind Energy*, Wiley Online Library, v. 19, n. 10, p. 1785–1805, 2016. Cited in page 43.

Mann, J. The spatial structure of neutral atmospheric surface-layer turbulence. *Journal of fluid mechanics*, Cambridge University Press, v. 273, p. 141–168, 1994. Cited in page 49.

Martinez, L.; Leonardi, S.; Churchfield, M.; Moriarty, P. A comparison of actuator disk and actuator line wind turbine models and best practices for their use. In: *50th AIAA Aerospace Sciences Meeting including the New Horizons Forum and Aerospace Exposition*. 2012. p. 900. Cited in page 39.

Martínez-Tossas, L. A.; Churchfield, M. J.; Leonardi, S. Large eddy simulations of the flow past wind turbines: actuator line and disk modeling. *Wind Energy*, Wiley Online Library, v. 18, n. 6, p. 1047–1060, 2015. Cited 5 times in pages 46, 47, 48, 50, and 70.

Martínez-Tossas, L. A.; Churchfield, M. J.; Meneveau, C. Optimal smoothing length scale for actuator line models of wind turbine blades based on gaussian body force distribution. *Wind Energy*, Wiley Online Library, v. 20, n. 6, p. 1083–1096, 2017. Cited in page 49.

Meneveau, C. Big wind power: Seven questions for turbulence research. *Journal of Turbulence*, Taylor & Francis, v. 20, n. 1, p. 2–20, 2019. Cited in page 53.

Meyers, J.; Meneveau, C. Large eddy simulations of large wind-turbine arrays in the atmospheric boundary layer. In: *48th AIAA aerospace sciences meeting including the new horizons forum and aerospace exposition*. 2010. p. 827. Cited in page 46.

Meyers, J.; Meneveau, C. Optimal turbine spacing in fully developed wind farm boundary layers. *Wind Energy*, Wiley Online Library, v. 15, n. 2, p. 305–317, 2012. Cited in page 64.

Miao, W.; Li, C.; Pavesi, G.; Yang, J.; Xie, X. Investigation of wake characteristics of a yawed hawt and its impacts on the inline downstream wind turbine using unsteady cfd. *Journal of Wind Engineering and Industrial Aerodynamics*, Elsevier, v. 168, p. 60–71, 2017. Cited in page 51.

Micallef, D.; Rezaeiha, A. Floating offshore wind turbine aerodynamics: Trends and future challenges. *Renewable and Sustainable Energy Reviews*, Elsevier, v. 152, p. 111696, 2021. Cited in page 52.

Mittal, A.; Sreenivas, K.; Taylor, L. K.; Hereth, L.; Hilbert, C. B. Blade-resolved simulations of a model wind turbine: effect of temporal convergence. *Wind Energy*, Wiley Online Library, v. 19, n. 10, p. 1761–1783, 2016. Cited in page 40.

Nassif, F. B. et al. Coastal wind measurements and power assessment using a lidar on a pier. *Revista Brasileira de Meteorologia*, SciELO Brasil, v. 35, p. 255–268, 2020. Cited in page 77.

Onel, H. C.; Tuncer, I. H. A comparative study of wake interactions between wind-aligned and yawed wind turbines using les and actuator line models. In: IOP Publishing. *Journal of Physics: Conference Series*. 2020. v. 1618, n. 6, p. 062009. Cited in page 51.

Onel, H. C.; Tuncer, I. H. Estimation of wake induced power loss in wind turbines using actuator line model. In: *AIAA AVIATION 2020 FORUM*. 2020. p. 3054. Cited in page 51.

Patrao, A. C. Description and validation of the rotordisksource class for propeller performance estimation. *Proceedings of the CFD with Open Source Software*, 2017. Cited in page 38.

Poletto, R.; Craft, T.; Revell, A. A new divergence free synthetic eddy method for the reproduction of inlet flow conditions for les. *Flow, turbulence and combustion*, Springer, v. 91, n. 3, p. 519–539, 2013. Cited in page 77.

Politis, E. S. et al. Modeling wake effects in large wind farms in complex terrain: the problem, the methods and the issues. *Wind Energy*, Wiley Online Library, v. 15, n. 1, p. 161–182, 2012. Cited in page 44.

Porté-Agel, F.; Bastankhah, M.; Shamsoddin, S. Wind-turbine and wind-farm flows: a review. *Boundary-Layer Meteorology*, Springer, v. 174, n. 1, p. 1–59, 2020. Cited 7 times in pages 26, 41, 42, 44, 45, 47, and 53.

Porté-Agel, F.; Wu, Y.-T.; Lu, H.; Conzemius, R. J. Large-eddy simulation of atmospheric boundary layer flow through wind turbines and wind farms. *Journal of Wind Engineering and Industrial Aerodynamics*, Elsevier, v. 99, n. 4, p. 154–168, 2011. Cited 2 times in pages 47 and 48.

Prandtl, L. Appendix to the paper of a. betz: Schraubenpropeller mit geringstem energieverlust. *Gottinger Nachrichten*, p. 193–213, 1919. Cited 2 times in pages 28 and 35.

Rankine, W. J. M. On the mechanical principles of the action of propellers. *Transactions of the Institution of Naval Architects*, v. 6, 1865. Cited in page 28.

Revaz, T.; Porté-Agel, F. Large-eddy simulation of wind turbine flows: A new evaluation of actuator disk models. *Energies*, Multidisciplinary Digital Publishing Institute, v. 14, n. 13, p. 3745, 2021. Cited 2 times in pages 45 and 48.

Richardson, L. F. The approximate arithmetic solution by finite differences of physical problems involving differential equations, with application to stresses in a masonry dam. Transactions of the Royal Society of London, v. 210, p. 307–357, 1910. Cited in page 69.

Roy, S. B.; Pacala, S. W.; Walko, R. Can large wind farms affect local meteorology? *Journal of Geophysical Research: Atmospheres*, Wiley Online Library, v. 109, n. D19, 2004. Cited in page 43.

Sanderse, B.; Pijl, S. Van der; Koren, B. Review of computational fluid dynamics for wind turbine wake aerodynamics. *Wind energy*, Wiley Online Library, v. 14, n. 7, p. 799–819, 2011. Cited 2 times in pages 45 and 46.

Schmitz, S.; Jha, P. Modeling the wakes of wind turbines and rotorcraft using the actuator-line method in an openfoam-les solver. In: American Helicopter Society. *Annual Forum Proceedings-AHS International*. 2013. v. 3, p. 2228–2235. Cited in page 51.

Schottler, J. et al. Comparative study on the wake deflection behind yawed wind turbine models. In: IOP Publishing. *Journal of Physics: Conference Series*. 2017. v. 854, n. 1, p. 012032. Cited in page 42.

Shamsoddin, S.; Porté-Agel, F. Turbulent planar wakes under pressure gradient conditions. *Journal of Fluid Mechanics*, Cambridge University Press, v. 830, 2017. Cited in page 44.

Shen, W. Z.; Mikkelsen, R.; Sørensen, J. N.; Bak, C. Tip loss corrections for wind turbine computations. *Wind Energy: An International Journal for Progress and Applications in Wind Power Conversion Technology*, Wiley Online Library, v. 8, n. 4, p. 457–475, 2005. Cited 2 times in pages 36 and 51.

Shen, W. Z.; Sørensen, J. N.; Zhang, J. Actuator surface model for wind turbine flow computations. In: *Proceedings of European Wind Energy Conference and Exhibition*. 2007. v. 7, n. 10. Cited in page 46.

Sherry, M.; Sheridan, J.; Jacono, D. L. Characterisation of a horizontal axis wind turbine's tip and root vortices. *Experiments in fluids*, Springer, v. 54, n. 3, p. 1–19, 2013. Cited in page 41.

Simisiroglou, N.; Sarmast, S.; Breton, S.-P.; Ivanell, S. Validation of the actuator disc approach in phoenics using small scale model wind turbines. In: IOP Publishing. *Journal of Physics: Conference Series*. 2016. v. 753, n. 3, p. 032028. Cited in page 47.

Sørensen, J. N.; Nilsson, K.; Ivanell, S.; Asmuth, H.; Mikkelsen, R. F. Analytical body forces in numerical actuator disc model of wind turbines. *Renewable energy*, Elsevier, v. 147, p. 2259–2271, 2020. Cited 2 times in pages 47 and 49.

Sørensen, J. N.; Shen, W. Z. Numerical modeling of wind turbine wakes. *J. Fluids Eng.*, v. 124, n. 2, p. 393–399, 2002. Cited 2 times in pages 28 and 39.

Stevens, R. J.; Martínez-Tossas, L. A.; Meneveau, C. Comparison of wind farm large eddy simulations using actuator disk and actuator line models with wind tunnel experiments. *Renewable energy*, Elsevier, v. 116, p. 470–478, 2018. Cited 2 times in pages 45 and 86.

Troldborg, N. Actuator line modeling of wind turbine wakes. 2009. Cited 2 times in pages 40 and 48.

Troldborg, N.; Sorensen, J. N.; Mikkelsen, R. Numerical simulations of wake characteristics of a wind turbine in uniform inflow. *Wind Energy: An International Journal for Progress and Applications in Wind Power Conversion Technology*, Wiley Online Library, v. 13, n. 1, p. 86–99, 2010. Cited 2 times in pages 48 and 49.

Troldborg, N.; Sørensen, J. N.; Mikkelsen, R.; Sørensen, N. N. A simple atmospheric boundary layer model applied to large eddy simulations of wind turbine wakes. *Wind Energy*, Wiley Online Library, v. 17, n. 4, p. 657–669, 2014. Cited in page 49.

Veers, P. et al. Grand challenges in the science of wind energy. *Science*, American Association for the Advancement of Science, v. 366, n. 6464, 2019. Cited 2 times in pages 53 and 54.

Vermeer, L.; Sørensen, J. N.; Crespo, A. Wind turbine wake aerodynamics. *Progress in aerospace sciences*, Elsevier, v. 39, n. 6-7, p. 467–510, 2003. Cited 3 times in pages 26, 41, and 47.

Wahono, S. *Development of virtual blade model for modelling helicopter rotor downwash in openfoam*. 2013. Cited in page 38.

Wang, J.-h.; Zhao, W.-w.; Wan, D.-c. Development of naoe-foam-sjtu solver based on openfoam for marine hydrodynamics. *Journal of Hydrodynamics*, Springer, v. 31, n. 1, p. 1–20, 2019. Cited in page 52.

Weller, H. G.; Tabor, G.; Jasak, H.; Fureby, C. A tensorial approach to computational continuum mechanics using object-oriented techniques. *Computers in physics*, American Institute of Physics, v. 12, n. 6, p. 620–631, 1998. Cited in page 55.

Wimshurst, A.; Willden, R. Analysis of a tip correction factor for horizontal axis turbines. *Wind Energy*, Wiley Online Library, v. 20, n. 9, p. 1515–1528, 2017. Cited in page 36.

WMO, W. M. O. The State of the Global Climate 2020. 2021. Available on: <https://public.wmo.int/en/our-mandate/climate/wmo-statement-state-of-global-climate>. Cited 2 times in pages 18 and 19.

Wu, K. L.; Porté-Agel, F. Flow adjustment inside and around large finite-size wind farms. *Energies*, Multidisciplinary Digital Publishing Institute, v. 10, n. 12, p. 2164, 2017. Cited in page 43.

Wu, Y.-T.; Porté-Agel, F. Large-eddy simulation of wind-turbine wakes: evaluation of turbine parametrisations. *Boundary-layer meteorology*, Springer, v. 138, n. 3, p. 345–366, 2011. Cited in page 46.

Yang, X.; Howard, K. B.; Guala, M.; Sotiropoulos, F. Effects of a three-dimensional hill on the wake characteristics of a model wind turbine. *Physics of Fluids*, AIP Publishing LLC, v. 27, n. 2, p. 025103, 2015. Cited in page 44.

Yu, Z.; Zheng, X.; Ma, Q. Study on actuator line modeling of two nrel 5-mw wind turbine wakes. *Applied Sciences*, Multidisciplinary Digital Publishing Institute, v. 8, n. 3, p. 434, 2018. Cited in page 52.